UNIVERSITY OF OTAGO

MASTER THESIS

Frequency Tuning of Whispering Gallery Mode Resonators with Planar Dielectric Substrates

Author:
Patrick A. DEVANE

Supervisor:
Dr. Harald G. L. SCHWEFEL

A thesis submitted in fulfilment of the requirements for the degree of Master of Science in Physics

in the

Department of Physics

July 8, 2019

"This is the real secret of life – to be completely engaged with what you are doing in the here and now. And instead of calling it work, realize it is play."

Alan Watts

UNIVERSITY OF OTAGO

Abstract

Department of Physics

Master of Science in Physics

Frequency Tuning of Whispering Gallery Mode Resonators with Planar Dielectric Substrates

by Patrick A. DEVANE

In this work we investigate the proposed relationship between planar dielectric substrates of increasing refractive index, and their effect on the frequency of a resonant mode confined in a whispering gallery mode resonator. We did this using a heavily automated setup to facilitate the collection of large quantities of data. Not all of this data is useful due to recurring instabilities within the experimental setup.

Despite the instabilities we were able to collect and analyse a sample of data for both TE and TM polarised modes when they interacted with a substrate. We used seven substrates which gave us a refractive index range of 1.43 to 4.0. We built plots that highlight the effect that these substrates have on both the frequency of the mode and the broadening of the mode for the substrates where mode-broadening was shown to occur.

We measured the effect of the substrates on the frequency of a whispering gallery mode resonance. These results are then compared to the theoretical predictions that inspired this research. We found that the figures we built showed qualitative agreement with the theory especially for the frequency tuning of TE polarised modes. The TM polarised modes also showed agreement with the theory. We also saw some agreement between TE mode broadening results and the theory but the TM mode broadening results are less conclusive when comparing to the theory.

Acknowledgements

I would like to thank everyone in the resonant optics lab for their help with various stages of this project, as well as my other undertakings in the lab over previous years. I must give special mention to Luke Trainor who has been a wealth of knowledge for the duration of my time in the lab. He has helped me move through countless roadblocks in the pursuit of my research and my progress would have been significantly hindered without him.

I would also like to thank my supervisor Harald Schwefel for the constant supervision of my research throughout my time in his lab. He has put up with me since my 2016 summer project which is an achievement not to be understated. He has shown exceptional guidance, patience, encouragement and I shudder to think of the level of research I would have produced without him. I am astounded at what I have accomplished in working under him, from producing my own computer programs to designing components for my experimental setup. I wish everyone in the lab the best and cannot wait to see what they produce in the future.

I would like to thank my friends, work has often prevented me from seeing many of you as often as I would have liked but I hope the results of my prioritisations are clear throughout this thesis and other work I have produced while studying at Otago.

Finally I must thank my family. The support from my parents has been staggering and I will always be grateful for what they have done for me.

Contents

Declaration of Authorship iii

Abstract vii

Acknowledgements ix

List of Figures xv

List of Abbreviations xvii

1 Introduction 1
- 1.1 Whispering Gallery History . . . 1
- 1.2 Whispering Gallery Phenomena . . . 2
- 1.3 Whispering Gallery Resonances . . . 2
- 1.4 Experiment Motivations . . . 4
- 1.5 Thesis Content . . . 5
- 1.6 Outcomes During This MSc . . . 6

2 Whispering Gallery Mode Resonator Fabrication 7
- 2.1 Fabrication Methods . . . 7
- 2.2 Fabrication Component Discussion . . . 7
  - 2.2.1 Lathe . . . 7
  - 2.2.2 Turning Machine . . . 8
  - 2.2.3 Paraffin Wax . . . 8
  - 2.2.4 Brass Rod . . . 9
- 2.3 Computer Control . . . 10
- 2.4 Lithium Niobate Resonator Fabrication Process . . . 10
  - 2.4.1 Drilling The Precursor . . . 10
  - 2.4.2 Mounting The Precursor . . . 11
  - 2.4.3 Cutting The Resonator . . . 12
- 2.5 Polishing of WGMRs . . . 12
- 2.6 Cleaning of WGMRs . . . 13
- 2.7 Maintenance of WGMRs . . . 14

3 Whispering Gallery Mode Resonators 15
- 3.1 WGMR Structure . . . 15
  - 3.1.1 Geometry . . . 15
  - 3.1.2 Birefringence . . . 15
- 3.2 Total Internal Reflection . . . 16
  - 3.2.1 Snell's Law . . . 17
  - 3.2.2 Frustrated Total Internal Reflection . . . 17
- 3.3 Coupling . . . 18
  - 3.3.1 Free-Space Coupling . . . 18
  - 3.3.2 Prism Movement . . . 19

3.3.3 Coupling Angle Calculation . . . 19
3.3.4 Newton's Rings . . . 21
3.4 Mode Observation . . . 22
3.4.1 Modes Characterisation . . . 23
Fundamental Modes . . . 24
3.5 WGMR Characterisation . . . 24
3.5.1 Linewidth . . . 24
3.5.2 Coupling Contrast . . . 24
3.5.3 Quality Factor . . . 25
3.5.4 Free Spectral Range . . . 27
3.6 WGMR Characterisation Measurement Process . . . 27
3.6.1 Coupling Contrast Measurement Process . . . 27
3.6.2 Linewidth Measurement Process . . . 27
3.6.3 Q-Factor Measurement Process . . . 28
3.6.4 FSR Measurement Process . . . 28

4 Experimental Setup **31**
4.1 Experiment Objectives . . . 31
Foreman et al. Theory . . . 31
Frequency Shift Contribution Discussion . . . 31
Our Experiment . . . 32
Red Shift Phenomena . . . 33
Blue Shift Phenomena . . . 34
Mode Broadening . . . 34
4.2 Setup . . . 35
4.3 Automation . . . 36
4.3.1 Computer Communication Discussion . . . 36
Breakout Boxes . . . 37
Network Access . . . 37
4.3.2 Python . . . 38
Frequency Axis Calibration . . . 38
Program Limitations . . . 39
4.3.3 MATLAB . . . 40
4.4 Nanocube Discussion . . . 40
4.4.1 Nanocube Calibration . . . 41
4.5 Attocube Discussion . . . 41
Attocube Movement Mechanisms . . . 42
Attocube Audible Feedback Mechanism . . . 43
4.6 Attocube-Nanocube Scale Calibration . . . 43
4.7 Frequency Shift Direction . . . 43
4.8 Substrate Mounting Orientation . . . 44
4.9 Environment Control . . . 45

5 Experimental Method **53**
5.1 Pre-Sweep Calibrations . . . 53
5.1.1 Polarisation Control . . . 54
Polarising Beam Splitter . . . 54
Paddle Fibre Polarisation Controller . . . 54
Polarisation Test . . . 55
5.2 Data Collection Method . . . 56

6 Experimental Results **59**
6.1 Germanium . . . 59
6.1.1 TE Mode Sweep . . . 59
6.1.2 TM Mode Sweep . . . 59
6.2 Silicon . . . 65
6.2.1 TE Mode Sweep . . . 65
6.2.2 TM Mode Sweep . . . 65
6.3 Zinc Selenide . . . 71
6.3.1 TE Mode Sweep . . . 71
6.3.2 TM Mode Sweep . . . 71
6.4 Zinc Sulfide . . . 77
6.4.1 TE Mode Sweep . . . 77
6.4.2 TM Mode Sweep . . . 77
6.5 Sapphire . . . 83
6.5.1 TE Mode Sweep . . . 83
6.5.2 TM Mode Sweep . . . 83
6.6 Optical Glass . . . 88
6.6.1 TE Mode Sweep . . . 88
6.6.2 TM Mode Sweep . . . 88
6.7 Calcium Fluoride . . . 94
6.7.1 TE Mode Sweep . . . 94
6.7.2 TM Mode Sweep . . . 94
6.8 Substrate Refractive Index Effects on WGMR Modes . . . 99

7 Discussion **101**
7.1 Analysis . . . 101
7.2 Determining Criteria For Results . . . 102
7.2.1 Frequency Shift Measurement . . . 104
7.3 Temperature Control . . . 105
7.4 Conclusion . . . 108
7.5 Outlook . . . 108

Bibliography **109**

List of Figures

1.1 Saint Paul's Cathedral . . . 1
1.2 Glass ball whispering gallery . . . 3
1.3 WGMR Resonances . . . 3
1.4 Foreman et al. (2016) Figure 3a . . . 4

2.1 Laboratory lathe . . . 8
2.2 Newton's rings illustration . . . 9
2.3 Hot plate . . . 10
2.4 Turning machine screenshot . . . 11
2.5 Flattening device . . . 12
2.6 Negative rake angle schematic . . . 13
2.7 Polishing slurries . . . 14

3.1 WGMR Structure . . . 16
3.2 WGMR z-cut diagram . . . 16
3.3 Total Internal Reflection . . . 17
3.4 Frustrated total internal reflection . . . 18
3.5 Coupling Angle Diagram . . . 20
3.6 Newton's rings illustration . . . 21
3.7 Resonator coupling glow . . . 22
3.8 1550nm laser control . . . 22
3.9 Whispering Gallery Modes - Oscilloscope . . . 23
3.10 WGMR Mode numbers . . . 24
3.11 Linewidth measurement . . . 25
3.12 WGMR coupling regimes . . . 26
3.13 Q-factor measurement . . . 28
3.14 FSR measurement . . . 29

4.1 Foreman et al. (2016) Figure 3a repeated . . . 32
4.2 Foreman et al. (2016) Figure 3a-mode broadening . . . 35
4.3 Photograph of Experimental Setup . . . 36
4.4 Breakout Box . . . 37
4.5 Python script screenshot . . . 46
4.6 GUI race condition test . . . 47
4.7 Nanocube Controller . . . 47
4.8 Nanocube Calibration . . . 48
4.9 Attocube picture . . . 48
4.10 Photograph of the attocube controller used . . . 49
4.11 Substrate Orientation . . . 49
4.12 Effect of substrate mounting angle on displacement . . . 50
4.13 Environmental effect on frequency . . . 50
4.14 Environmental controller . . . 51
4.15 Temperature stabiliser . . . 51

5.1 Polarising Beam Splitter 55
5.2 Paddle Fibre Polarisation Controller 55

6.1 Germanium substrate raw results (TE) 61
6.2 Germanium substrate shift results (TE) 62
6.3 Germanium substrate frequency detuning (TE) 62
6.4 Germanium substrate raw results (TM) 63
6.5 Germanium substrate shift results (TM) 64
6.6 Germanium substrate frequency detuning (TM) 64
6.7 Silicon substrate raw results (TE) 67
6.8 Silicon substrate shift results (TE) 68
6.9 Silicon substrate frequency detuning (TE) 68
6.10 Silicon substrate raw results (TM) 69
6.11 Silicon substrate shift results (TM) 70
6.12 Silicon substrate frequency detuning (TM) 70
6.13 Zinc selenide substrate raw results (TE) 73
6.14 Zinc selenide substrate shift results (TE) 74
6.15 Zinc selenide substrate frequency detuning (TE) 74
6.16 Zinc selenide substrate raw results (TM) 75
6.17 Zinc selenide substrate shift results (TM) 76
6.18 Zinc selenide substrate frequency detuning (TM) 76
6.19 Zinc sulfide substrate raw results (TE) 79
6.20 Zinc sulfide substrate shift results (TE) 80
6.21 Zinc sulfide substrate frequency detuning (TE) 80
6.22 Zinc sulfide substrate raw results (TM) 81
6.23 Zinc sulfide substrate shift results (TM) 82
6.24 Zinc sulfide substrate frequency detuning (TM) 82
6.25 Sapphire substrate raw results (TE) 84
6.26 Sapphire substrate shift results (TE) 85
6.27 Sapphire substrate frequency detuning (TE) 85
6.28 Sapphire substrate raw results (TM) 86
6.29 Sapphire substrate shift results (TM) 87
6.30 Sapphire substrate frequency detuning (TM) 87
6.31 Optical glass substrate raw results (TE) 90
6.32 Optical glass substrate shift results (TE) 91
6.33 Optical glass substrate frequency detuning (TE) 91
6.34 Optical glass substrate raw results (TM) 92
6.35 Optical glass substrate shift results (TM) 93
6.36 Optical glass substrate frequency detuning (TM) 93
6.37 Calcium fluoride substrate raw results (TE) 95
6.38 Calcium fluoride substrate shift results (TE) 96
6.39 Calcium fluoride substrate frequency detuning (TE) 96
6.40 Calcium fluoride substrate raw results (TM) 97
6.41 Calcium fluoride substrate shift results (TM) 98
6.42 Calcium fluoride substrate frequency detuning (TM) 98
6.43 Effect of substrate refractive index on mode frequency 99
6.44 Effect of substrate refractive index on mode broadening 100

7.1 Savchenkov figure 105

List of Abbreviations

WGM	**W**hispering **G**allery **M**ode
WGMR	**W**hispering **G**allery **M**ode **R**esonator
TE	**T**ransverse **E**lectric
TM	**T**ransverse **M**agnetic
TIR	**T**otal **I**nternal **R**eflection
FTIR	**F**rustrated **T**otal **I**nternal **R**eflection
GRIN	**GR**aded **IN**dex
FSR	**F**ree **S**pectral **R**ange
EOM	**E**lectro-**O**ptic **M**odulator
PCI	**P**eripheral **C**omponent **I**nterconnect
PBS	**P**olarising **B**eam **S**plitter

Dedicated to my parents...

Chapter 1

Introduction

This chapter exists as several distinct sections. The first two sections are to outline the history and phenomenology of whispering galleries. It is important that this is done in absence of the experimental discussion so that a clearer picture of what a whispering gallery is and how it works is shown. This will make it easier to see how a whispering gallery is used in experiments such as the one in this thesis when later chapters are read. After the introduction to whispering galleries we will extend this discussion to the development of how a WGMR can satisfy the resonance condition. We will then move on to discuss the motivations for this thesis and look at the theoretical paper about which the experiment in this thesis is based. Finally we will outline what can be expected in the remainder of this thesis through short synopses of each chapter.

1.1 Whispering Gallery History

A whispering gallery is usually a room with a round edge. These rooms often possess geometry that is circular in nature, although whispering galleries have been discovered with geometry that can deviate, possessing hemispherical, elliptical or ellipsoidal geometry instead. The rooms with these sorts of geometries would often be the result of being built beneath an architectural vault of some kind. Whispering galleries like the Saint Paul's Cathedral (figure 1.1) in London are the result of being built beneath a dome, a common type of architectural vault.

FIGURE 1.1: The whispering gallery in Saint Paul's Cathedral. Image taken from [1].

There are many examples of whispering galleries around the world. Saint Paul's Cathedral in London is a popular example as it is also the location where Lord

Rayleigh began work on understanding them (detailed below in 1.2). Other examples include Grand Central Terminal in New York, Saint Peter's Basilica in the Vatican City and The Church of the Holy Sepulcher in Jerusalem.

The name "whispering gallery" comes from the discovery that a message whispered along a wall could be clearly heard in other parts of the gallery. Two people could have a whispered conversation in such a gallery and find that even if they stood on opposite sides of the gallery, the message would be better preserved when whispered along the wall rather than at the person directly across the room. It was noticed that the sound would seemingly "stick" to the walls as it travelled, allowing for whispered communication from one part of the wall to any other part on the circumference. Furthermore, it was noticed someone standing in the centre of the room would not be able to hear the whispers even if standing directly between those whispering.

1.2 Whispering Gallery Phenomena

In 1878, Lord Rayleigh explained what was occurring in the gallery [2] and named the phenomenon "whispering gallery" phenomenon after the location of its discovery within Saint Paul's Cathedral. He explained that the sound was constantly reflecting off of the wall as it travelled around. To prove this Lord Rayleigh set lit candles around the gallery and used a whistle as a sound source, measuring the flickering of the candles to determine the reach of the whistle. The intensity of the sound was shown to decay slower when bouncing along the wall. It decayed as the inverse of the distance it travelled, rather than as the inverse square as is the case with an outward radiating sound from a point source in free space.

While initially discovered for acoustic waves, whispering gallery phenomena applies to electromagnetic waves also. The research into the scattering of light from spherical particles is credited to papers published in 1908 by Gustav Mie [3] and Peter Debye [4]. In this instance, confining light waves does not require the same scale as the whispering gallery in Saint Paul's Cathedral due to the differences in the size of their respective wavelengths. To observe the analogous acoustic reflections in the optical domain, we can build a resonator out of a dielectric material. A large glass sphere is useful at visually demonstrating the confining of light when a laser of a visible wavelength is coupled into it. When this is set up correctly the light appears confined at the rim of the sphere. Due to the size of the sphere relative to the wavelength of light, the light appears to "bend" around the sphere as it travels (see figure 1.2).

1.3 Whispering Gallery Resonances

Let us take a moment to discuss how the confinement of a wave at the edge of a surface contributes to the satisfaction of the resonance condition: The repeated reflections of a wave around the rim of a surface will continue infinitely if contributions from absorption and scattering from the material are neglected. To neglect these components would quickly turn this into an unphysical system, so when those components are not neglected and there is no external driving force present to compensate, we recognise that a decay in the amplitude of the wave must occur. If one takes steps to promote the lifetime of the wave as it travels, the wave would eventually circumnavigate the space and traverse its origin on the rim. The overlap between the returning wave and the point of origin is dependent on the number of times it

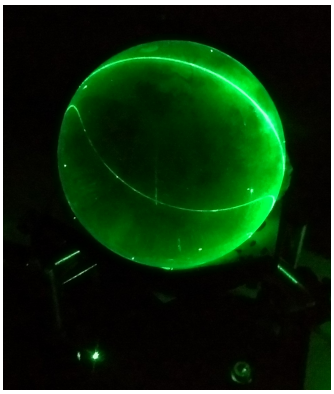

FIGURE 1.2: The light remains confined near the rim of this glass ball, analogous to how sound is confined to the rim of a whispering gallery.

is reflected while travelling. This is dependent on the geometry of the space and the properties of the wave. The frequency of the wave will determine the resulting phase offset the returning wave has with its point of origin. Certain frequencies will experience no phase offset, which will cause constructive self-interference. Similarly, there will be certain frequencies that return to the same starting point but exactly out of phase. This results in destructive interference and so these frequencies are suppressed in the WGMR. The constructive self-interference leads to an amplification of the wave, with the strongest amplification of the wave occurring at integer multiples of 2π after one circumnavigation by the wave.

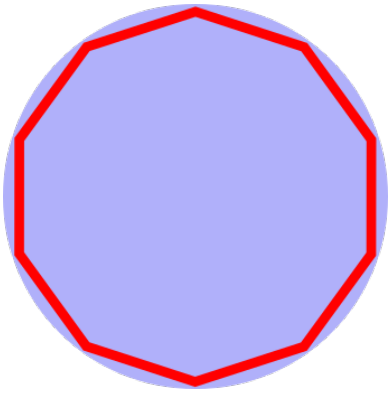

FIGURE 1.3: A ray optics illustration of WGMR resonance. A light ray is confined in the WGMR by continuous reflections at the rim.

This satisfies the resonance requirement as the amplitude of the frequency of the wave after travelling around the rim will exceed the amplitude of the frequency of the wave at the origin. We refer to the resonance frequencies formed in this manner as modes, hence the term whispering gallery modes. In the acoustic domain, Lord Rayleigh was able to generate the modes in the whispering gallery of Saint Paul's Cathedral by standing in the gallery and blowing on a whistle. The optical domain uses a different process to generate the modes. While there are several methods to do this, this thesis will focus on the method known as prism coupling using frustrated total internal reflection and will be discussed in detail in section 3.2.2. The discussion of modes in this section is kept brief but will be elaborated on in section 3.4.

1.4 Experiment Motivations

The experiment in this thesis is conducted with the objective of verifying a relationship proposed in Foreman et al. (2016) [5]. In this paper, it was suggested that a dielectric substrate could be brought into close proximity with a WGMR to detune a resonant mode.

This relationship was developed further, to suggest that changing the refractive index of the substrate would change the amount of frequency detuning. This relationship can be seen in figure 1.4 below. The amount of frequency detuning seen can also change depending on if the mode is transverse-electric (TE) polarised or transverse-magnetic (TM) polarised. Polarisation will be discussed in greater detail in section 5.1.1.

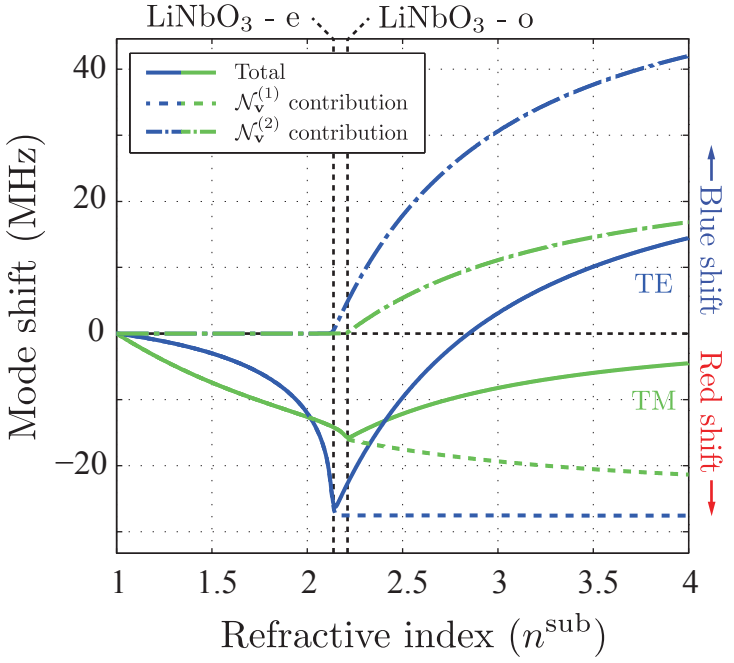

FIGURE 1.4: We note that the relationship between the refractive index of the substrate and the resulting frequency shift of the resonant mode is non linear. Of interest is an inflection point that occurs when the refractive index exceeds that of the resonator. We can also note that an anomalous blue shift is predicted for high refractive index values when using TE polarised modes. (Figure 3a taken from Foreman et al. (2016) [5])

Many interesting consequences occur from the relationship between refractive index and frequency detuning. We introduce the standard terms red-shift (a reduction in frequency) and blue-shift (an increase in frequency) to simplify explanations relating to these consequences. If a TE mode is observed, a red-shift is expected when the refractive index of the substrate is increased from 1. Once the refractive indices of the substrate and resonator match, a maximal red-shift occurs. What is perhaps more interesting, is that when the refractive index of the substrate is increased further, the magnitude of the red-shift decreases, eventually reaching a point where there is no frequency shift of the resonator mode. At this point the effects of the red-shift and blue-shift compensate each other, making it as if there is no substrate nearby. When the substrate refractive index is increased beyond this point,

a blue-shift of mode is expected. There are many anecdotal reports about noticing blue-shifts in experiments but there is little literature available that explores them in detail. One work that does is by Vogt et al. (2019) [6] in the THz domain. It is important to note that the presence of a blue-shift is unique to TE modes. TM modes were shown to exhibit a similar pattern of behaviour but without a blue-shift.

The purpose of the experiment in this thesis is to explore the relationship proposed in Foreman et al. and to verify if the relationship holds true for both TE and TM modes. To do this we must discretize the continuous refractive index scale. This is to generate a more physical setup whereby we can use substrates with a range of different refractive indices to form a relationship between the refractive index of the substrate and resulting frequency shift of the resonator mode.

The discussion of the relationship proposed in Foreman et al. was kept brief in this introduction, and will be revisited in section 4.1 with more detail.

1.5 Thesis Content

This thesis has chapters grouped together based on different aspects of the experiment. Chapter 2 and chapter 3 will focus on more of the background discussion away from the direct experimental context of the experiment presented in this thesis. The remainder of this thesis will focus on aspects of the experiment more directly, from discussions about aspects of the experiment of the results of the experiment itself:

- In chapter 2 we will spend some time illuminating the complicated process of fabricating a resonator in the lab. We will then move into a description of the processes involved with both polishing and cleaning a fabricated resonator.
- In chapter 3 we will discuss various aspects of WGMRs. This chapter will serve as the majority of the background required to understand the reasoning for steps taken in this experiment moving forward. Section 3.1 will outline the geometric structure of WGMRs and how birefringence influences the refractive index of a resonator when a particular polarisation of light is coupled into it. Section 3.2 will show how Snell's law plays a vital role in confining light to a WGMR using total internal reflection. We will then extend the theory of total internal reflection to account for light entering a resonator through evanescent field coupling. Section 3.3 will have a lengthy discussion about many of the aspects involved with coupling light into a WGMR. We will begin by coupling light from a fibre to free pace and continue discussion until a coupling spot is found by observing the presence of Newton's rings. Section 3.4 will introduce the nomenclature for characterising the spatial position of modes that are observed in WGMRs. We will take an example of this nomenclature to introduce the idea of fundamental modes. Section 3.5 will take at the values that can characterise WGMRs. We will discuss what the theory of each value with reference to their importance in this experiment before detailing a process of extracting the values experimentally.
- In chapter 4 we will study aspects of the experimental setup in greater detail: Section 4.1 will have us revisit the motivations behind this experiment in more detail. Here we will discuss the implications of moving from the theoretical conclusions of the background paper to the experiment devised in this thesis. Here we will analyse some of the results found in Foreman et al. and what they

mean for the experiment presented in this thesis. It is in this section that we also get the first introduction to the substrates used in this experiment through table 4.1. We will then move into section 4.2 where we will show the physical setup with which we run the experiment. The remainder of this chapter is focused on discussions around specific elements of the setup. Section 4.3.1 will examine the methods by which the computers communicate with lab apparatus. This is followed by a discussion around the two different types of positioning systems used (sections 4.4 and 4.5).

In section 4.3 we will elaborate on the automation processes employed in this experiment to facilitate data collection. We will conclude this chapter with an outline of some of the steps taken to mitigate potential error sources: the orientation of the substrate mounting (section 4.8) and the presence of thermal fluctuations (section 4.9).

- Chapter 5 focuses exclusively on the methodology of this experiment. This has two important aspects, the process for readying the setup before data is taken (section 5.1) and the process of running the experiment itself (section 5.2).
- The results of the experiment are broken down by the relevant substrate in chapter 6. We will also analyse the results in this chapter.
- This will leave a lot of the discussion to chapter 7, which will also serve as the future outlook of this experiment and the final chapter of this theses.

1.6 Outcomes During This MSc

While completing the research for this thesis, we had several positive outcomes. The research for this thesis was presented at the Dodd-Walls Symposium held in Auckland in July 2018. This research generated a high level of interest at this symposium with a lot of engagement during the poster presentation session in which this research was showcased. This discussion resulted in a competing work demonstrating a blue-shift measured in the THz domain [6], published in Optics Letters.

This research was also presented at the Frontiers in Optics Conference held in Washington DC in September 2018. At this conference there was a high degree of interest during the poster session that this research was presented. Many interesting discussions took place between myself and various attendees, some of whom were familiar with the field and some who were not.

Chapter 2

Whispering Gallery Mode Resonator Fabrication

This chapter will focus on the fabrication of resonators. This will include discussions around the apparatus used to fabricate the resonator. Once the fabrication process is complete the resonator is still unlikely to be useful in a setup. The resonator must be refined through bouts of polishing and cleaning before it will perform adequately in a physical setup. The process of polishing and cleaning a resonator will follow on from the conclusion of the fabrication process.

2.1 Fabrication Methods

There are different fabrication methods available for WGMRs depending on their intended use and the material they are fabricated from. Common methods are melting and re-flowing and single point diamond tuning. Melting and re-flowing does not work well for single crystalline materials as the fabrication process causes the resonator to become polycrystalline. If the resonator is polycrystalline then it loses its birefringence (birefringence is explained in section 3.1.2) which is an important property for our experiment in distinguishing between TE and TM modes (see section 4.1). Polycrystalline resonators can also have increased bulk and surface scattering. This will negatively affect the Q-factor (Q-factor is explained in section 3.5.3) of the resonator. This makes a single crystalline resonator more desirable than a polycrystalline resonator.

The resonator used in Foreman et al. is made from lithium niobate ($LiNbO_3$) so we also selected lithium niobate for our resonator material to increase compatibility. As this material possesses a single crystalline structure, we wish to preserve this for reasons explained above. This makes single point diamond tuning a more favourable fabrication method and will be the method discussed in this thesis. Single diamond tuning ensures that the fabricated resonator remains single crystalline.

2.2 Fabrication Component Discussion

2.2.1 Lathe

We use an air-bearing spindle lathe for fabrication. It is attached to an air compressor to reduce friction and achieve up to 6000rpm when using the turning machine. The object to be spun on the lathe is first inserted into a chuck and then twisted into the front of the lathe until tight As the object is twisted it lead to instabilities while using the lathe if it rotates eccentrically. There are calibration processes available to

mitigate this balancing issue that will not be detailed in this thesis so it is assumed the lathe is already balanced to a satisfactory level.

FIGURE 2.1: An image of the air-bearing spindle lathe and microscope where WGMRs are fabricated.

2.2.2 Turning Machine

The turning machine is a cutting arm mounted on the top of a platform with independently controlled x and y axis movement. This gives it a limited range of motion on one side of the lathe (see figure 2.2). A sharp single crystalline diamond tip is mounted at the end of the cutting arm and is used to cut the precursor into a resonator. The resonators fabricated in the lab possess rotational symmetry so the turning machine only needs access to one side of the resonator. We employ the use of a computer to make precise movements of the turning machine. We can use complex curves to shape the resonator

2.2.3 Paraffin Wax

We use paraffin wax as a mounting adhesive. It is used to mount a resonator material wafer onto a sheet of metal, to mount the resonator precursor onto a brass rod and to mount substrate windows onto aluminium slides.

There are many advantages to using wax over other adhesives. It retains a strong bond in the setup because the melting point is very high relative to the room temperature. The wax also doesn't have a curing time that other stronger adhesives have, meaning the object can be used once it has sufficiently cooled rather than after a certain amount of time has passed. This makes it especially useful when only minor adjustments need to be made to the position of something such as resonator precursor on the brass rod tip as often many small adjustments need to be made before the precursor is mounted satisfactorily.

To use the wax we first need to melt it into a liquid. This is done using a hot plate (see figure 2.3). The process for using the wax is as follows:

1. We set the hot plate to a temperature around the melting point of the wax. This temperature is around 110°C. We place a small glob of wax and object we want to mount something onto. This should be a metallic item such as the brass rod or aluminium slide. As these are metallic they conduct the heat well and allow the wax to be manipulated before it cools.

(A) Two uni-axial translators are mounted perpendicular to each other to produce a stage with a large rage of movement. It can be controlled through a joystick or via a computer. The clamps allow for objects to be mounted on it such as the diamond cutter (pictured right).

(B) The diamond cutter used for the fabrication of WGMRs. The diamond tip can be seen protruding to the right. The diamond tip can be exchanged using a screw. This allows for customisable precision with smaller or larger diamond tips based on the requirements.

FIGURE 2.2: A composite figure shows a diagram of the setup conditions and a photograph of the resulting reflected image from the prism onto a screen. The left image shows A possible coupling spot due to the presence of the interference highlighted in yellow. In the right image, the coupling prism is moved away from the resonator and the interference pattern disappears (compare the yellow highlights of the left and right images). This suggests that the interference seen in the left image is caused by the contact between the spherical surface of the resonator and the flat surface of the coupling prism, generating Newton's rings. The location of this interference suggests the presence of a coupling spot.

2. When the wax has melted into a pool a toothpick is used to collect a small amount and smear it on the item where something is to be mounted.

3. The item is removed from the hot plate carefully and pressed together with the object to be mounted and the toothpick is used to finely manipulate the position of the join while the wax is still hot and liquid.

4. When the position of the join is satisfactory the bound object has one of its metallic surfaces placed onto a heatsink. This speeds up the cooling process for the wax and allows the object to be used in a matter of minutes after the wax is applied. Suitable heatsinks include metallic bench vices or large blocks of metal.

2.2.4 Brass Rod

Brass rods are favoured to hold resonators for several reasons. They provide stable housing for the resonator, allowing for the changing of a resonator in a setup with relative ease. As the rod is brass, it is thermally conductive, making them useful in setups with temperature control. We employ a naming system of etching a resonator designation into the base. This makes it easy to distinguish resonators that are hard to distinguish by eye alone.

The end of the brass rod should have a tapered tip. This allows for a coupling prism to be brought into close proximity without impacting the brass and means the

FIGURE 2.3: The hot plate used to melt the paraffin wax for use in mounting objects in the experiment.

diamond tip of the turning machine does not need to cut the brass while it shapes the resonator. This leads to a reduction in wasted materials and prolongs the sharpness of the diamond tip.

2.3 Computer Control

We use a program written by a current PhD student to facilitate the fabrication process (see figure 2.4). Using the program allows for precise diamond cutter movements with greater precision than can be achieved by manually using a joystick. As we have precise control over the x and y movements of the diamond, we can combine movements in both the x and y directions to simulate a curve. This allows us to shape the curved rim of the resonator and allows us to control the major and minor radius (see section 3.1) of the finished resonator.

2.4 Lithium Niobate Resonator Fabrication Process

Here we will detail the steps taken to fabricate a resonator using single point diamond tuning.

2.4.1 Drilling The Precursor

The resonator materials often come in the form of a wafer. We need a way to drill a small piece of the wafer out to be used in fabricating a resonator. The method we use is to mount a hollow core brass drill bit with in the lathe and push the wafer mounted to a thin metal sheet into the bit as it rotates in the lathe. We add high grain size diamond slurry to the contact point between the drill bit and the wafer to facilitate the drilling process. We can adjust the size of the resonator precursor by changing the size of the brass drill bit mounted in the lathe. The purpose of the metal sheet is two-fold. Firstly it gives stability to the drilling process by reducing the risk of fracturing given the brittle nature of some materials like lithium niobate. Secondly it serves as a novel feedback system for determining when the drilling process has completed. This process involves connecting the brass drill bit and the metal sheet underneath the wafer with a LED bulb and battery. When the drilling has completed, the brass drill bit and metal sheet will contact, completing

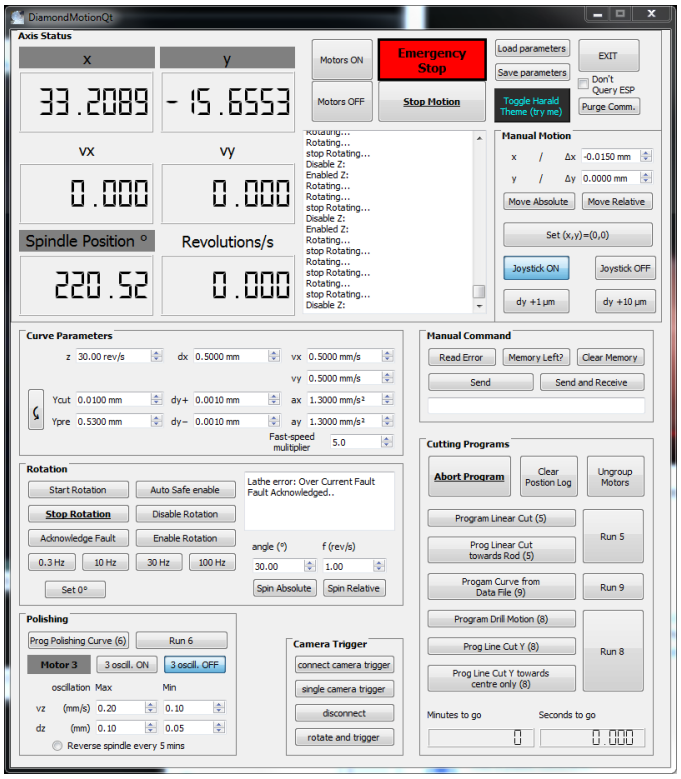

FIGURE 2.4: A screenshot of the program used to control the turning machine when fabricating WGMRs.

the circuit and turning on the LED. With the feedback circuit in place and the lathe rotating at 6000rpm we bore a small cylindrically-shaped resonator precursor out of the wafer. The precursor should have a 100 µm radius larger than the desired resonator radius. This is a safety threshold so that cracks in the surface of the precursor can be removed without changing the desired radius of the resonator.

Once the wafer has been drilled, the metal sheet and wafer can be placed on the hot plate and the precursor can be extracted from the wafer once the wax has melted. The precursor should be cleaning by wrapping it in lens tissues and placed into a beaker with a small amount of acetone. This beaker is then placed into a hyper-sonic bath that cleans excess wax, diamond slurry and other debris from the precursor.

2.4.2 Mounting The Precursor

Once we have a suitable precursor, this is removed from the wafer and mounted on the end of a brass rod. The precursor should be mounted flat on the end of the resonator, as the turning machine operates perpendicular to the long axis of the rod. This means any deviations from flat can give rise to eccentricities in the final shape of the resonator. The 'flatness' of the precursor can be checked on a microscope eyepiece that has a gird. The resonator edge is aligned with a grid line under the microscope. If the resonator is then rotated along the rod axis, one rotation should see the edge of the resonator remain near the specified grid line. Large deviations from the grid line as it rotates suggests that the resonator is not mounted flat on the brass rod.

We devised a way to help ensure the precursor is flat upon the brass rod tip using a large press and a height adjustable stage (see figure 2.5). We place a leveler on the press so that we can tell that the press is flat, then adjust the height of the stage such that the press starts to push the precursor down on the brass rod. This is most effective when the brass rod is on the hot plate as the wax needs to be soft to change the position of the precursor.

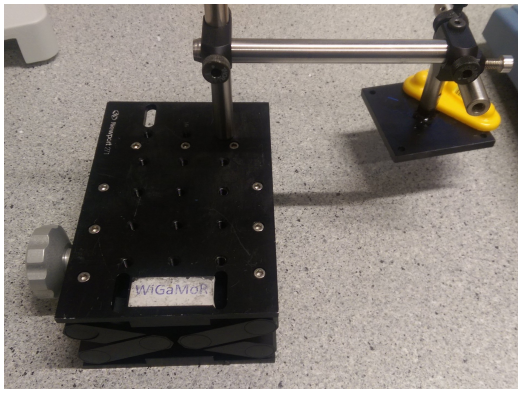

FIGURE 2.5: The device we made to help ensure a resonator precursor was mounted flat on a brass rod tip. The yellow leveller is used to make sure the press is flat.

2.4.3 Cutting The Resonator

The precursor is then cut into the shape of the desired resonator. This is using the diamond cutter and turning machine. For lithium niobate resonators, they should be cut in accordance with the negative rake angle, cutting speed and cutting depth specified in section. This should be done in steps with a surface inspection by microscope to ensure there are no cracks or breaks in the material.

The rake angle and feed rate of the diamond cutter are carefully controlled to ensure that the finished resonator has a high surface quality. Rake angle and feed rate are the two parameters that have the most impact on the final surface quality of a fabricated resonator. Rake angle is the angle between the surface normal of the precursor and the diamond cutter (see figure 2.6). A negative rake angle is found to have better results for brittle substances like lithium niobate. The diamond cutter is mounted below the equatorial plane of the brass rod to ensure a negative rake angle is obtained. A positive rake angle can chip or break the material during the fabrication process. The best rake angles are found anecdotally to be between -20° and -25° for lithium niobate.

The feed rate is a measure of how far the diamond cutter travels while the precursor undergoes one revolution. The diamond cutter should approach at a maximum speed of 25 µm/s and have a maximum cutting depth of 2 µm.

2.5 Polishing of WGMRs

When the cutting process has been completed after enough steps, polishing will be required to ensure an optically smooth surface around the resonator. Polishing can take place immediately after a resonator is cut as they are both done on a lathe.

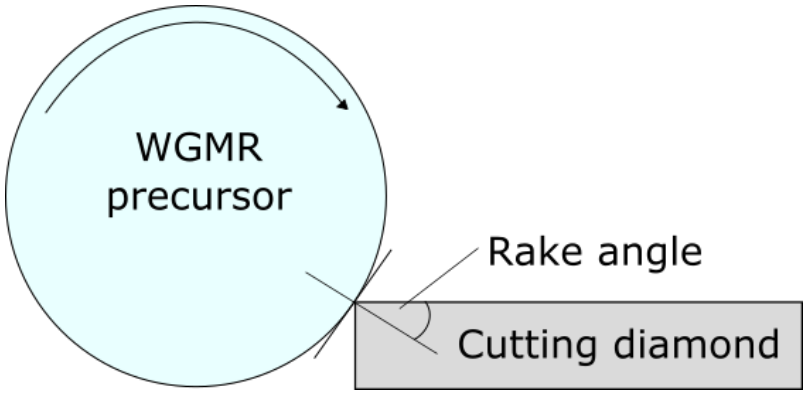

FIGURE 2.6: A schematic of the negative rake angle used when fabricating WGMRs.

The optically smooth surface is the result of removing any imperfections in the resonator. These imperfections often take the form of scratches, chips or indents. We can often see imperfections in the reflections of the resonator when looked at under a microscope. The lathe microscope shows two light spots in the top of the resonator and rotating the resonator can highlight imperfections when they cause a change to these light spots . The polishing is done by hand with a spin speed of 60rpm. We use diamond slurries with varying sizes of diamond grains to polish the resonator. A lens cleaning tissue is folded in half multiple times to build an edge where a slurry can be applied and held to the resonator while it spins. The grain size in the slurry will usually start at 9 µm or 3 µm depending on the degree to which the resonator needs polishing. At these grain sizes the slurries are often in a water based solution however for finer grain sized slurries the particles are suspended in a grease solution, requiring a drop of distilled water applied to the resonator or slurry before polishing. The grain size of the slurry can be reduced to provide a finer polish and therefore an increased optical smoothness in the resonator. The application spot on the folded tissue should be changed when a different sized slurry is used to avoid scratching the surface with residual large diamond particles. The resonator should also be cleaned with isopropanol in order to remove any excess slurry before a smaller grain is applied. When the polishing process is complete and the surface appears smooth under a microscope, the resonator can be cleaned to remove any excess slurry.

2.6 Cleaning of WGMRs

Cleaning a resonator is done by hand on the lathe with a spin speed is set to 30rpm. Cleaning alcohols like isopropanol or ethanol can be applied to a lens tissue and wiped along the surface of the resonator. The process is best done by beginning with the top of the resonator and moving the tissue towards the base of the rod. This motion is repeated along the resonator and ensures that any detritus collected is pushed in the same direction and away from the resonator. Otherwise random cleaning motions might only serve to smear the detritus around and result in little change to the cleanliness of the resonator. A dry lens tissue is used to ensure the cleaning alcohols are wiped away from the resonator. They evaporate but can sometimes leave a residue that causes chromatic aberration when looking at the resonator surface under a microscope. These aberrations can sometimes mask particles

FIGURE 2.7: An image of the different diamond slurries used to polish WGMRs. They are labelled by the grain size of the diamonds within them and kept seperate from each other to prevent cross contamination.

that would reduce the optical smoothness of the resonator and so they should be removed if possible.

2.7 Maintenance of WGMRs

If a resonator that is placed in a setup begins to behave more poorly it is useful to place it in the lathe and observe it under a microscope. Often times the image under the microscope can diagnose why a resonator might suddenly perform worse. Below is a quick description of what to look for to diagnose poor resonator performance while observing the resonator in the microscope:

- Often times dark spots that appear around the resonator rim can be a sign of dust tat can be fixed by repeating the cleaning process.
- If cleaning has removed the spots but has caused chromatic aberrations of either the light points in the rim from the microscope lamp, or any spots that appear rainbow in colour, this can be a sign of residue remaining on the resonator. This can be solved by properly drying the resonator after cleaning.
- If the reflected lamp light points change shape or reflection intensity asymmetrically as the resonator is rotated, this can be a sign of an asymmetric change in shape of the resonator., in the form of a dent or mark. If cleaning does not fix the issue the resonator will likely need to be re-polished.

Chapter 3

Whispering Gallery Mode Resonators

In this chapter we will look in more detail at various aspects of WGMRs. We will discuss the structure of a resonator before a detailed discussion of the process of total internal reflection. This will serve as laying the groundwork for discussions around how light couples into the resonator. This will be done in two parts. The underlying process will be discussed with an outline of frustrated total internal reflection, before moving through the physical process undertaken to actually couple light into the resonator. Once we have established how light couples into the resonator (both in theory and in practice) we will discuss what one can see on an oscilloscope when the coupling process is complete (resonator modes). Armed with the knowledge of understanding what is being seen, we will extend this discussion into the characterisation of these modes, both in characterising their spatial location in the resonator and useful measurements that can be performed on the modes to increase our understanding of what is happening inside the resonator. This chapter will conclude with an explanation of how one goes about obtaining the useful measurements when the resonator is in a physical setup.

3.1 WGMR Structure

3.1.1 Geometry

WGMRs often possess spherical or rotational symmetry. This is often achieved by fabricating a disk made from a dielectric material that contains a major radius R and a minor radius r.

A WGMR can have different "cuts" referring to the location of the optical axis relative to the resonator. When the optical axis is parallel to the axis of rotational symmetry (denoted as the z-axis from figure 3.1), we refer to the resonator as a z-cut resonator. One can fabricate a resonator with the optical axis parallel to the x-axis (x-cut resonators [7]) or at an arbitrary angle relative to the z-axis (angle-cut resonators [8]). This thesis will almost exclusively refer to z-cut resonators.

3.1.2 Birefringence

In resonator materials such as lithium tantalate, barium tetraborate or lithium niobate, the refractive index is dependent on the direction of the polarisation of the light within it. This is a property known as birefringence and means that different polarisations of light will interact with different refractive indices within the same crystal. A birefringent crystal will have two refractive indexes, an ordinary refractive index

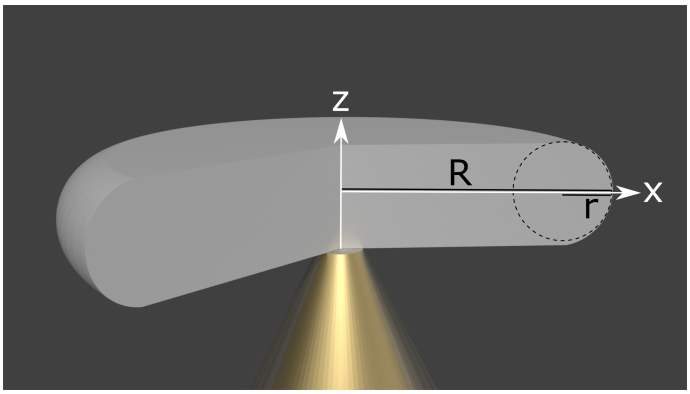

FIGURE 3.1: Structure of a WGMR. The difference between the major radius R and the minor radius r can be noted from their positions on the figure.

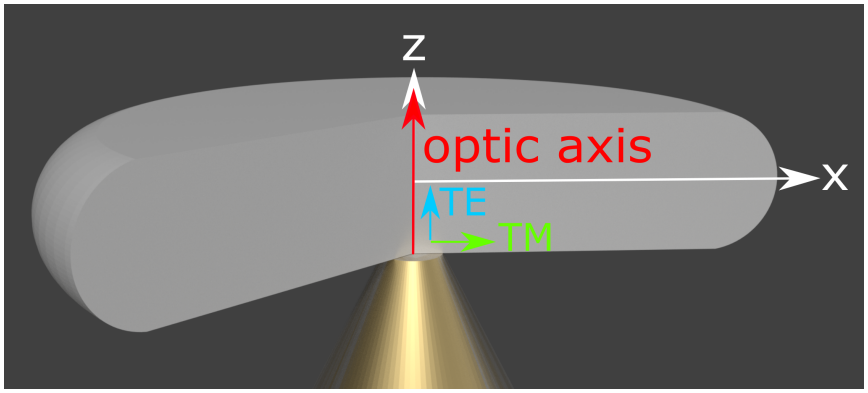

FIGURE 3.2: An illustration of the optical axis in a z-cut resonator. TE and TM directions are also shown.

(denoted as n_o) and an extraordinary refractive index (denoted n_e). Based on the direction of the optical axis in a crystal, light polarised parallel to the optical axis will experience the extraordinary refractive index and conversely light polarised perpendicular to the optical axis will experience the ordinary refractive index.

If we now introduced polarised light into the resonator, transverse-electric (TE) polarised light (light polarised perpendicular to the WGMR place) will experience the extraordinary refractive index and transverse-magnetic (TM) polarised light (light polarised parallel to the WGMR place) will experience the ordinary refractive index of the resonator. Due to the rotational symmetry of a z-cut resonator, the refractive indices experienced by the different polarisations of light are constant regardless of the position along the rim of the resonator where light is coupled in.

3.2 Total Internal Reflection

We described how a wave was able to "stick" to a curved surface as it travelled earlier in section 1.2 but here we explain the underpinning principle in more detail. The confinement of a wave along a curved surface is a result of total internal reflection (TIR). Here we will discuss Snell's law and the condition for TIR to occur. The process by which we actually couple light into a resonator uses an extension of TIR

known as frustrated total internal reflection (FTIR). It is useful to cover FTIR below before we talk about coupling more broadly in the following section (3.3).

3.2.1 Snell's Law

TIR is a consequence that is derived from Snell's Law. Snell's law describes how a wave is refracted as it travels across a boundary between two different mediums, such as water and air. The angle that it will refract at is dependent on the refractive indices of the media and the angle of incidence it makes with the boundary. This relationship is written as

$$n_1 \sin(\theta_1) = n_2 \sin(\theta_2). \tag{3.1}$$

If we take the limit where θ_2 approaches 90°. We would find that the wave no longer passes across the boundary, but rather travels along it. We denote this as the critical angle

$$\theta_{\text{critical}} = \arcsin\left(\frac{n_2}{n_1}\right). \tag{3.2}$$

If the angle of incidence exceeds the critical angle ($\Theta_1 > \Theta_{\text{critical}}$) then the wave will reflect at the media boundary, giving rise to the term totally internal reflection. This can only occur in instances where $n_1 > n_2$ in accordance with the critical angle formula. This explains why TIR can occur in the whispering gallery in St. Paul's cathedral, due to the interface between air and stone. This also explains how light is internally reflected in a WGMR, due to the interface between the resonator material and air. The process for TIR is illustrated in figure 3.3.

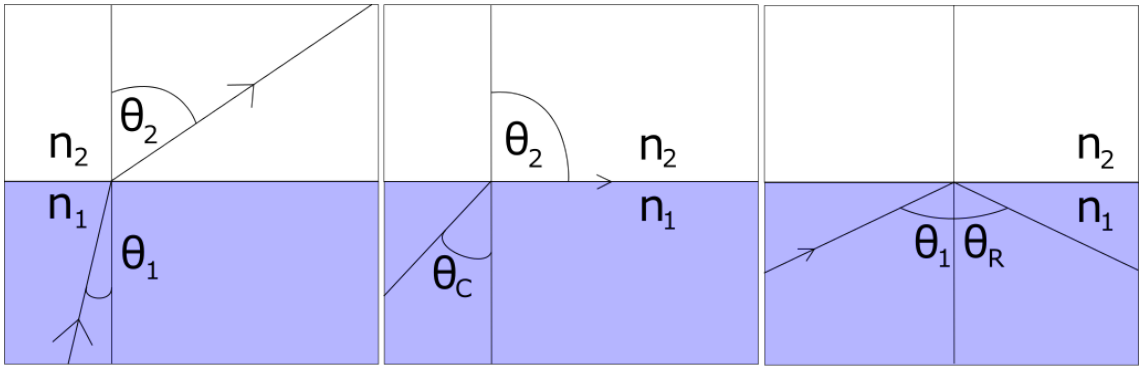

FIGURE 3.3: An illustration of total internal reflection.

3.2.2 Frustrated Total Internal Reflection

Frustrate total internal reflection is an extension of total internal reflection. Even if an incident wave is entirely reflected through the process of TIR, it will still produce an evanescent wave (see figure 3.4). This wave will ordinarily transmit zero energy, however if we introduce a dielectric prism into the field of the evanescent wave, the evanescent wave can become a propagating wave again. If the prism has a higher refractive index than the resonator $n_{\text{prism}} > n_{\text{resonator}} > n_{\text{air}}$ then the energy transmitted to the resonator can be enough to excite a wave that can continue propagating. Doing this creates an evanescent coupling channel which allows light

to 'tunnel' into the resonator. Evanescent waves decay exponentially if there is no third media in close proximity for it to propagate in.

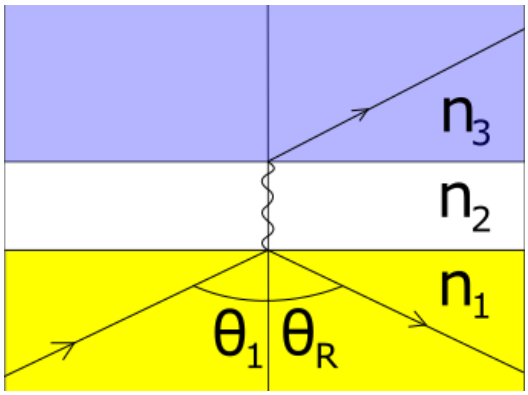

FIGURE 3.4: An illustration of frustrated total internal reflection. This diagram represents the interaction at the prism-resonator boundary, TIR occurs within the prism but the nearby WGMR opens an evanescent coupling channel, thus emitting light from the prism into the resonator.

3.3 Coupling

We have discussed how light remains in a resonator but one might wonder how it's possible to introduce light into a resonator in the first place. It is common to use prism coupling [9] or tapered fibre coupling [10] to couple light into a WGMR. This thesis will only focus on prism coupling due to its relevance to the experiment. The name arises from the reliance of this method on the introduction of a dielectric prism to the coupling environment.

There are several important steps to utilising prism coupling, we must couple light to free space such that we can refract it into a prism. We must ensure that the refraction into the prism at the correct angle to couple into the resonator. Next we use a screen to see the reflection of off of the back side of the prism that will help to find the coupling spot. Once the coupling spot is found, we need to be able to detect if there are resonant modes present in the resonator. It is advised to complete most of the coupling process using a laser in the visible spectrum and revert to the desired wave-length once the resonator has been coupled into. This section will elaborate on each step of the coupling process.

3.3.1 Free-Space Coupling

Optical fibres are great at allowing light to move over vast distances without losses but one cannot use a fibre to shine light into a prism. We must first couple the light from optical fibre into free-space. To do this we need three things, a graded index (GRIN) lens, a pig-tailed ferule and a glass mating sleeve. We fix the GRIN lens to one end of the mating sleeve using super glue or other form of strong adhesive, as the GRIN lens will not need to be moved once it's fixed in the sleeve. We then place the pig-tailed ferule in the other end of the sleeve.

A pig-tailed ferule bares resemblance to an optical fibre patch cable that has been cut in half. They have a fibre optic terminator at only one end, and we use the non-terminated end with the GRIN lens to couple the light to free space.

A GRIN lens is a lens that has a refractive index that varies radially. They are generally used in collimating or re-imaging fibre optic cable outputs, especially when paired with a pig-tailed ferule.

We do not fix the pig-tailed ferule in the mating sleeve like we did the GRIN lens. This is because we can gently move the pig-tailed ferule forwards or backwards in the plastic mating sleeve and it will change the numerical aperture of the free-space coupling. This has the effect of adjusting the focus of the light which is necessary to reduce the out-coupled beam profile to ensure as much light as possible strikes a detector chip.

It is recommended to attach the mating sleeve with the pig-tailed ferule and GRIN lens to a xyz translator stage. This makes fine adjustment of the laser position easier and will be vital when finding the coupling spot (see below) and optimising modes (see section 3.4 below).

3.3.2 Prism Movement

We need to ensure that the prism is in contact with the resonator such that the coupling spot is visible in the reflected image from the prism. To do this we use an Attocube nano-positioning system to move the prism into contact with the resonator. The mechanism for this movement will be discussed further in section 4.5 but it is important to mention this step during the coupling process.

3.3.3 Coupling Angle Calculation

To ensure the highest probability of light coupling into the resonator, we solve Snell's law to find the optimum angle for an incident wave to enter the coupling prism from free space. Light entering the prism at the optimum angle undergoes FTIR with the best conditions to emit into the resonator. The calculation of this angle is more complicated than plugging the respective values into equation 3.1 above. The internal angles of the coupling prism complicate the optimum coupling angle as light must first refract into the prism before it can undergo FTIR.

We assume that the coupling prism is in contact with the resonator, and that the plane of the prism in contact with the resonator is parallel to the tangent of the resonator (see figure 3.5). We define this plane to be the 'coupling plane'. We make several assumptions to simplify the derivation. We consider the case for triangular coupling prisms with either isosceles or equilateral geometry. This simplifies the calculations as we don't need to consider the angle difference between the incident wave and the out-coupled wave. We also assume that the resonator and prism are surrounded by either air or vacuum and that neither the prism nor the resonator have any coating that would influence their refractive index. We only consider the case for TE polarised light however this can be extended to TM polarised light without too much added difficulty. Finally we assume that the prism is isotropic and that the resonator is a z-cut.

Let the refractive index of the coupling prism be n_{prism} and the refractive index of the resonator be $n_{\text{resonator}}$. We define the angle the incident light ray makes with the normal of the side of the coupling prism as γ, we can calculate the refracted wave angle θ_1 using Snell's law (3.1)

$$\theta_1 = \arcsin\left(\frac{n_{\text{air}}}{n_{\text{prism}}}\sin\gamma\right). \tag{3.3}$$

We then implement the critical angle condition for FTIR to occur on the coupling plane. Let the angle that θ_1 makes with the coupling plane be β. We can express this using the form of equation 3.2 where

$$\beta = \arcsin\left(\frac{n_{\text{resonator}}}{n_{\text{prism}}}\right). \tag{3.4}$$

The wave now reflects off of the coupling plane, the presence of the resonator opens a coupling channel and light couples into the resonator. Due to the symmetry from specifying isosceles or equilateral triangular prism geometry, the wave is refracted across the prism-air boundary at the same angle γ. The final step is to formalise how this fits together with the interior angles of the coupling prism. Let us define the isosceles angles as α. Using this definition we can redefine γ as

$$\gamma = \arcsin\left(\frac{n_{\text{prism}}}{n_{\text{air}}}\sin\left(\beta - \alpha\right)\right). \tag{3.5}$$

This definition causes the optimal coupling angle (θ_{optimum}) to fall out of the equation as

$$\theta_{\text{optimum}} = 90 - \alpha - \gamma. \tag{3.6}$$

The optimal coupling angle is defined as the angle made between the coupling plane and the incident light to the prism (as can be seen in figure 3.5). This definition is a stable reference point that allows the interior angle of the coupling prism to change without changing how the optimum angle is measured. To have a stable reference point also makes it easier to adjust the angle later if the setup changes. We used a permanent marker to draw a crude protractor on the optical table by the setup as a coupling angle reference.

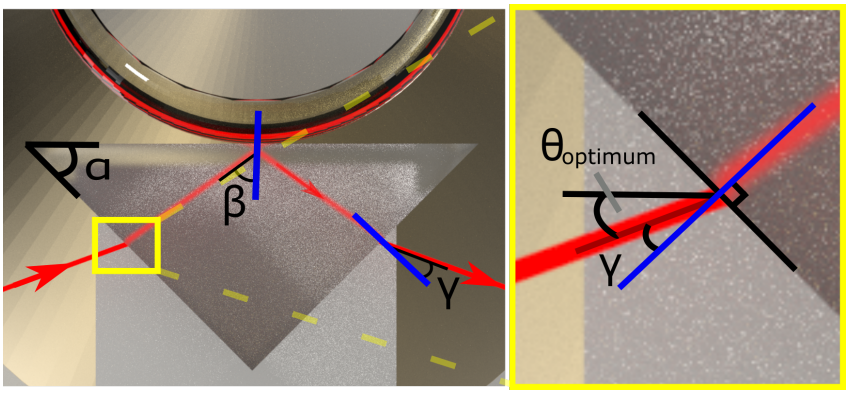

FIGURE 3.5: A diagram of the coupling prism with annotations describing the angles used to calculate the optimum coupling angle. The normals at the boundaries are drawn in blue The left image is an expanded look at the incident light wave entering the prism. Here the difference between the incident angle for Snell's law γ and the angle with the coupling plane θ_{optimum} can be clearly distinguished.

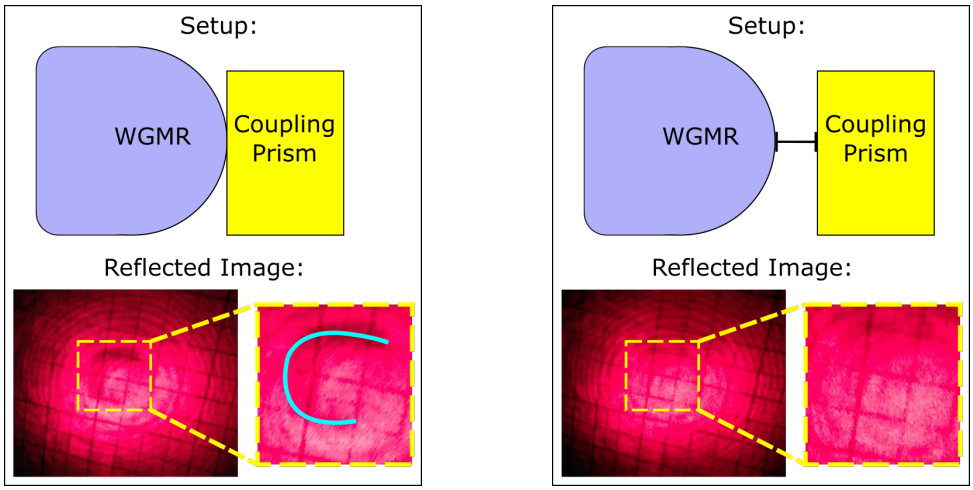

(A) The reflected image shows a potential coupling spot. Indicated by the presence of a circular interference pattern with a notable dark fringe along the top and right of the pattern. This has been framed in yellow for clarity. A zoomed in crop of the frame is seen to the right with an arc drawn in blue to direct the eye to where the fringe can be seen.

(B) This is the same reflected image but with the WGMR and coupling prism no longer in contact. This causes the dark fringe previously seen to disappear. As the presence of the dark fringe is dependent on the distance between the WGMR and coupling prism, this indicates the location of the coupling spot.

FIGURE 3.6: A composite figure shows a diagram of the setup conditions and a photograph of the resulting reflected image from the prism onto a screen. The left image shows A possible coupling spot due to the presence of the dark fringe framed in yellow. In the right image, the coupling prism is moved away from the resonator and the interference pattern disappears (compare the yellow zoomed image of the left and right images). This suggests that the interference seen in the left image is caused by the contact between the spherical surface of the resonator and the flat surface of the coupling prism, generating Newton's rings. The location of this interference suggests the presence of a coupling spot.

3.3.4 Newton's Rings

We want to find the point where the resonator rim is the closest to the coupling plane. This will produce a unique interference pattern known as Newton's rings (see figure 3.6). This interference is caused by a curved surface (the resonator) being in contact with a flat surface (the coupling prism).

We set up a screen to observe the reflected light from the prism. We can then adjust the pig-tailed ferule distance in the mating sleeve to zoom in or out of the reflected image. We can then adjust the reflected image by adjusting the position of the light entering the prism using the xyz translation stage. There are many sources of interference when looking at the reflected image, however only one spot will be caused by the resonator. Other interference is typically due to dust or other debris collecting on the prism or resonator. When the potential coupling spot has been identified, it can be tested by moving the coupling prism away from the resonator and returning it to contact. If the coupling spot has been identified correctly, moving the prism away also removes the Newton's rings from the reflected image. This is because introducing a gap between the resonator and prism violates the condition for Newton's rings to appear, yet returning the prism to contact will also return the Newton's rings to the reflected image. This makes it very easy to check whether identified interference is the coupling spot or not.

Once the coupling spot has been correctly identified then we use the translation stage dials to centre the coupling spot on the reflected image. We then adjust the numerical aperture of the coupling lens to reduce the beam profile as much as possible. Reducing the beam profile while centred on the coupling spot can allow enough light to couple into the resonator, often giving it a faint glow from Rayleigh scattering on the rim (see figure 3.7). Finally we introduce a detector in place of the screen to catch the out-coupled light from the prism. This can be combined with a focussing lens to ensure the detector is capturing as much light from the setup as possible.

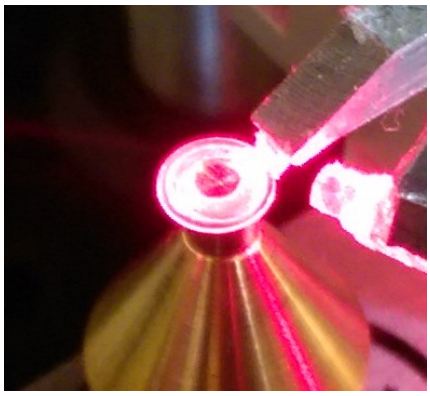

FIGURE 3.7: An image of the glow on the resonator produced by Rayleigh scattering. This can be seen when enough light can couple into a resonator during the coupling process.

3.4 Mode Observation

Connecting the detector to an oscilloscope will not automatically show modes. Here we will discuss how the light entering the detector reveals the presence of modes in the resonator. Referring back to section 1.3, we noted that we need to encourage constructive self-interference to fulfil the resonance condition. As this can only happen with certain frequencies of light we need a way of adjusting the frequency of light coupling into the resonator.

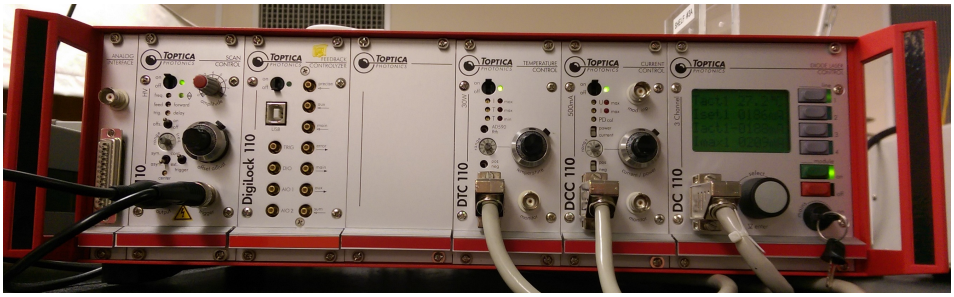

FIGURE 3.8: An image of the controller we use to manage the 1550 nm laser. Of note are the modules present, scan control, temperature control and current control. Adjusting these can change how the laser performs.

We use a Toptica Photonics SYS DC110 to control the 1550 nm laser. One of the modules we use in the control rack is a scan control module. The scan control uses

a piezo to rotate an internal grating that adjusts the frequency of the output light. The scan control module has a scan frequency range of 0.01 Hz to 10 kHz and an adjustable offset. We set a large frequency scan amplitude to sweep over a large frequency range. Sweeping over a large frequency range is more likely to find a resonant frequency. The scan control can produce sawtooth signals for the piezo, that come symmetrically or asymmetrically. An asymmetric wave contains a longer ramp up, retaining the same frequency information but spread over a greater number of samples on the oscilloscope. This gives us a greater resolution of the frequency sweep than the symmetric wave would be capable of. We trigger the oscilloscope off of the scan control trigger to see this longer frequency ramp on the oscilloscope. Adjusting the numerical aperture of the light is anecdotally the fastest and only step needed to observe modes on the oscilloscope. This should be sufficient before one needs to adjust any dials on the x-y-z translator stage.

Modes are observed as dips on the oscilloscope trace. These dips occur because the modes are at frequencies that are resonating so they do not out-couple to the detector. We use a combination of the prism-resonator distance and the x-y-z translation stage dials to increase the contrast between the observed modes and the baseline detector reading. Once this process is complete the oscilloscope should show clear modes similar to that seen in figure 3.9.

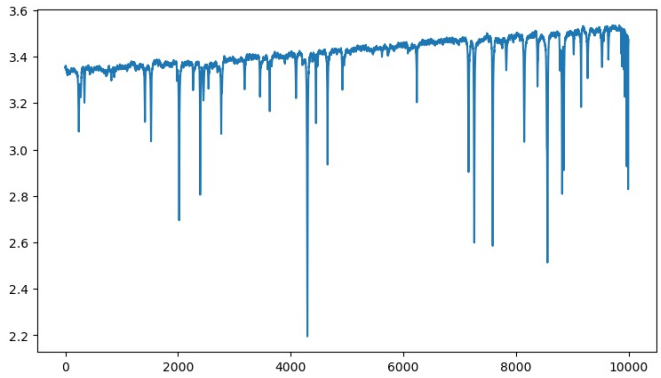

FIGURE 3.9: An image of the oscilloscope showing WGMs. The x-axis hasn't been calibrated for frequency yet so it shows the sample number.

3.4.1 Modes Characterisation

Modes that are seen in a resonator can be characterised with three components. These components serve to give an indication of the spatial location of the mode within the resonator. The three components are:

1. The azimuthal mode number m. This number denotes the number of oscillations in the plane of the resonator.
2. The polar mode number p. This number denotes the number of minima in the polar direction
3. The radial mode number q. This number denotes the number of maxima in the radial direction.

Examples of modes with differing mode numbers can be seen in figure 3.10 below.

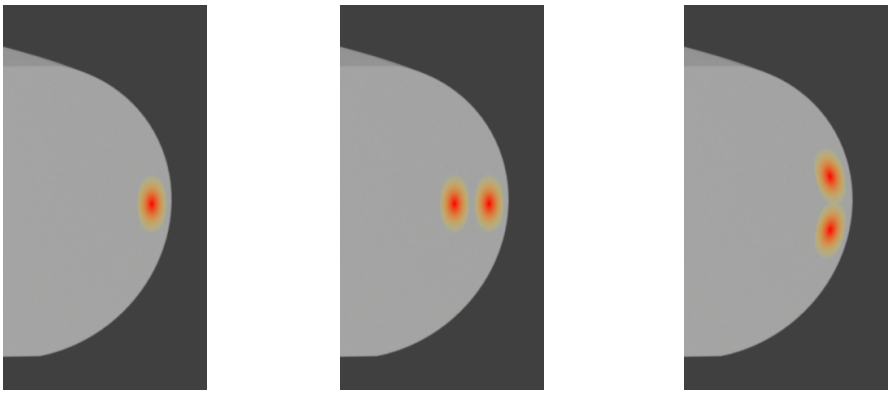

(A) Depiction of a mode with $q = 1$, $p = 0$. This is a fundamental mode.

(B) Depiction of a mode with $q = 2$, $p = 0$.

(C) Depiction of a mode with $q = 1$, $p = 1$.

FIGURE 3.10: An artistic rendering of the spatial location of modes based on mode numbers. The dots in each figure are made to represent localised electric fields within the resonator (not to scale).

Fundamental Modes

A fundamental mode is a mode that has $q = 1$ and $p = 0$ (see figure 3.10a). These were the modes used by Foreman et al. to derive the relationships of interest. A process for identifying fundamental modes is presented in Breunig et al. (2013) [11]. One can obtain the radial mode number q by measuring the free spectral range (see section 3.5.4 below) of many modes in the WGMR and stratifying the data by the free spectral range. The stratification of the data corresponds with the radial number, meaning modes in the lowest strata will have a radial mode number of $q = 0$.

3.5 WGMR Characterisation

Studying a mode can yield a lot of useful information. In this section we will look at several of the common measurements done on resonator modes. We will first look at the theory for a measurement before we elaborate on the experimental procedure for obtaining the values.

3.5.1 Linewidth

The linewidth of a mode is the full width half maximum (FWHM) of a Lorentzian fit to a particular mode. It gives us an indication of the amount of time that light spends in a resonator.

3.5.2 Coupling Contrast

The coupling contrast of a resonator is a measure of how much light enters a resonator compared to how much light dissipates. This can be calculated using the equation

$$K = \frac{P_{\text{in}} - P_{\text{out}}}{P_{\text{in}}} = 1 - \frac{P_{\text{out}}}{P_{\text{in}}}. \tag{3.7}$$

The ratio between the light entering (P_{in}) and light dissipating (P_{out}) affects the contrast between the edges of a mode and the depth of its centre. Based on the

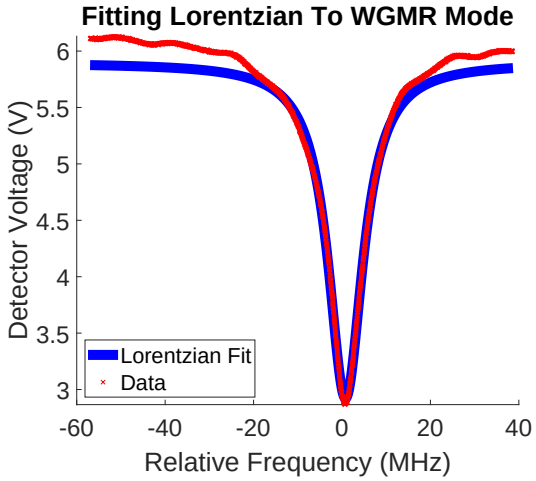

FIGURE 3.11: A Lorentzian fit applied to a WGM of interest.

relative sizes of light entering and light leaving there are three different coupling regimes possible for a WGMR:

1. *Under coupling*, where $P_{\text{out}} > P_{\text{in}}$. In this regime, the coupling contrast is small so modes are harder to distinguish from background noise. The linewidths are also small making the frequency of a mode easier to determine. See figure 3.12b.

2. *Critical coupling*, where $P_{\text{out}} = P_{\text{in}}$ means $K = 1$. In this regime, the resonances have a maximised coupling contrast, making modes easy to distinguish from noise during data analysis. This regime also increases the linewidth of resonances. See figure 3.12c.

3. *Over coupling*, where $P_{\text{out}} < P_{\text{in}}$. In this regime, the coupling contrast is reduced compared with the critical coupling regime. The linewidth is maximised in this regime resulting in greater uncertainty of the mode frequency. See figure 3.12d.

The third plot in figure 3.13 illustrates the differences between these regimes. Changing the distance from the coupling prism to the resonator changes the coupling contrast. This response is non-linear due to the exponential behaviour of the evanescent field. Due to the relative ease of changing this distance, it makes it easy to adjust the strength of the resonator coupling mid-experiment.

3.5.3 Quality Factor

The Q factor is a measure of the inverse of a resonators linewidth relative to its (resonant) frequency. It determines how much energy is lost compared to the energy stored in the resonator. Q factor is given by

$$Q = \frac{f_{resonant}}{\Delta f}. \tag{3.8}$$

This is often referred to as the total or loaded quality factor (Q_T). This can be separated into the intrinsic quality factor Q_0 and the coupling quality factor Q_C components by

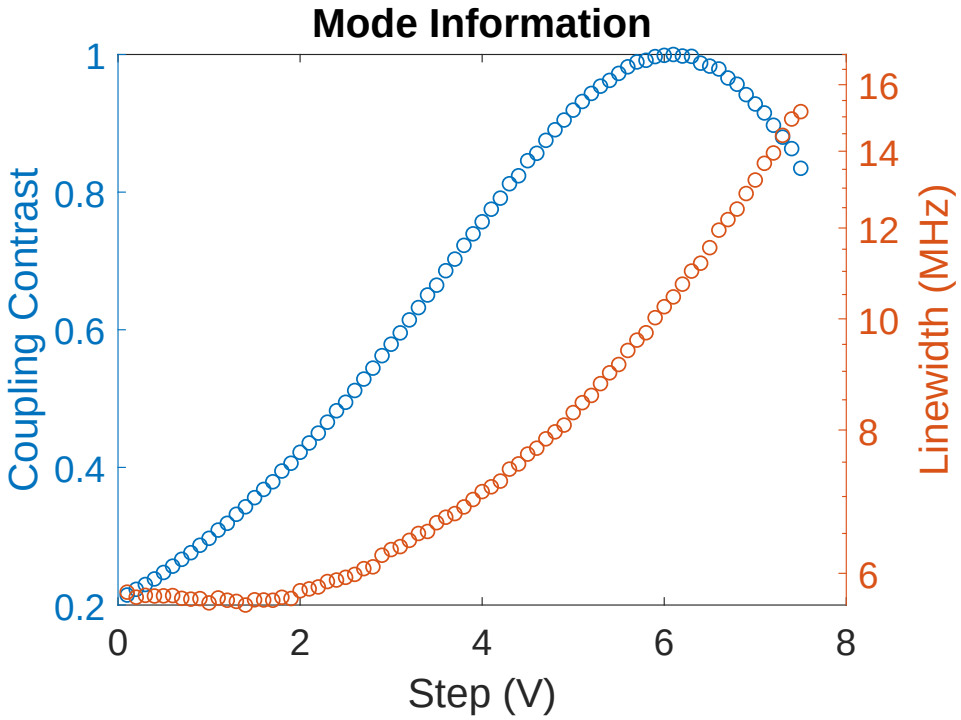

(A) The effect on coupling contrast and linewidth of changing the distance between the coupling prism and resonator.

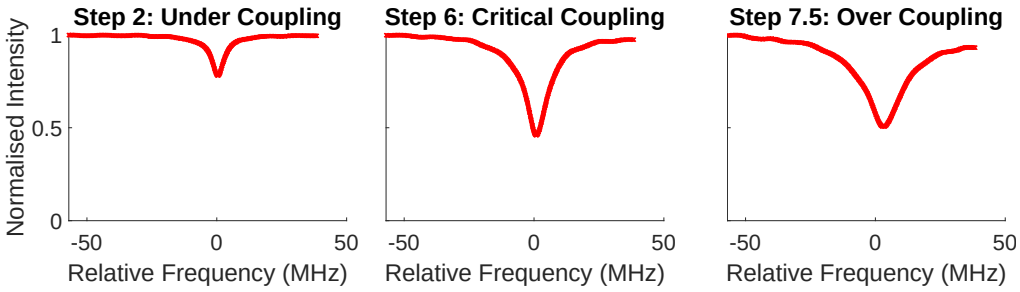

(B) The mode at step 2. Here we can see that the mode is under coupled due to the small linewidth and low coupling contrast observed at this step on figure 3.12a.

(C) The mode at step 6. Here we can see that the mode is critically coupled as the coupling contrast observed in figure 3.12a is maximised at this step.

(D) The mode at step 7.5. Here we can see that the mode is over coupled due to the decreased coupling contrast when compared to critical coupling and the increased linewidth observed at this step on figure 3.12a.

FIGURE 3.12: We observe a mode and save a trace after changing the position of the coupling prism incrementally. Figure 3.12a shows the results of fitting a Lorentzian to this mode at each increment, allowing us to observe how the linewidth and coupling contrast change with the distance between the coupling prism and the resonator. The distance was changed by incrementing the voltage of a piezo in steps of 0.1 V, with each increment moving the coupling prism closer to the resonator, reducing the distance between them. This was repeated 75 times. The figures 3.12b-3.12d show the mode at different distances illustrating the different coupling regimes.

$$\frac{1}{Q_T} = \frac{1}{Q_0} + \frac{1}{Q_C}. \tag{3.9}$$

When the coupling is increased (distance between coupling prism and resonator is reduced) light tends to exit the resonator sooner using the prism. This decreases Q_C as the losses incurred by the coupling increase. This separation also allows us to redefine the coupling regime in terms of Q-factor. *Under coupling* is where $Q_0 < Q_C$, *critical coupling* is where $2Q_T = Q_0 = Q_C$ and *Over coupling* is where $Q_0 > Q_C$.

Energy losses in a WGMR can occur from surface scattering, material absorption and radiative loss. We polish the surface of the resonator (see section 2.5) to minimise losses by surface scattering. The light lost from radiation is a result of the evanescent field that escapes the resonator. As this field decays exponentially, a sufficiently large major resonator radius compared to the wave-length of light ($R >> \lambda$) means the radiative losses are usually negligible when compared to other sources of loss for the resonator.

3.5.4 Free Spectral Range

When light is coupled into the resonator, the frequency of the light will determine how many wavelengths comprise one round trip of the resonator. The free spectral range (FSR) is a measure of the increase in resonance frequency between the coupled light and light that completes one round trip with an extra wavelength. This value is non constant when the number of wavelengths that comprise a single round trip is small. As the number of wavelengths in one round trip increases the increase in frequency becomes more constant. Due to the major radius R of the resonator relative to the wavelength of light coupled into it we can assume that the FSR is constant. FSR is given by the equation

$$\text{FSR} = \nu_{m+1} - \nu_m. \tag{3.10}$$

We can directly calculate the expected FSR for a resonator using

$$\text{FSR} = \frac{c}{\pi D_{\text{resonator}} n_{\text{eff}}}, \tag{3.11}$$

where $D_{\text{resonator}}$ is the diameter of the resonator in millimetres. There is an interesting phenomena that can occur known as mode anticrossings [12] where modes couple with each other. This is usually seen between modes of differing polarisation.

3.6 WGMR Characterisation Measurement Process

3.6.1 Coupling Contrast Measurement Process

The coupling contrast is obtained by normalising the voltage of the out-coupled light from the resonator at the detector.

3.6.2 Linewidth Measurement Process

We obtain the linewidth for a mode by fitting a Lorentzian to a mode of interest and extracting the FWHM value. As linewidth is a frequency value, this requires translating the x-axis into frequency instead of time. The conversion is done through the method described in section 4.3.2. It is recommended to have the Lorentzian fit done using a computer for accuracy and speed.

3.6.3 Q-Factor Measurement Process

We commonly calculate a range of Q-factors for a single mode by changing the coupling conditions. If we modify the distance between the coupling prism and the resonator we can change the coupling contrast and linewidth for that mode. Often we do this to find the maximum Q-factor value. We do this by changing the position of the coupling prism (by adjusting the voltage of the attocube that it is mounted upon) and saving the trace of the mode seen on the oscilloscope. We do this for several measurements, obtain the linewidth using the process above and substitute values into equation 3.8.

We can also obtain the intrinsic Q-factor Q_0 for a mode by changing the distance between the coupling prism and resonator in small, regular increments and obtaining the linewidth at each increment. This will often show exponential behaviour due to the exponential nature of the evanescent field. If we fit an exponential line to the linewidth values calculated. The y-intercept of this fit line should match the intrinsic Q-factor because it is equation 3.9 taken at the limit where the contribution from the coupling Q-factor Q_C is zero.

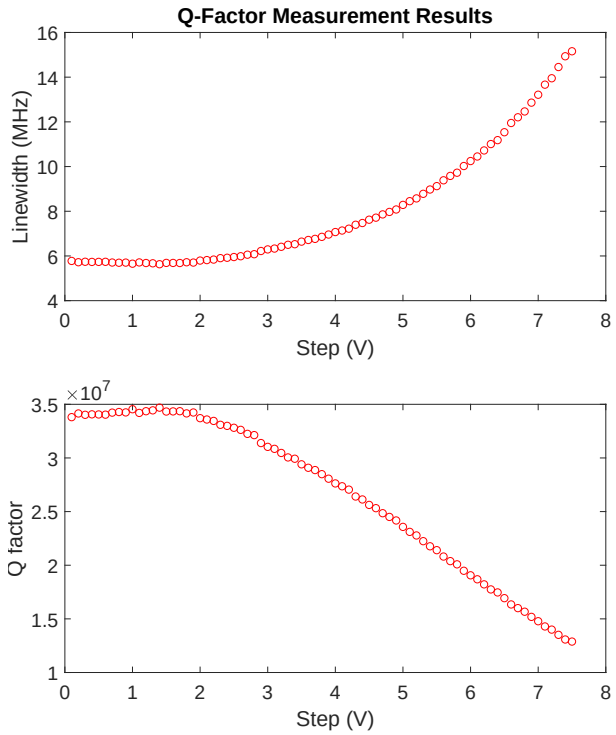

FIGURE 3.13: The coupling prism was moved incrementally by adjusting the voltage of a piezo. A trace of the mode was saved after each increment of movement and had a Lorentzian fitted. Using the fit, the Q-factor was extracted and plotted.

3.6.4 FSR Measurement Process

We ensure that light is coupled into the resonator and that modes can be seen on the oscilloscope. We observe one mode and use equation 3.11 to get an estimate of the FSR we would expect for the resonator. We then use an electro-optic modulator

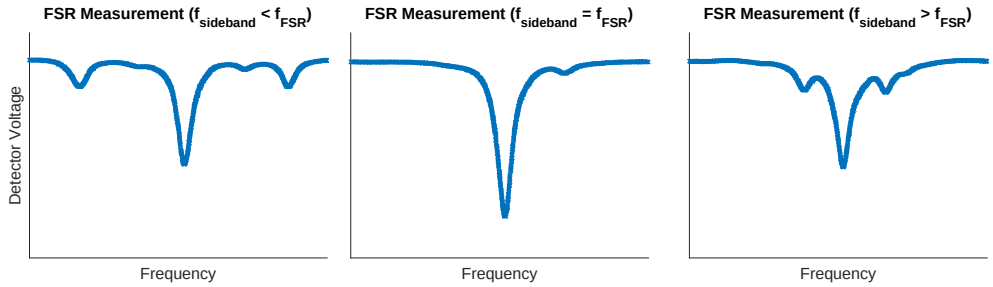

(A) Side-bands are modulated onto the signal below the FSR frequency, giving the trace side-bands that appear equidistant from the mode.

(B) Side-bands are modulated onto the signal at the FSR frequency. The side-bands coalesce with the mode giving the mode a greater coupling contrast.

(C) Side-bands are modulated onto the signal above the FSR frequency. The mode loses the increased coupling contrast and the side-bands reappear to either side.

FIGURE 3.14: Modulating side-bands onto the signal at various frequencies to find the FSR of a mode.

(EOM) to modulate side-bands onto the light with a side-band frequency near the calculated value. If the EOM frequency is close to the FSR, then the side-bands of the modes with one wavelength higher and lower will appear equidistant from the observed mode. If the side-band frequency is tuned closer to the EOM frequency then the position of the side-bands will move closer to the observed mode until they perfectly overlap the focussed mode. The modulated side-band frequency at this point is the FSR frequency. When $f_{sideband} = f_{FSR}$ the observed mode often appears to increase in depth making it obvious visually when this frequency is found.

Chapter 4

Experimental Setup

In this chapter we will discuss some of the assumptions made in Foreman et al. and how they are controlled for within the experiment in this thesis. This will include a break-down of figure 1.4 that was introduced in chapter 1. We will then take a more detailed look at the experimental setup with discussions on how a mode is selected and measured. We will then discuss some of the finer operational details of various experimental apparatuses used in this experiment. This chapter will conclude with a discussion of the software that we built and used to increase the efficiency and volume of data collection. We will use this as foundational discussion to explain why the development of such software was necessary within the scope of this experiment.

4.1 Experiment Objectives

Foreman et al. Theory

In Foreman et al. (2016) [5], the calculations made were using several conditions which we will now discuss. The calculations of Foreman et al. rely on a lithium niobate resonator that has 1550 nm light coupled into it. Lithium niobate is a birefringent material (review section 3.1.2) meaning that it has an ordinary refractive index of $n_o = 2.213$ and an extraordinary refractive index of $n_e = 2.138$. The geometry in the resonator is assumed to be of major radius $R = 2.1$ mm and minor radius $r = R/9$. The WGMR used is a z-cut resonator and the fundamental modes were assumed, meaning mode values of $p = 0$, $q = 1$. For the fundamental TE mode this led to the calculation of azimuthal mode number $m = 18152$ and the fundamental TM mode azimuthal number of $m = 18790$. These values were quoted as being calculated from the dispersion relation given in Breunig et al. (2013) [11]. The results of the frequency shifts on the resonance modes by the substrates are from the assumption that the substrates have a thickness so much larger than the 1550 nm wavelength light that they can be considered infinite in thickness. Finally it is assumed that the substrate is brought from infinity into touching contact with the resonator.

Frequency Shift Contribution Discussion

In figure 4.1 the legend indicates that there are 3 separate curves noticed on the plot: the total curve and two contributions that comprise the total curve ($\mathcal{N}_\nu^{(1)}$ and $\mathcal{N}_\nu^{(2)}$) These are defined integral terms that are taken from Foreman et al. (2016) [5]. While they are initially introduced as equations 49 and 50 in Foreman et al. (2016) [5], they rely on work done by Foreman et al. throughout Chapter 4 and accompanying work done in Appendix C (where the Bethe-Schwinger equation is derived) to reach the form used in figure 4.1 (equations 66 and 67 in Foreman et al. (2016) [5] for $\mathcal{N}_\nu^{(1)}$ and $\mathcal{N}_\nu^{(2)}$ respectively). It is these forms which I will be discussing in more detail below.

For any reader interested in their definition they can look to Chapter 4 and Appendix C in Foreman et al. for a greater theoretical discussion than what is presented here. $\mathcal{N}_\nu^{(1)}$ will be discussed in greater detail within the subsection 'Red Shift Phenomena' below and $\mathcal{N}_\nu^{(2)}$ will be discussed in greater detail within the subsection 'Blue Shift Phenomena' below.

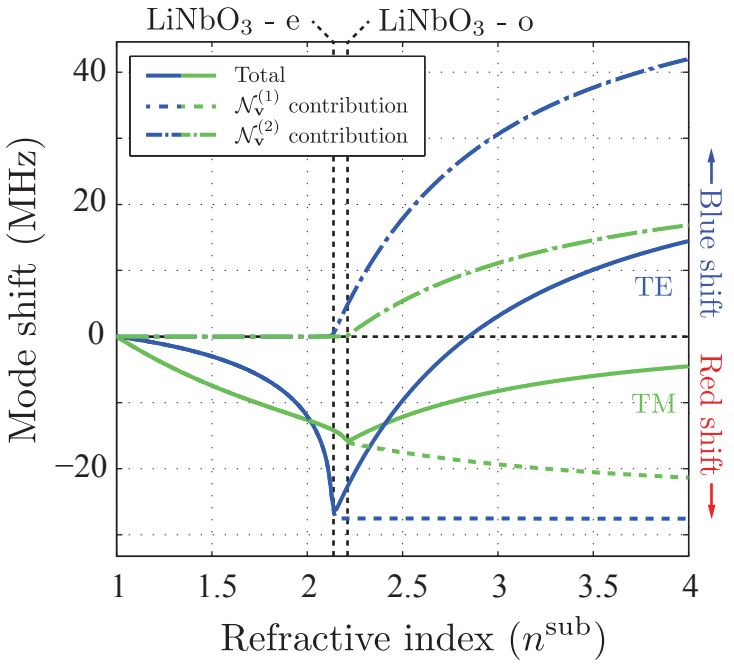

FIGURE 4.1: Figure 3a taken from Foreman et al. (2016) [5]. This figure has appeared earlier in the introduction to this thesis however it is repeated here for ease of access when discussing the results of this figure in greater detail.

Our Experiment

The assumptions covered above place some conditions on how we conducted this experiment. We used a lithium niobate resonator that was z-cut, so the same material and cut of resonator was used. The geometry of the resonator is different. The geometry of our resonator is such that the major radius $R = 12.5\,\mathrm{mm}$ and the minor radius $r = 5\,\mathrm{mm}$.

As the paper uses a continuous scale of refractive index, we cannot replicate this in an experimental setup. Instead we discretize the scale into a series of substrates with increasing refractive index. Thee substrates are similar sized windows that we mount on aluminium slides with wax so that we can attach them to an attocube for movement. The silicon substrate was much larger than the other windows so we used a diamond saw to cut the window in half. This was necessary as the silicon window was too big for the slide. The list of substrates can be found in table 4.1 below.

Substrate	Refractive Index	Image
Germanium	4.0 [13]	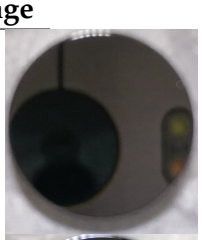
Silicon	3.48 [14]	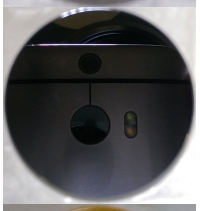
Zinc Selenide	2.45 [15]	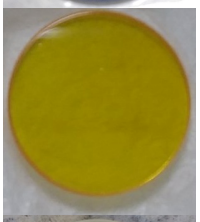
Zinc Sulfide	2.27 [16]	
Sapphire	1.75 [17]	
Optical Glass	1.5	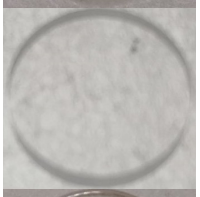
Calcium Fluoride	1.43 [18]	

TABLE 4.1: The substrates used in the experiment.

Red Shift Phenomena

The red shift is theorised to be the result of work done to generate a material polarisation in the resonator. This is represented by the term $\mathcal{N}_{\nu}^{(1)}$ in figure 4.1. The evanescent field around the resonator interacts with the substrate and the field remains evanescent at small substrate refractive indices ($n_{\text{resonator}} > n_{\text{substrate}}$). The difference between the refractive index of the substrate and resonator determines

the magnitude of the shift. The magnitude of the red shift increases as the difference between the refractive index of the substrate and resonator decreases. When the refractive index of the substrate approaches the limit $n_{\text{resonator}} \approx n_{\text{substrate}}$, the magnitude of the red shift is greatest and the maximum red shift occurs.

The small difference in the refractive index at which the maximum red shift occurs between TE and TM polarised light is due to the birefringence of lithium niobate, and therefore the maximum red shift occurs at $n_{\text{e}} \approx n_{\text{substrate}}$ for TE and at $n_{\text{o}} \approx n_{\text{substrate}}$ for TM.

If the refractive index of the substrate is increased past this point $n_{\text{resonator}} < n_{\text{substrate}}$, the magnitude of the red shift decreases. This is in contrast to the magnitude of the contribution $\mathcal{N}_v^{(1)}$ which remains constant for TE waves and nearly constant for TM waves. This a consequence of the transmitted wave from the resonator to the substrate containing propagating as well as evanescent components (noted by the contribution $\mathcal{N}_v^{(2)}$ increasing from zero). This can cause the resonator resonance frequency to begin to blue shift as radiative losses are increased into the far field (discussed more below).

Blue Shift Phenomena

When both the effective refractive index of the resonant mode and the refractive index of the substrate match, the evanescent field that leaks into the substrate becomes a travelling wave. These contributions are signified by the term $\mathcal{N}_v^{(2)}$. They grow as the substrates index increases. At some point these contributions cancel the polarisation components $\mathcal{N}_v^{(1)}$ entirely and the substrate does not induce any shift (there will be however still a mode broadening due to part of the light propagating into the far field).

Increasing the refractive index of the substrate further past this point causes the effect of the blue shift to become stronger than the effect of the red shift ($\mathcal{N}_v^{(2)} > \mathcal{N}_v^{(1)}$).

The resulting blue shift can be understood well in the limit of very large refractive index of the substrate. In this case no light can penetrate into the substrate and the substrate acts as a perfect mirror. If the light can not enter the substrate, the electro-magnetic field needs to have a node at the surface which will push the mode contributions of the whispering gallery mode deeper into the WGM, thereby causing a blue shift.

Mode Broadening

In the coupling regime where $n_{\text{substrate}} < n_{\text{resonator}}$, the parts of the field that leak from the resonator into the substrate contain evanescent components but no propagating components. This means that no light is coupled out into the substrate so no mode broadening is observed.

At the point where $n_{\text{resonator}} < n_{\text{substrate}}$, the parts of the field that leak from the resonator into the substrate contain propagating components as well as evanescent components. Some of the energy is carried in the propagating components that is not re-introduced to the resonator. This energy is carried into the far field and is thereby lost to the resonator. This loss mechanism causes the linewidth of the resonance to increase. As there is less energy leaked into the evanescent field by TM modes, the expected mode broadening for TM modes is thus expected to be less than TE. Again we can observe the effects of the birefringence of lithium niobate

as the point where mode broadening begins to occur coincides with the refractive index of lithium niobate experienced by the different polarisations of light. For TE polarised mode broadening occurs when $n_{\text{substrate}} > n_{\text{e}}$ and for TM polarised light mode broadening only occurs when $n_{\text{substrate}} > n_{\text{o}}$.

For much larger refractive indexes we can see a drop in the mode broadening. This can again be understood well in the limit for very large refractive index of the substrate. In this limit the substrate acts as a perfect reflector and therefore no light is lost.

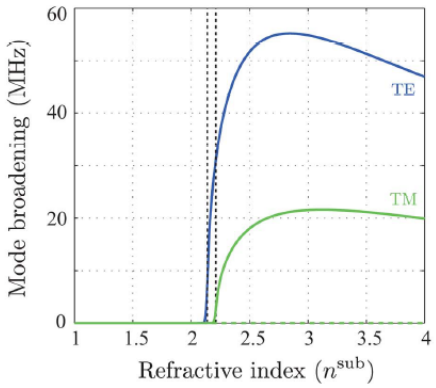

FIGURE 4.2: Figure 3a taken from Foreman et al. (2016) [5]. This figure shows the mode broadening TE and TM polarised light. Of interest is the shape of the curve for both TE and TM where the curve shows a local maximum mode broadening.

4.2 Setup

The setup was designed to ensure we had a high degree of mechanical stability in coupling light into the resonator. It was also designed such that the tested substrate could be brought into close proximity so monitoring the space around the resonator was important.

The central block features a main hole that houses the brass rod with resonator mounted. The location of the hole that houses the brass rod is aligned with a screw hole in the optical table underneath. This gives us a good reference point to align the correct angle for the laser when coupling light into the resonator and also provides a high degree of stability on the optical table. The major disadvantage that comes with the lack of rotational freedom is that any change in angle of incident light needs to be performed by re-orienting the translation stage that coupled the light into free-space for the setup. This trade-off is acceptable as the angles calculated to couple to the fundamental TE and TM modes are based on the resonator and coupling prism and will therefore remain constant throughout the experiment. The central block also features the ability to mount an attocube near the resonator. By having the attocube on the same block as the resonator it increases the mechanical stability of the setup. On top of the attocube is a single arm that has the coupling prism fixed to it. The attocube allows the distance between the prism and the resonator to be controlled with a high degree of precision.

In our setup we have a z-cut lithium niobate resonator and the coupling prism is an equilateral triangle made of diamond. This means that performing the calculations in 3.3.3 yields a coupling angle of 21.3° for TE modes and 10.7° for TM modes.

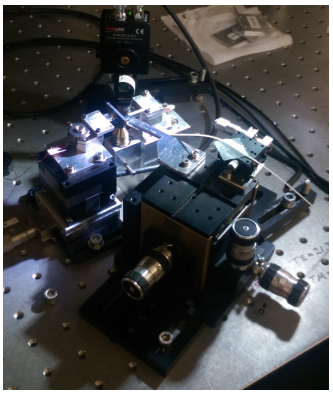

(A) Photograph of the experimental setup in an overview.

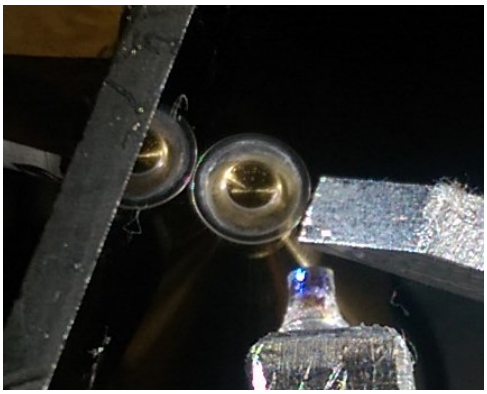

(B) Photograph of the resonator in contact with the silicon substrate window. A reflection of the resonator can be seen in the window and the GRIN lens and coupling prism can also be seen nearby.

FIGURE 4.3: The setup used for the experiment.

The detector is a Thor Labs InGaAs Amplified Detector which we use to collect the out-coupled light from the resonator. It has a variable gain in increments of 10dB. The gain can be turned up to offset low laser power but it should not be turned up too much or the detector can become sensitive enough to pick up the beat frequency of the lights in the lab.

4.3 Automation

Because our experiment is to test for a shift in the frequency of a mode when a substrate is in close proximity of the WGMR, we need a rigorous repeatable system to collect data. If we collected this data manually we would need to change the position of the substrate and save the frequency trace measured by the detector. This process would need to be repeated enough times to build up a range of substrate positions and analysis of the data would be needed to highlight any observable shift in the frequency. This would be very slow and likely very inaccurate. Ideally this process would be done quickly to avoid large environmental changes in pressure or temperature that might affect the results.

To most efficiently collect data we automate the procedure. There are two parts to the automation of this experiment. Part 1 is the automation of data collection, this is performed through a python script. Part 2 is the manipulation and analysis of the data, this is performed through a MATLAB script. Both parts are discussed in detail in this section.

4.3.1 Computer Communication Discussion

As we are using a computer this introduces an extra layer of complexity to the experimental setup. It is worth taking a moment to discuss how a computer is able to communicate with the apparatus used in the experiment. In this experiment we have two methods of computer communication. One uses an external interface to facilitate the communication. In this experiment this external interface is a breakout box. The other method used in this experiment is to wire the apparatus directly into the laboratory network with its own static IP address. Both methods are discussed in more detail below.

Breakout Boxes

In order to facilitate communication between a computer and a device like the nanocube or the attocube, we use a breakout box (see figure 4.4). A breakout box serves as an interface between BNC cable inputs from the devices in the lab and the computer. Information is passed to the computer through its PCI slot. We use two different breakout boxes in the experiment. One breakout box facilitates communication between a lab computer and the nanocube. Another breakout box facilitates communication from the EOM to a second lab computer. We need two different lab computers as only one has a PCI slot which is a necessity for the breakout box to talk to the nanocube. The other computer manages its breakout box through a USB port but this breakout box lacks the required BNC slots to connect to the nanocube. The network access route also removes the potential for crosstalk to occur between devices. Crosstalk can be noticed in something like a breakout box where the signals are transmitted through BNC cables. A consequence is that the signal transmission through one cable can lead to some signal getting "leaked" into a nearby cable or channel. This has been noticed when BNC cables are plugged into ports located next to each other on the breakout box. It is often mitigated by plugging a dedicated resistor end into the unused ports of the breakout box nearby to the port with the BNC cable plugged in.

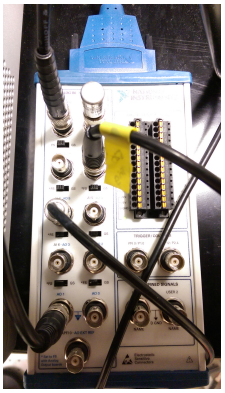

FIGURE 4.4: Photograph of the breakout box controlling the nanocube.

Network Access

In the experiment we also use a digital oscilloscope and an attocube controller. Both of these devices are wired into the network of the lab. This makes it easy to connect to them over the Local Area Network (LAN) as they have their own IP address and port. Giving them network access provides a significant speed advantage in reading data from each device as it bypasses the breakout box which can get congested with each device relying on a bus to transfer information to the computer. Accessing the attocube controller through the network also extends its functionality as it has an onboard console that can receive commands through the network. This makes remote operation of the attocube controller only possible when the attocube controller is accessed through its network port.

4.3.2 Python

A former PhD student designed the basic script that we used as the python automation script in this experiment. For the script to automate the data in a useful and efficient way we designed it to do several things. The script copies the trace from the detector on the oscilloscope and reproduces it on the computer, this allows us to save the traces as .dat files for MATLAB to import and analyse. We decided not to make the program automatically update for reasons outlined below so it refreshes on a command or action performed from within the program instead. The script also has the ability to talk to the EOM in the lab. This has the advantage of being able to perform the majority of the tasks required in the pre-sweep calibration process (see section 5.1) from a single lab computer. We extended the functionality of the script to also be able to communicate directly with the attocube controller. This removes the need to make small adjustments to the attocube from the controller, and instead can also be performed from the lab computer. Due to the ease of communication to other equipment in the setup from within this python script, we created methods that would increment the position of a piezo. We can set this piezo to be the one responsible for the position of the substrate to generate a .dat file every time the substrate moves past a set threshold in displacement. It was important to automate this process for two reasons, it is much faster to take data when the process is automated, and it can be timed such that the time interval between measurements is kept constant. Irregular time intervals could skew the data and give false results. As we could control the step sizes that the piezo took we can generate sets of data of many different resolutions. This is a useful feature if we want to investigate a particular displacement from the resonator in higher resolution.

Frequency Axis Calibration

The x-axis of the python oscilloscope must be changed into frequency. This requires the use of side-bands of a known frequency to be modulated onto the light by an EOM [19], and using the position of the side-bands to form a frequency scale for the python script. This process is simple to carry out from within the script and is vital to do before an experiment sweeps are conducted.

1. We focus on a mode on the python oscilloscope that looks like it would have a high Q-factor and a low linewidth
2. We turn on the EOM with a designated frequency. This should be chosen reasonably as from Foreman et al. we expect frequency shifts of up to 40 MHz. We can use the scan control amplitude dial on the frequency sweep of the laser to increase or decrease the distance between the mode and the side-bands without adjusting the frequency of the EOM.
3. We type the upper and lower bounds of the mode and the side-bands into the appropriate boxes in the python script.
4. We specify the frequency of the side-bands if this is not already entered in the script window.
5. We click calibrate. This initialises a method that finds the position of the side-bands relative to the mode and sets the difference between them equal to the side-band frequency. It then forms a new scale based on the relationship between the number of data points an the frequency to translate the x-axis from

sample number into frequency. It will also zero the axis about the mode. This makes any frequency measurements relative to the calibrated mode position.

6. We then turn off the EOM and refresh the python oscilloscope to return the frequency trace to be of just the desired mode.

This completes the calibration process and an experimental sweep is now ready to be conducted. The scan control amplitude dial on the frequency sweep of the laser cannot be tampered with or the calibration process must be repeated. The DC offset dial can be used as this only applies an offset and doesn't adjust the scale of the frequency between the side-bands and the mode. The equations followed by the calibration method to turn sample number into frequency are shown below.

$$\mathrm{Hz} = \frac{2 \cdot f_{\mathrm{sideband}}}{d_{\mathrm{sideband}}}, \tag{4.1}$$

where $f_{sideband}$ is the side-band modulation frequency (often chosen to be an integer multiple of 10 MHz) and d_{sideband} is the number of data points that reside between the centre of the left side-band and the centre of the right side-band, calculated as

$$d_{\mathrm{sideband}} = n_{\mathrm{Right}} - n_{\mathrm{Left}}. \tag{4.2}$$

As there is a finite amount of data taken in from the oscilloscope by the python script, we can artificially boost the resolution by changing the scan control amplitude dial with an appropriate EOM frequency to ensure the distance between the mode and the side-bands is as large as possible while remaining visible on the oscilloscope. Doing this means there are more samples available for each unit of frequency, giving changes in frequency a higher resolution.

Program Limitations

One might assume that the easiest way to see the results of the experiment in real time is to make a python script that also has a constantly updating GUI. This would give it the advantage that any change in the frequency is immediately noticed on the screen. While this is a major advantage, our attempts at achieving this failed when we discovered the presence of a "race condition" within the program.

A race condition can occur in software when an application relies on a particular sequence of processes or threads to operate correctly. When we made the python script that had the GUI, we decided that the best method was to both update the GUI and poll for new data to come in through the PCI card. We created separate threads, one that was only responsible for moving the substrate on command from within the program and one that was only responsible for updating the GUI by pulling in information from the detector. We thought this approach worked but found that the movement of the substrate was faster than the GUI was able to update. This lead to the race condition as the GUI was "blocked" from updating while the substrate moved, yet as a result the computer didn't have enough time to switch between updating the GUI and moving the substrate sufficiently. We found that instead the program would assume that the substrate had moved even when it had not. This lead to inaccurate data.

We discovered this by getting the program to pretend that the position of the substrate was the voltage at the detector, allowing us to see what the true output of

the program was. We expected this test to show lines at 1 V increments, corresponding to the increment in position of the substrate (figure 4.6a). The results of this test can be seen in figure 4.6b. Due to the inaccuracies between the expected results and the actual results we decided to manually implement a sleep of the computer to overcome the race condition. While this did increase the accuracy of the program and produced results that we expected, the time taken to run each sweep increased significantly as there was a sleep period of 500 ms. The idea of using a constantly updating GUI was eventually abandoned and replaced with the python program described above.

4.3.3 MATLAB

Alfredo Rueda provided the initial design for the MATLAB script that would process the .dat files generated from the python script. This script takes a user-specified number of data files and applies a Lorentzian fit to the mode seen in each trace. It then compiles the results of all of the Lorentzian fits applied and generates a plot for the Q-factor, linewidth and frequency shift. The frequency shift that the MATLAB script produces is relative to the first data set it analysed, and not the frequency axis associated with the .dat file it received from the python script. This is done to remove any frequency offset that might be carried over from the python script. This script is useful for both the experiment and finding the critical coupling distance between the coupling prism and the resonator. We will use this script to set the coupling prism distance to match where the highest Q-factor is obtained.

4.4 Nanocube Discussion

The accuracy in measuring the substrate position is crucial to determining how much the substrate perturbs the evanescent field. To maximise the accuracy of these measurements we need a very precise system to control the position of the substrate. Piezos are popular for taking positional measurements at the sub-micron level. We are using a Physics Instruments 3 Dimensional Nanocube Controller and P-611.3 Nanocube for this task. This apparatus is capable of translating by up to 100 µm in each dimension. There is a stack of piezos located internally that can control movement in each dimension of the nanocube. The piezos are designed to expand and contract in response to a voltage being passed through them, with the magnitude of the voltage controlling the amount of expansion and therefore the amount of movement. As this is a physical change in the crystal to change the position, there can be a hysteresis problem, where the amounts of expansion and contraction are not always equal. There are servos present in the nanocube to reduce the effects of hysteresis as well as dampen fluctuations in the voltage. This keeps the position stable to a tenth of a micron. Initial testing of the nanocube controller deemed the y-axis the only appropriate axis for the direction of the substrate movement. The z-axis was unusable as it moves the substrate perpendicular to the table instead of in the experimental plane. The x-axis was not able to remain in a stable position regardless of the servos being active, the output would fluctuate making it unusable when precision is so critical.

Each axis of the nanocube controller has two BNC ports associated with it. One is an input to modify the voltage of the axis within the nanocube and the other is an output of the voltage for connecting to an external measurement device. We utilise both ports when we automate the data collection process (discussed below in

section 4.3). We also tested the calibration of the nanocube to ensure that the values it displayed were accurate. This process is described in section 4.4.1 below.

The entire nanocube is mounted on top of a one dimensional stage translator. This translator is useful in making coarse position adjustments for the substrate and nanocube. This allows us to move the nanocube rapidly away from the WGMR when we want to change the substrate being tested. This also allows us to move the substrate near to the WGMR by eye using the coarse adjustment knob on the translator. It would be difficult to use the nanocube to move the substrate directly into contact with the resonator. There is no feedback mechanism to tell us when the movement of an axis is impaired. We mitigate this difficulty by mounting an attocube to the top of the nanocube (see section 4.5 below). This has the audible feedback mechanism for movement and so is easier to use to close the remaining distance in placing the substrate into contact with the resonator.

4.4.1 Nanocube Calibration

Accuracy was ensured between the position of the nanocube and the digital readout of the nanocube controller by building a Michelson Interferometer. The interferometer was built during a summer studentship. The movement of the nanocube was matched with the change in voltage read by the detector (see figure 4.8). We used a sine fit to determine the relationship between the position and voltage because a displacement of $\lambda/2$ of the mirror mounted on the nanocube causes a change in the wavelength of the beam at the detector by λ. We can solve this relationship to form an equation for voltage as a function of distance.

The results of this relationship were used to check if the readout of the position from the nanocube controller were consistent with the voltage we expected from calculations. We found that the relationship is approximately 1 V to 10 µm. This is consistent with the display of the nanocube controller. While the input of the nanocube controller accepts volts, it automatically converts voltage to position, resulting in any input being converted into an output of position. This simplifies the calculations needed to make for how the nanocube behaves. When feeding an input of voltage to the nanocube, it will automatically step the voltage up by a factor of 10. This means that we have an effective range of 0 V-10 V but the nanocube will display 10 times the voltage it receives as input. This voltage range corresponds to a positional change of 0 µm-100 µm. This is mirrored in the limits of the nanocube where it has a voltage input ceiling of 10 V.

4.5 Attocube Discussion

Attocube is a company that specialises in nano-positioning systems. When the term attocube is referenced in this thesis it is referring to the nano-positioning unit made by Attocube. We used ANPx101 linear horizontal stepper positioners in this experiment. This is done to distinguish it from the nanocube, as both are piezo systems used in this experiment. To operate an attocube it is plugged into a control module and there can be several control modules operating from a single control system, with each control module responsible for a single attocube positioner. In this experiment we used two ANM300 control modules and a single ANC300 control system. The piezo actuator inside an attocube is a piezo-ceramic made from lead zirconite titanate. These can be supplied with a voltage of up to 150 V which is enough for

most applications. The attocubes have a travel range of 50 mm and can perform movements at speeds of up to several mm/s.

An attocube is useful as a positioning solution in the experimental setup due to the piezo actuator within it that makes sub-micron movements possible. The mechanism for the attocube movement is detailed below. We use two attocubes in the setup. We use one as the method of moving the coupling prism as seen in section 3.3.2. We also use an attocube to control the position of the substrate in conjunction with the nanocube. Using the attocube to move something into contact with the resonator is preferred over a method such as the nanocube due to the feedback mechanism that makes it clear when the movement of the attocube is impeded. The feedback mechanism and how it's utilised is explained below. The attocube controller is also capable of receiving commands through an on-board console that can be accessed via logging into it directly. This can only be done if the attocube controller is connected on a network.

Attocube Movement Mechanisms

The attocubes use a "slip-stick" mechanism to move. This allows the attocube to make very small movements with high precision. The typical minimum step size for attocubes is around 50 nm when at room temperature. As this step size is smaller than the wavelength of light used in this experiment it makes attocubes invaluable at moving substrates to specific parts of the evanescent field. There are three steps that the attocube goes through to perform one displacement step:

1. Before the step: When there is no voltage applied to the piezo, the piezoceramic clamps the internal driving element. This clamping action and the friction of the coating on each side of the clamped interface prevents the position of the slide on the attocube from changing.

2. The "stick" phase: This involves applying a saw-tooth pulse of voltage to the attocube. During the ramp part of the saw-tooth wave the piezo expands, causing the slide to move the displacement corresponding to the voltage supplied.

3. The "slip" phase: During the steep drop portion of the saw-tooth wave, the piezo contracts rapidly. This contraction occurs over a short space of time, giving the piezo a rapid acceleration. The inertia of the slide on top of the piezo overcomes the friction force from the clamping, making it near stationary while the piezo "resets". This can be thought of having an effect similar to quickly pulling a table-cloth from under dinnerware if the dinnerware was the attocube slide and the tablecloth was the piezo.

With the piezo "reset" the displacement step is now complete and voltage is no longer supplied to the attocube. The lack of voltage triggers the clamping mechanism in step 1 again, preventing the position of the attocube slide from changing once more.

One can also use an offset voltage to expand or contract the piezo in an attocube. Doing so uses a mechanism different to the stepping system so the range of movement is reduced. This method is more useful for high resolution movements over a smaller range. The attocubes have a stock limit of 130 V which corresponds to a range of approximately 650 µm. This offset voltage can be controlled through the attocube controller via the front panel or remote connection. As the movement of the attocube is not the slip-stick method described above, it will not produce audio feedback as it moves.

Attocube Audible Feedback Mechanism

This feedback mechanism is only possible with an Attocube control module that has an output frequency range. This is available on control modules like the ANM300 used in this experiment. The ANM300 has an output frequency range of 0 Hz to 10 kHz which can be heard when the attocube is moved, so it can be set to a frequency that one can hear clearly. This frequency will remain constant while the attocube performs its movement however if the movement of the attocube is impeded the frequency output will change. This makes it obvious when there is something impeding the movement of the attocube. We can abuse this indication to purposefully wait for a frequency change while moving an attocube, such as when we want the coupling prism of a substrate to contact a WGMR. When the frequency of the attocube controller changes we can use that to indicate that whatever is on the attocube slide (such as the coupling prism) has impacted the resonator.

4.6 Attocube-Nanocube Scale Calibration

While the nanocube has a digital readout that can tell us the relative distance from the resonator, the attocube does not have such a scale. One way to calibrate the scale is to follow the method presented in [7] and fit the exponential decay of coupling linewidth (refer to equations 2 and 7-9 in [7]). This gives a calibration scale of 0.1 V $\approx$ 5 nm.

4.7 Frequency Shift Direction

While we can use the data to see *if* there is a shift in the frequency of a resonant mode, there is no way to tell from the data alone if the shift is in the correct direction or not. To determine the direction of any frequency shift we find, we use the wavelength meter. First we follow the same steps as above in section to couple light into the resonator and adjust it such that the coupling contrast is maximised, the mode line width is minimised and the coupling prism is in a critical coupling spot. Next we identify a suitable mode (high contrast and narrow line width) to track. We then use the DC offset knob on the laser controller to manually change the position of this mode on the oscilloscope screen. We determined that turning the knob clockwise resulted in a shift of the mode to the right. We then attenuated the signal to a very low amplitude as it is easy to overload the wavelength meter. We then plug the laser fiber into the wavelength meter instead of the experiment and measure the wavelength. We note this value and then turn the DC offset knob clockwise again. The result is that a clockwise turn of the DC offset knob reduces the wavelength. From the basic wave equation

$$c = f \cdot \lambda, \tag{4.3}$$

we know that a reduction in wavelength must be compensated by an increase in frequency. Because the DC offset is applied equally, there is the same frequency distribution on the oscilloscope screen. The frequency of the mode has not changed because we only adjusted the offset and not the physical position of anything that would change it. This means the area to the left of the mode must have higher frequency values to ensure equation remains satisfied. Therefore when the DC offset

knob is turned clockwise, we are seeing a *decrease* in frequency. This is vital information because without it we would not be able to conclude which direction the frequency shift is in.

4.8 Substrate Mounting Orientation

Due to the spherical symmetry of the resonator, it doesn't matter where the substrates make contact with the resonator. This means it does not matter at what angle the substrates are mounted in the x-y plane. It does matter at what angle the substrates are mounted in the y-z plane however. Because we are using wax to mount the substrates, it can be difficult to gauge the angle in the y-z plane. When the substrate is brought into proximity with the resonator, we can use the attocube frequency feedback to ensure that the substrate is touching the resonator, but we cannot know if the interaction surface between the resonator and the substrate is perpendicular. Ideally the substrates and the resonator would be mounted in the y-z plane at 0° (see figure 4.11a). As these angles are only controlled by eye during the substrate mounting process, there can be a few degrees of elevation present. We look at the substrates under the microscope after they are mounted, and if there is anything more than a few degrees of elevation the substrate is removed and the mounting process restarted. Despite there only being a few degrees of elevation, it is useful to know what effect this can have on our results. Using trigonometry, we can derive a relationship between the angle and the distance for the resonator-substrate interaction. We start with the right angled triangle with sides r, $r + \Delta y$ and the substrate edge (see figure).

$$\cos\alpha = \frac{\text{Adjacent Side}}{\text{Hypotenuse}}, \tag{4.4}$$

$$\cos\alpha = \frac{r}{\Delta y + r}, \tag{4.5}$$

$$\Delta y = \frac{r}{\cos\alpha} - r. \tag{4.6}$$

Where Δy is the distance between the perpendicular surface of the resonator and the substrate, r is the minor radius of the resonator and α is the angle of elevation to the touching edge of the substrate. Δy is chosen as the displacement amount to keep consistent with the direction of translation for the nanocube axis. The optimum and non-optimum cases are demonstrated in figures 4.11a and 4.11b.

To investigate what this means for the distance that we measure, we know that the minor radius of the resonator is 0.5 mm and used this to generate a range of angles between to determine how large the resulting displacement would be. The results can be seen in figure 4.12. What can be seen is that even for small angles there can be a significant displacement relative to the distance the substrate moves. We see that an angle of elevation of 10° results in a displacement of 8 µm and an angle of elevation of 5° results in a displacement of 2 µm.

As the substrates were all of similar sizes we are able to mitigate fluctuations in the degree of elevation between substrates. This was due to the identical way each substrate was mounted. The substrate was placed on a flat surface and an aluminium slide with hot parafin wax was pressed into each one to adhere them together. This was followed by mounting the slide with a substrate in a table vice. Due to the sloped edges on each side of the slide, this meant it could be mounted flat

in the vice. As the wax was still hot briefly after the mounting process, a toothpick was used like a rolling pin to level the amount of wax between the substrate and the slide. The toothpick was pressed down across the centre of the substrate-slide join while the wax cooled down, further flattening the substrate. As this was repeated for each substrate and that the substrates and slides were near identical sizes, this lead to a uniform and flat set of mounted substrates.

4.9 Environment Control

A large potential source of error is in the ambient environment around the setup. If we do not take any measures to isolate the experiment from a changing environment, the thermal fluctuations can confound the frequency shift measured during the experiment (see figure 4.13).

To prevent this, we use a simple cardboard box as an insulator from air-currents that may be circulating around the setup during the experiment. We place the box over the setup and cut any material that may block an element of the experiment such as the light beam to the detector. By placing the box over the setup it is hoped that the optical table will serve as a thermal stabiliser, being large and metallic allows it to operate as an effective heat-sink. The box also helps mitigate air currents from circulating around the resonator.

To further increase the temperature stability of the setup, we built a temperature stabiliser to fit around the resonator (see figure 4.15). This temperature stabiliser uses a Peltier device to heat the setup to a specified temperature and the accompanying thermistor serves as a feedback mechanism to ensure the temperature is at the correct level. To control the Peltier device we use a Thor Labs TED200C temperature controller. This allows us to set the temperature that we want and operates the Peltier device until the thermistor reads the same temperature. It can then use the Peltier and thermistor to maintain a temperature specified to the accuracy of 0.002°C. We clamp a block of copper around the brass rod, and use thermally conductive epoxy to fix the Peltier to one side of the copper. We then drill a small hole in the copper on the opposite side to mount the thermistor in. The block of copper serves as an excellent heat conductor, so the heat from the Peltier can be easily transferred through the copper and into the brass. The Peltier device uses the Peltier effect, where a current flowing through a boundary between two different conductors can add or remove heat from the boundary depending on the direction of current flow. This is known as thermo-electric cooling, and does not involving moving parts. This means we can use this for of temperature stability without introducing any extra air-flows around the setup. A heat sink is fixed to one side of the Peltier to build a thermal gradient between the both sides of the Peltier. This allows it to dump heat from the heat-sink into the copper when we need the brass rod heated, and dump heat from the copper into the heat-sink when we want the brass rod cooled.

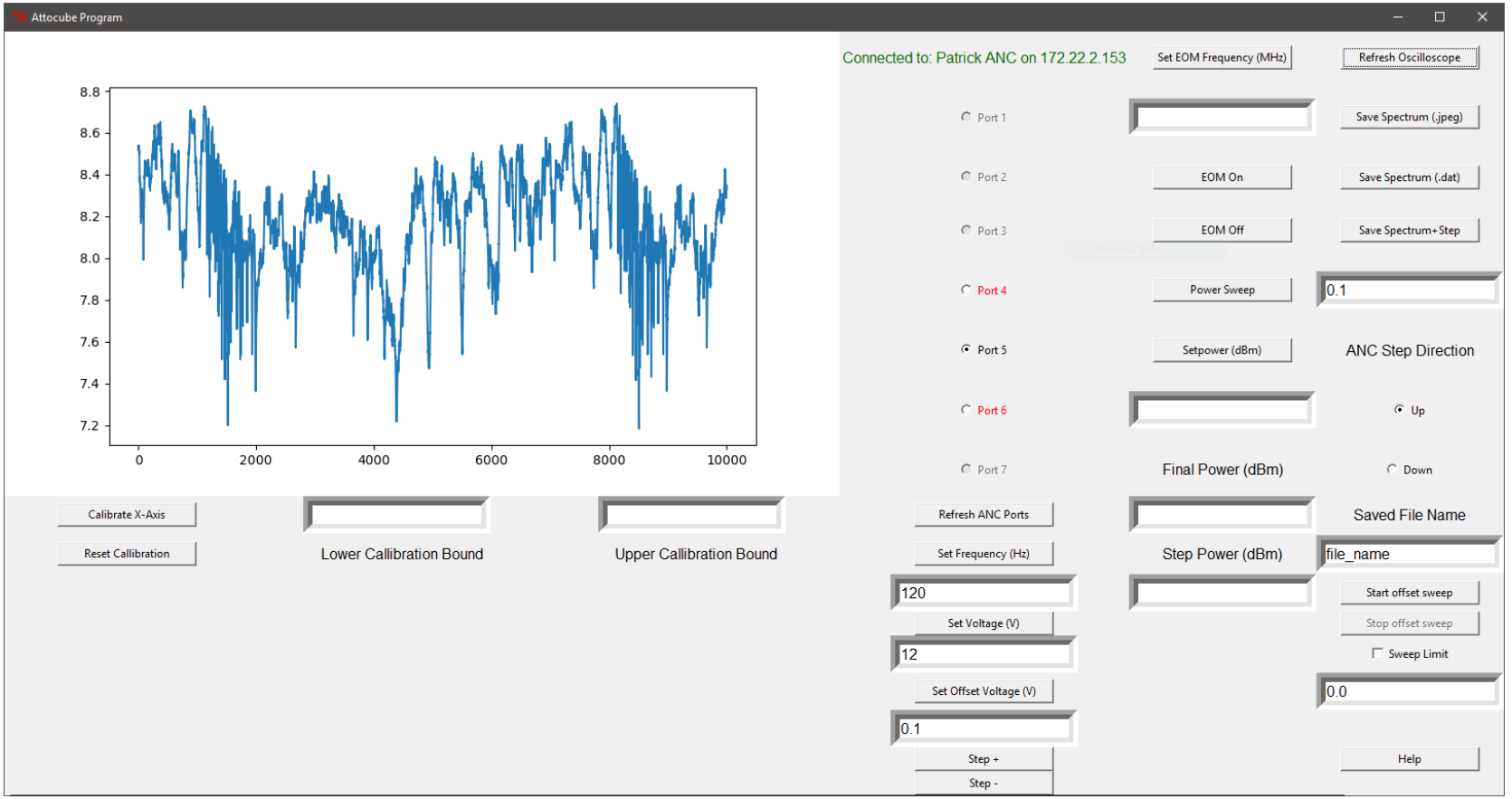

FIGURE 4.5: Screenshot of the python script running most of the data collection automation. The modes displayed are taken directly from an oscilloscope via network connection. There are options for controlling attocubes via network access to attocube controller remote terminals seen in the column to the right of the trace plots. There are also options for controlling the EOM directly in the column to the right of the attocube controls, allowing for frequency calibration of the trace plots x-axis to take place within a single script. The rightmost column contains options related to data collection, with saving options and automation methods available.

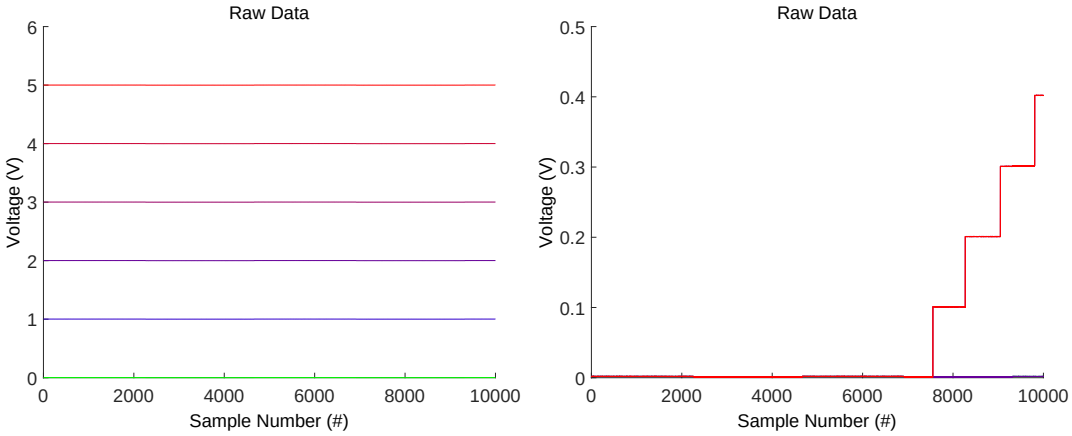

(A) The expected results for the program incrementing a voltage output. These results were only obtained after implementing a 500 ms sleep after each increment in order to overcome the race condition.

(B) The results of the race condition test. The program has not been able to increment the output voltage and instead can only increase the voltage by a small amount when it is most of the way through a sweep. The voltage step seen in the figure corresponds to a steady output of 5 V in the absence of the race condition.

FIGURE 4.6: We tested for a race condition by getting the program to increase its voltage output from 0 V to 5 V in increments of 1 V.

FIGURE 4.7: Photograph of the nanocube controller used. The green-lights indicate that the internal servo-motors are stabilising the position across each axis and the y-axis is showing that the nanocube is currently 40 µm in the direction of the y-axis.

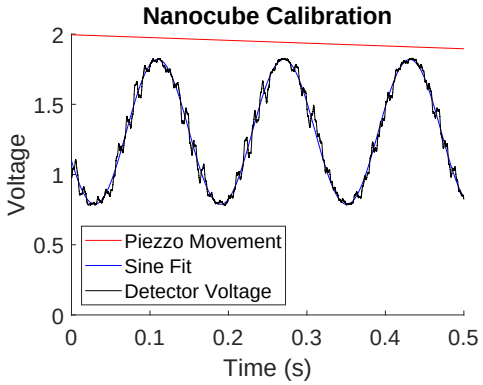

FIGURE 4.8: Results of the Michelson interferometer built to calibrate the nanocube.

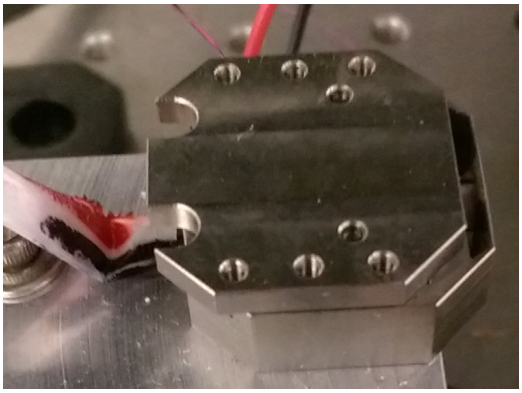

FIGURE 4.9: Photograph of an attocube. There are screw holes along both sides of its top for mounting and is controlled via the single pin wires seen trailing to the left of the attocube.

(A) Photograph of the attocube controller with individual axis modules plugged into the front.

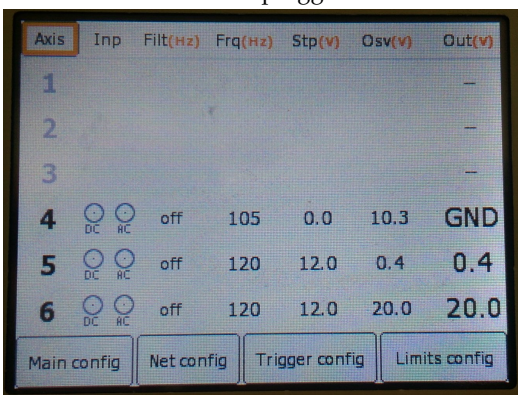

(B) Close up of the display of the ANC300 attocube controller. The values and status for each axis are clearly visible.

FIGURE 4.10: The ANC300 attocube controller used in the experiment.

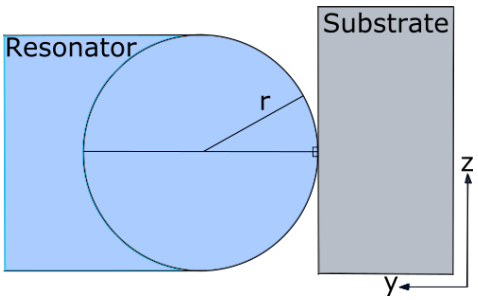

(A) Diagram of substrate mounted without angle resulting in no displacement.

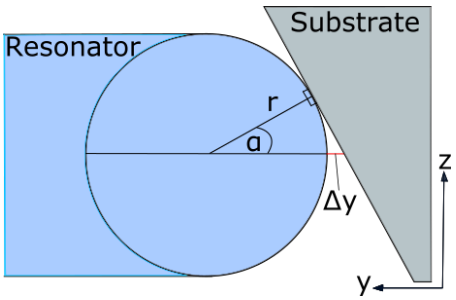

(B) Diagram of substrate mounted at an angle a resulting in displacement.

FIGURE 4.11: Diagrams of how the orientation of the substrate can impact the resonator-substrate distance.

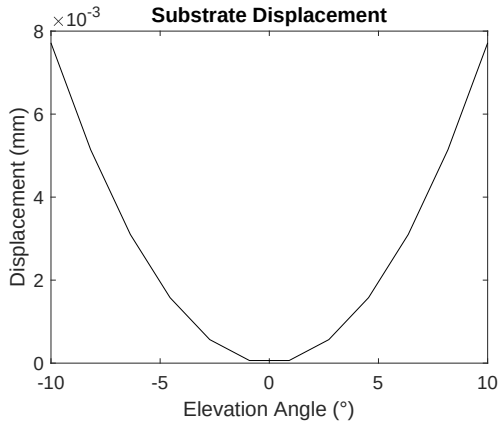

FIGURE 4.12: Impact of the mounting angle of the substrate on the displacement.

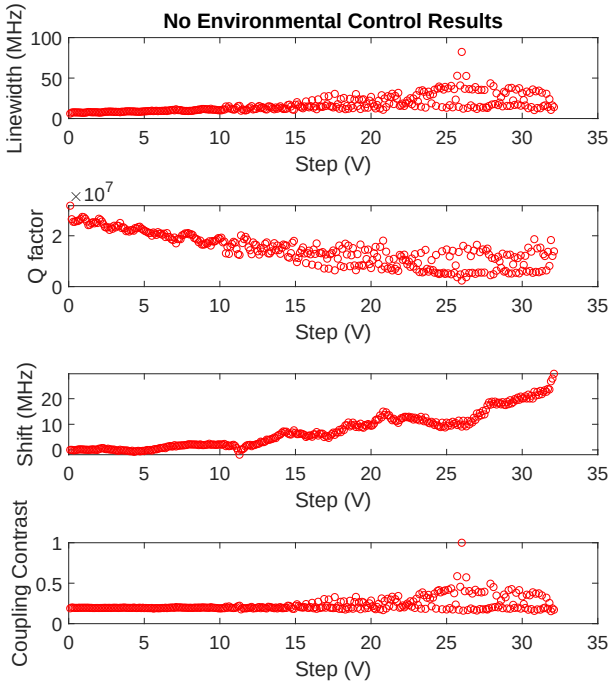

FIGURE 4.13: Results of running a practice sweep with no environmental control. No substrate was mounted so there was no change in substrate-resonator distance. As typical sweeps with substrates run over 30 V this test was left to run for an equivalent period of time.

FIGURE 4.14: Photograph of environmental control box when placed over the setup.

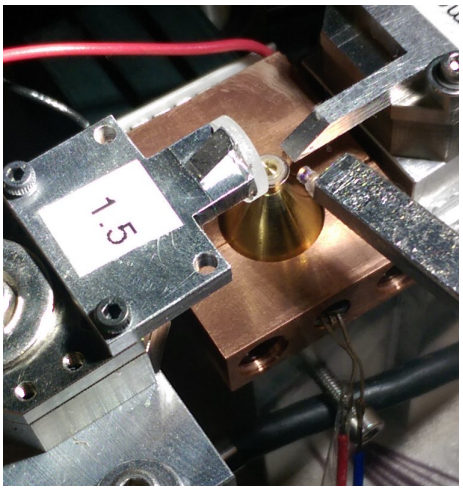

FIGURE 4.15: An image of the temperature stabiliser we built to further mitigate thermal fluctuations around the experiment. The large copper block features a hole for the thermistor on one side and the Peltier device with heat sink can be seen mounted on the other side. Two screw holes are visible for clamping the block around a brass rod holding a resonator.

Chapter 5

Experimental Method

The purpose of this chapter is to discuss the methodology of how the experiment was conducted to ensure rigorous scientific processes were followed. There will likely be references to discussions conducted in chapter 2 and chapter 4 where the underlying methodology of some steps taken in the method will have been explained in greater detail when they were introduced in their respective chapters.

5.1 Pre-Sweep Calibrations

Before an experiment sweep can begin, there are a number of steps that must be taken to ensure that the data collection process is as accurate as possible. It is necessary to ensure that light is coupled into the resonator by following the coupling and refining processes described in section 3.3. Once light is successfully coupled to the resonator, the experiment laser must be switched on and given enough time to stabilise. With the laser operational, the desired substrate must be mounted on the attocube on top of the nanocube. This is best done by first mounting the substrate to a slide and screwing the slide into the top of the attocube. The nanocube is switched on and adjusted using the offset dial of the y-axis to move the nanocube position to 99 µm. The substrate is then brought closer to the resonator by using the translation dial on the translation stage underneath the nanocube. After the rough translation is complete, the final movement is made by using the attocube on top of the nanocube. We set the offset of the attocube to 100 V before moving it into place with the stepping functionality. The stepping movement is done with the attocube frequency set to 120 Hz and the attocube voltage set to 12 V. At this frequency and voltage the movement is slow enough that the substrate can make contact with the resonator with minimal damage or changes to the coupling conditions. Moving the substrate faster than this would reduce the time the substrate takes to make contact with the resonator but carries a higher risk of damaging the resonator. We use the audible feedback mechanism from the attocube (section 4.5) to indicate when contact between the resonator and the substrate is made. We then reduce the nanocube offset by 1 µm to 98 µm and reduce the attocube offset voltage by 100 V to 0 V. We turn on the temperature controller and check that the connections between the temperature controller, the thermistor and the Peltier are connected. The cardboard box is then placed over the setup, this is discussed in section 4.9. The purpose of reducing the offsets of the attocube and nanocube are to move the substrate out of the evanescent field of the resonator. When the substrate makes contact it can deform the resonator. This can change the evanescent field and lead to less conclusive data. Moving the substrate out of the evanescent field ensures it is not deforming the resonator and allows us to collect data on the interaction the substrate makes with the evanescent field when it first enters it during a sweep.

The scan control on the laser is switched on to couple into the modes of the resonator. We ensure the detector is plugged into an oscilloscope so that we can see the modes. As the substrate should have been moved sufficiently outside of the evanescent field of the resonator, the oscilloscope should display modes from the light in the resonator unperturbed by the substrate.

We check the polarisation of the light entering the resonator using the method described in section 5.1.1 below. One must measure the FSR of several modes to determine the location of the modes within the resonator. We change the oscilloscope settings and the laser scan control settings to observe a single mode on the oscilloscope. We launch the python script described in section 4.3.2 and perform the calibration process outlined in section 4.3.2 to generate the frequency axis on the python script oscilloscope. Once the frequency calibration is complete we run a test sweep by adjusting the position of the coupling prism but without moving the substrate. This generates .dat files for the MATLAB script discussed in section 4.3.3 to obtain values for the Q-factor and linewidth of the resonator. The calibration process is repeated until a mode is found with a suitable linewidth and Q-factor. The position of the coupling prism is set to match the position during the test sweep that gives the highest Q-factor, as this position corresponds with the lowest linewidth.

If we are expecting mode broadening to occur, we will modify this potion such that the resonator is slightly under-coupled. This is a precaution so that when mode broadening occurs, the increased losses in the resonator keep the coupling regime from becoming over-coupled slightly longer. This is useful for data analysis as over-coupling makes it harder to distinguish the frequency of the resonance.

5.1.1 Polarisation Control

We need to control the polarisation of the light entering the setup because we expect the effects of the dielectric substrates to change depending on if the light couples to TE or TM polarised modes. We utilise two methods of polarisation control simultaneously: a polarising beam splitter (PBS) and a paddle fibre polarisation controller. The functionality of each of these is described below.

Polarising Beam Splitter

The PBS is a cube comprised of two triangular prisms of different refractive indices that are then glued together (see figure 5.1a). The cube is mounted on a slide that can be screwed onto the front of a detector. The different refractive indices allow a PBS to separate an incident beam into a transmitted beam and a reflected beam where the transmitted beam and reflected beam have different polarisations (see figure 5.1b). When mounted in front of a detector, only the transmitted beam will pass through the PBS and into the detector.

Paddle Fibre Polarisation Controller

The PBS is good for determining the polarisation of light entering the detector, but it cannot change the polarisation of the light entering the resonator. We use Thorlabs three-paddle polarization controllers to change the polarisation of the light. This helps ensure we are coupling into the correct mode polarisation. These controllers combine a quarter-wave plate, half-wave plate and another quarter-wave plate into a series that allows one to transform an arbitrary polarisation state into a different arbitrary polarisation state.

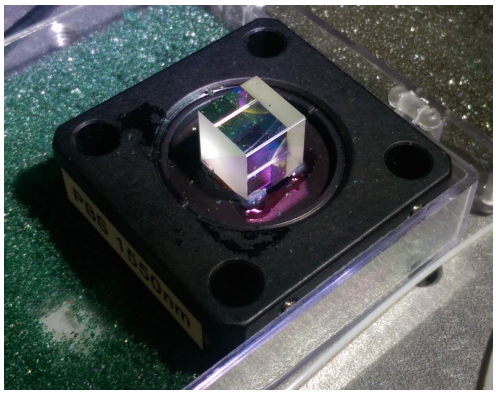

(A) Photograph of the PBS used to ensure the correct polarisation of light is tested.

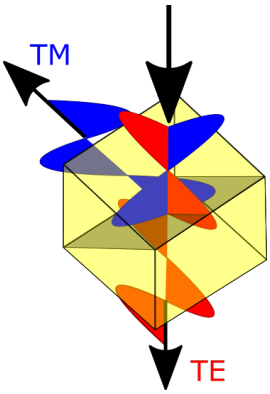

(B) Diagram showing how the PBS works with an example light ray passing through it. Note the incident beam contains both TE and TM polarised light however the PBS splits this into a reflected beam of TM light and a transmitted beam of TE light. The polarisation of the transmitted and reflected beams is dependant on the orientation of the PBS relative to the incident light wave.

FIGURE 5.1: The PBS used in the experiment.

The mechanism for this action is in the function of each paddle. Single-mode fibre is looped several times into a spool that is centred in each paddle. The spools cause a stress induced birefringence in the fibre. This transforms each paddle into a fractional wave plate. The three-paddle design contain spools that act as quarter-wave plates at each end and a half-wave plate in the middle. The amount of birefringence induced depends on the wave-length of light used, the number of fibre loops in the spool, and the diameter of the spool. We can form an arbitrary polarisation state by rotating each of the paddles.

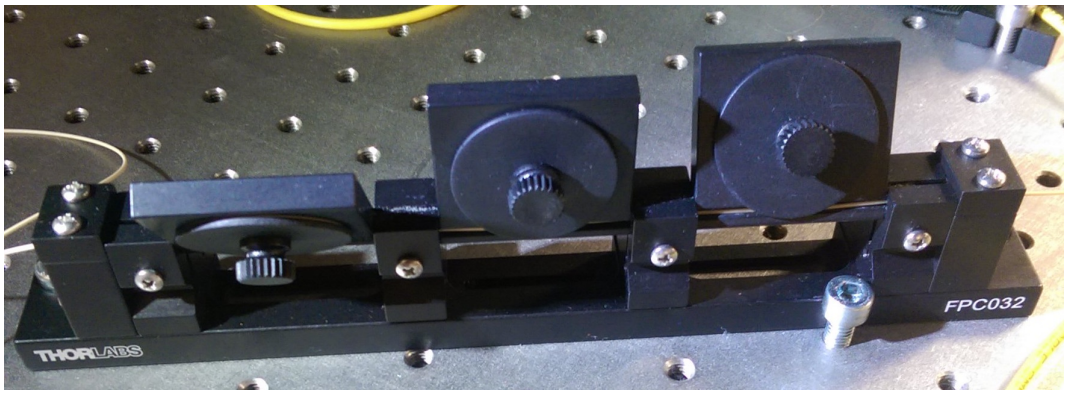

FIGURE 5.2: Photograph of the paddle fibre polarisation controller used.

Polarisation Test

There is a simple process that can be done to check and modify the polarisation of the light entering the setup. If we wish to study TE polarised modes, we must minimise the intensity of the TM polarised modes. To do this we observe the TM polarised modes on the oscilloscope by orienting the PBS in front of the detector such that the

reflected beam is TE polarised light and the transmitted beam is TM polarised light. We then adjust each paddle of the paddle fibre polarisation controller to minimise the TM polarised light in the transmitted beam. This has the effect of changing the polarisation of the incident beam to be TE linearly polarised, maximising the intensity of the light in the TE polarised reflected beam. When the PBS is removed from in front of the detector, this results in seeing only TE polarised modes on the oscilloscope. If we wish to study TM polarised modes we can repeat this process with the orientation of the PBS changed such that the transmitted beam is TE polarised and the reflected beam is TM polarised.

5.2 Data Collection Method

The method for collecting data is centred mostly on the use of the python script (section 4.3.2) that receives data from the oscilloscope. After following the pre-sweep calibrations (section 5.1), the active channel within the script is set to control the position of the substrate. The substrate should not have moved so remain outside of the evanescent field of the resonator at this point. We adjust the offset voltage to the attocube controlling the substrate to be 0.1 V. This avoids floating point zero-error in python that can prevent the file being analysed in MATLAB. We initiate the data collection method from within the python script by starting an offset sweep on the substrates attocube channel. This will incrementally adjust the offset of the attocube wit the substrate until we stop it or it reaches the limit of the offset voltage for the attocube. We will stop the offset sweep if the mode disappears, becomes severely deformed or moves out of the oscilloscope sample range.

We pass the collected data to the MATLAB script to produce the raw result plots. These plots are useful in identifying any changes in linewidth which could be a sign of mode broadening if we are testing a substrate $n_{\text{substrate}} > n_{\text{resonator}}$. We can use the presence of linewidth changes to tailor the range of motion for the substrate on subsequent sweeps, if no linewidth changes are present it could be a sign that the substrate is not interacting with the resonator, possibly being too far away from the evanescent field of the resonator. If the output of the sweep suggests everything is working correctly, and there is a sign of interaction between the substrate and the resonator, the position of the substrate is reset by resetting the offset voltage of the attocube. Subsequent sweeps are taken with different file names to mitigate confusion when analysed by MATLAB. Often times it is useful to take a sweep with the substrate starting close to the resonator and moving away. This can be a useful sanity check as the direction of any changes should match the direction the substrate is moving in.

Once a satisfactory amount of data is collected for a single substrate, the box is removed and the attocube is used to move the substrate away from the resonator. Once there is a visible gap between the substrate and the resonator, the coarse translation dial below the nanocube is used to move the substrate away from the resonator faster. Once the substrate is safely out of the way of the resonator, the substrate is replaced with the next substrate to test and the entire process is repeated with the same mode remaining on the oscilloscope if possible. The python script allows for the resetting and recalibrating of the frequency axis without restarting the program meaning the optimal position for the coupling prism can be updated part way through the data collection process. Keeping the same mode in focus makes for a stronger comparison when generating the relationship between refractive index and

frequency detuning of the resonator mode as the expected frequency shifts were all calculated from the same mode in Foreman et al.

Chapter 6

Experimental Results

This chapter will discuss the results and analysis of this project. The majority of the discussion of this experiment will reside in the following chapter (Chapter 7).

6.1 Germanium

6.1.1 TE Mode Sweep

The results of the sweep using the germanium substrate are plotted. Figure 6.1 shows that values remained constant through the majority of the sweep but eventually the distance between the resonator and substrate decreased to such a point that the substrate began to have an impact on the mode. The impact on this mode can be seen by the change in each of the sub-plots present. Around step 90 it can be noted that there is an inflection in the frequency shift and the changes in linewidth, Q-factor and coupling contrast begin to reduce. We note that the step 89.9 must be the point that we can consider the substrate and resonator to be in contact.

Due to the presence of an ambient shift in the frequency through the majority of the sweep despite linewidth and Q-factor remaining constant, we can fit a linear line to the first part of this figure. The results of this linear fit can be seen in figure 6.2. Here we arbitrarily determine the bounds between which a linear fit is calculated. For the germanium mode sweep the bounds of 50 and 67 were selected for the linear fit. 67 was chosen due to its distance from the position where the linewidth and Q-factor begin to change. We can subtract this linear fit to produce a clearer plot of the effect that the substrate has had on the frequency of the mode. This can be seen in sub-plot 3 where an obvious blue-shift can be noted. The error for the frequency shift is calculated from the standard deviation of the linear fit line where $\sigma = 4.67$.

The pseudo-colour plot (figure 6.3 highlights where any change in intensity of the light at the detector may have occurred. For the germanium substrate sweep we can see an obvious colour change in the mode from step 88 until step 90 at the end of the sweep range.

6.1.2 TM Mode Sweep

The results of the sweep using the germanium substrate are plotted. Figure 6.4 shows that linewidth remained constant through the majority of the sweep but increased around step 33. Around step 33 it can be noted that there is a sudden change in linewidth, Q-factor and coupling contrast. We note that the step 33 must be the point that we can consider the substrate and resonator to be in contact.

Due to the presence of an ambient shift in the frequency through the majority of the sweep despite linewidth and Q-factor remaining constant, we can fit a linear line to the first part of this figure. The results of this linear fit can be seen in figure 6.5.

Here we arbitrarily determine the bounds between which a linear fit is calculated. For the germanium mode sweep the bounds of 10 and 23 were selected for the linear fit. 23 was chosen due to its distance from the position where the linewidth and Q-factor begin to change. We can subtract this linear fit to produce a clearer plot of the effect that the substrate has had on the frequency of the mode. This can be seen in sub-plot 3 where a red-shift can be noted. The error for the frequency shift is calculated from the standard deviation of the linear fit line where $\sigma = 0.66$.

The pseudo-colour plot (figure 6.6 highlights where any change in intensity of the light at the detector may have occurred. For the germanium substrate sweep we can see an obvious colour change in the mode from step 33 until step 35 at the end of the sweep range.

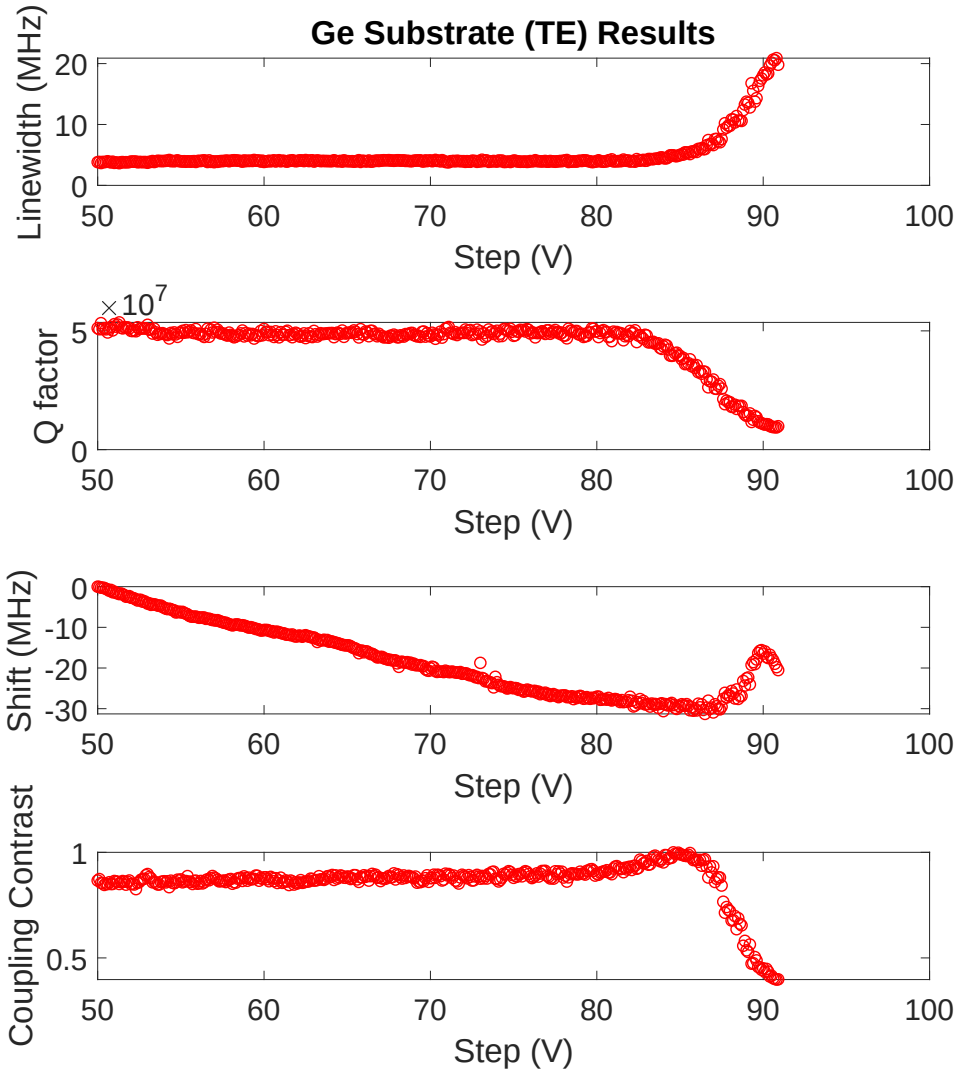

FIGURE 6.1: Raw output of the MATLAB script for the germanium substrate.

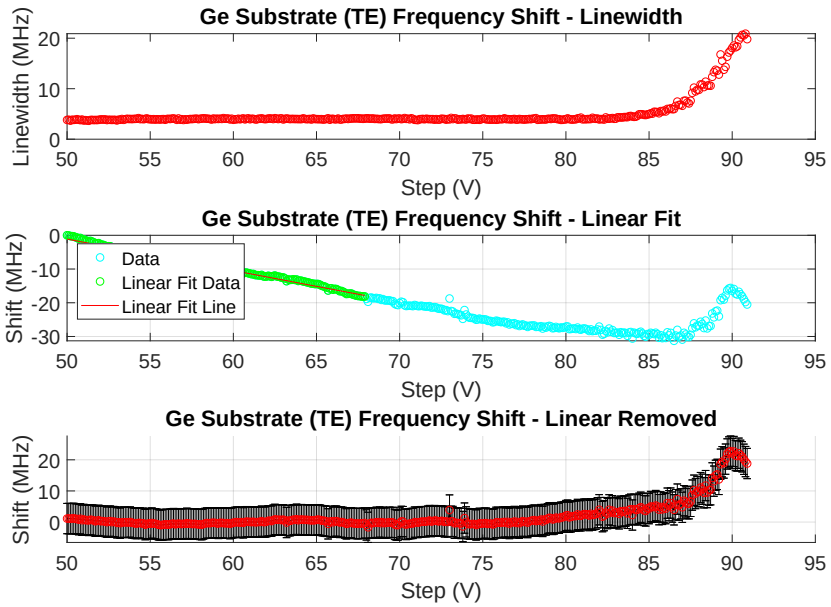

FIGURE 6.2: Analysed output of the MATLAB script for the germanium substrate. The second sub-figure features a linear fit line set at a step number before the substrate enters the evanescent field of the resonator. The third figures shows a more accurate frequency shift when the linear fit is removed from the shift data.

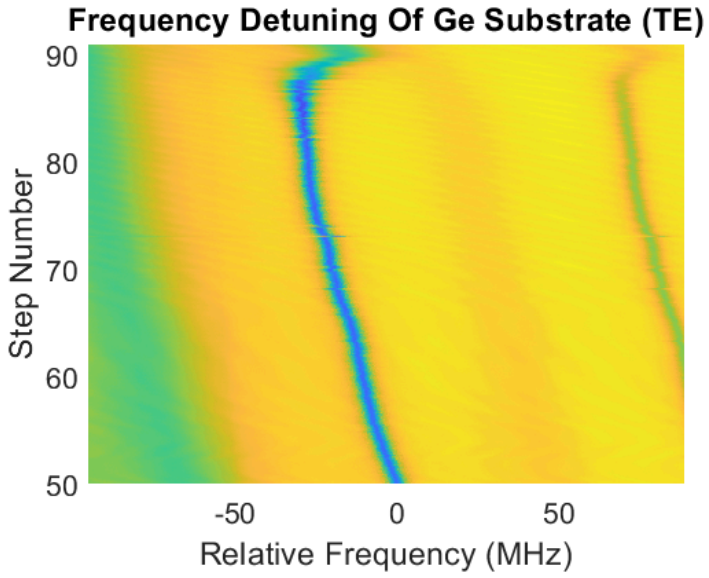

FIGURE 6.3: A pseudo-colour plot of the tested mode. The colour represents the intensity of the light at the detector. The dark line indicates the relative frequency of the mode and shows how it changed over the duration of the sweep.

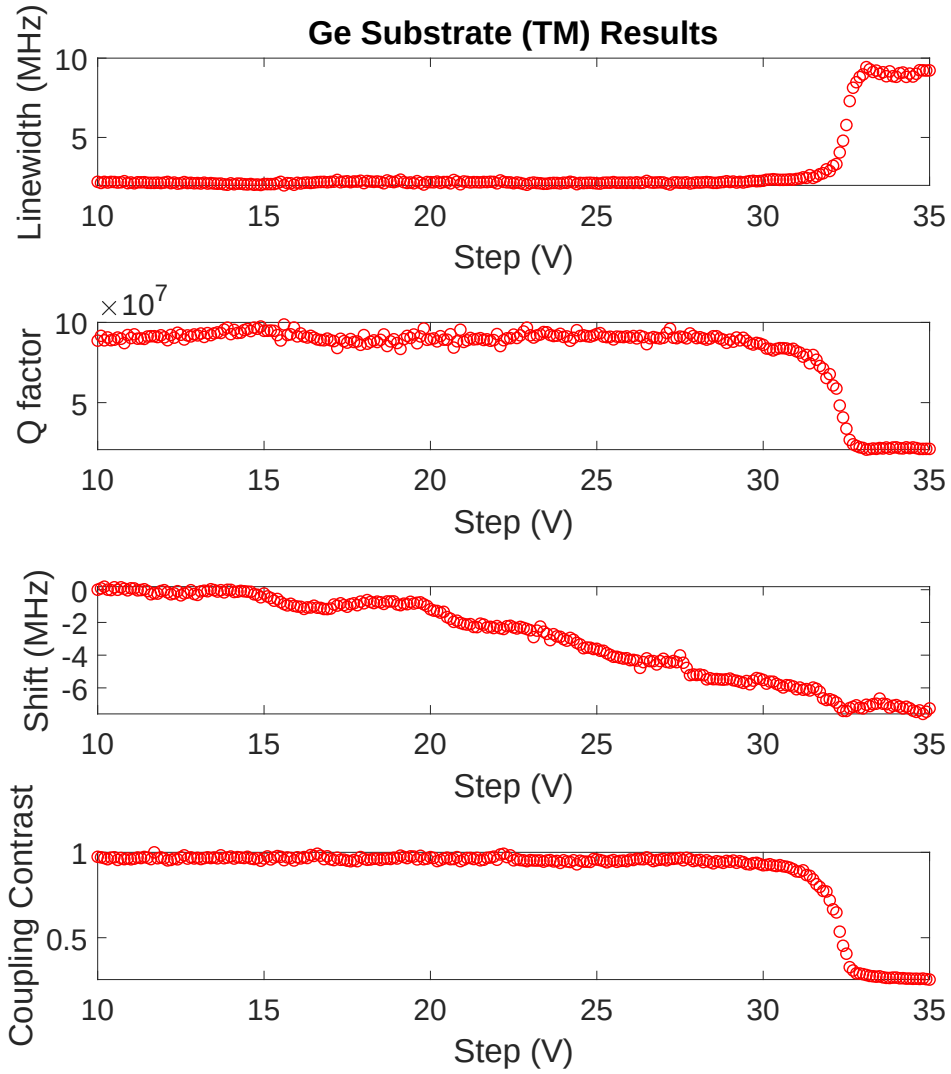

FIGURE 6.4: Raw output of the MATLAB script for the germanium substrate.

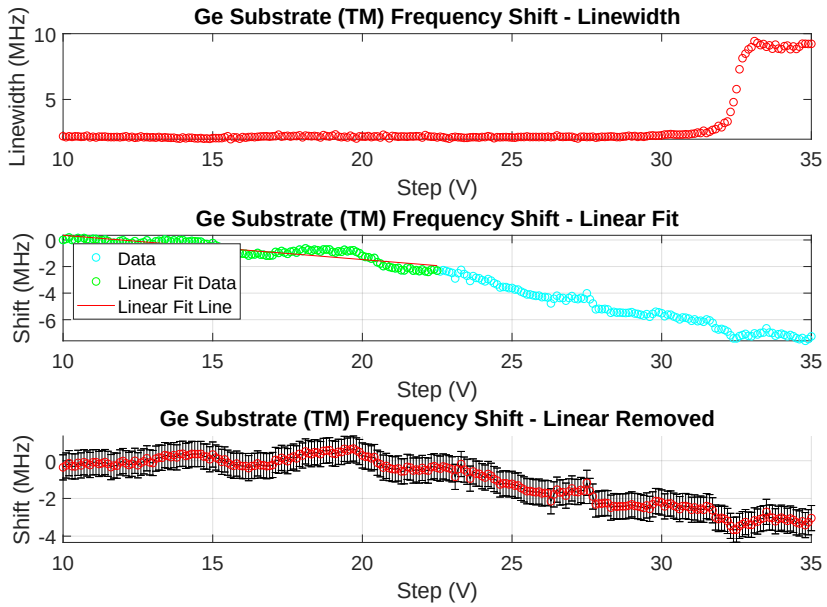

FIGURE 6.5: Analysed output of the MATLAB script for the germanium substrate. The second sub-figure features a linear fit line set at a step number before the substrate enters the evanescent field of the resonator. The third figures shows a more accurate frequency shift when the linear fit is removed from the shift data.

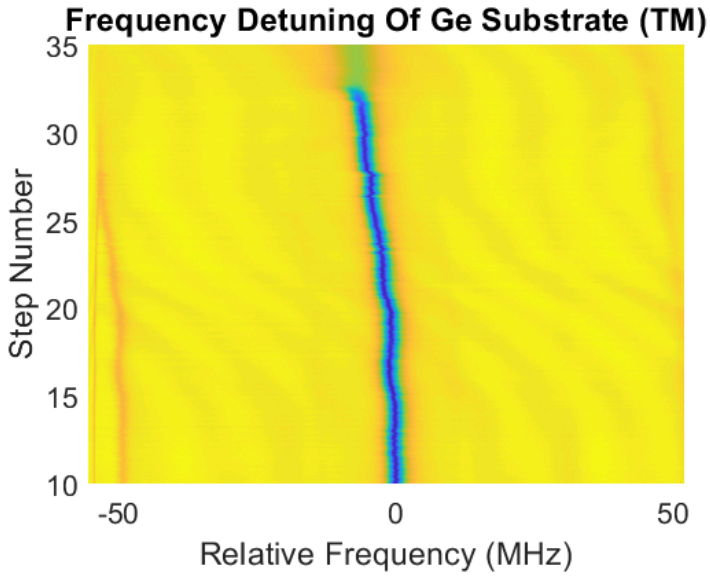

FIGURE 6.6: A pseudo-colour plot of the tested mode. The colour represents the intensity of the light at the detector. The dark line indicates the relative frequency of the mode and shows how it changed over the duration of the sweep.

6.2 Silicon

6.2.1 TE Mode Sweep

The results of the sweep using the silicon substrate are plotted. Figure 6.7 shows that linewidth, Q-factor and coupling contrast remained constant from the beginning of the sweep until step 20 where they begin to change. The silicon substrate results show a large amount of resemblance to the germanium results but the step values that changes to linewidth and Q-factor begin to occur at is much less than for germanium. At step 25 it can be noted that there is an inflection in the frequency shift and the changes in linewidth, Q-factor and coupling contrast begin to reduce. We note that the step 25.5 must be the point that we can consider the substrate and resonator to be in contact.

There remains the presence of an ambient shift in the frequency through the majority of the sweep similar to the one noted for germanium. The gradient of the shift for silicon appears to be less than the gradient of the shift present in germanium. We fit a linear line to the first part of this figure to make the effect of the substrate more apparent. The results of this linear fit can be seen in figure 6.8. Here we arbitrarily determine the bounds between which a linear fit is calculated. For the silicon mode sweep the bounds of 0 and 13 were selected for the linear fit. 13 was chosen due to its distance from the position where the linewidth and Q-factor begin to change. We can subtract this linear fit to produce a clearer plot of the effect that the substrate has had on the frequency of the mode. This can be seen in sub-plot 3 where a blue-shift can be noted. The error for the frequency shift is calculated from the standard deviation of the linear fit line where $\sigma = 1.25$.

The pseudo-colour plot (figure 6.9 displays a clear boundary where a change in the intensity of the light at the detector can be seen. For the silicon substrate sweep we can see an obvious colour change in the mode from step 24 until step 30 at the end of the sweep range.

6.2.2 TM Mode Sweep

The results of the sweep using the silicon substrate are plotted. Figure 6.10 shows that linewidth remained constant from the beginning of the sweep until step 31 where it begins to increase. At step 35 it can be noted that there is an inflection in the linewidth. We note that the step 35.1 must be the point that we can consider the substrate and resonator to be in contact, proven further by reference to the pseudo-colour plot.

There remains the presence of an ambient shift in the frequency through the majority of the sweep, with an inflection at step 23. We fit a linear line to the first part of this figure to make the effect of the substrate more apparent. The results of this linear fit can be seen in figure 6.11. Here we arbitrarily determine the bounds between which a linear fit is calculated. For the silicon mode sweep the bounds of 10 and 23 were selected for the linear fit. 23 was chosen due to its distance from the position where the linewidth and Q-factor begin to change. We can subtract this linear fit to produce a clearer plot of the effect that the substrate has had on the frequency of the mode. This can be seen in sub-plot 3 where a blue-shift can be noted. The error for the frequency shift is calculated from the standard deviation of the linear fit line where $\sigma = 1.26$.

The pseudo-colour plot (figure 6.12 displays a clear boundary where a change in the intensity of the light at the detector can be seen. For the silicon substrate sweep

we can see an obvious colour change in the mode from step 34 until step 40 at the end of the sweep range.

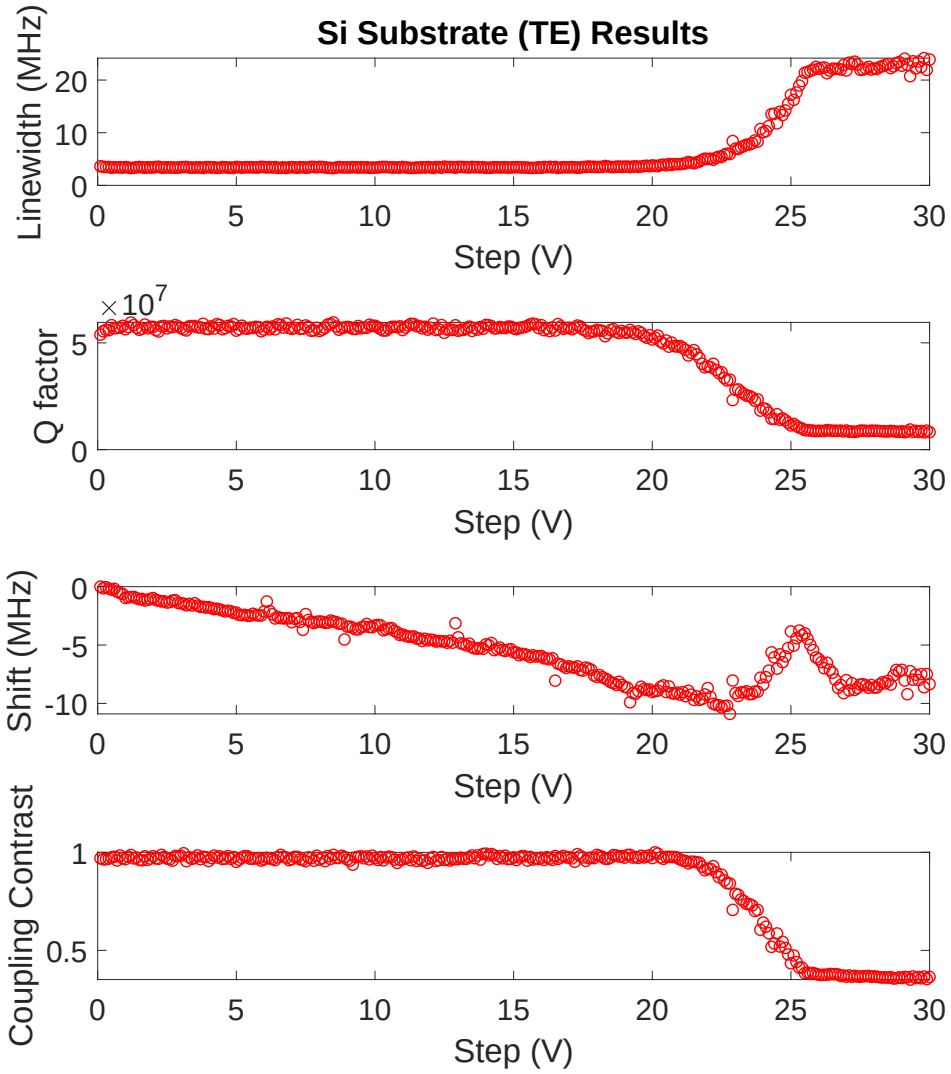

FIGURE 6.7: Raw output of the MATLAB script for the silicon substrate.

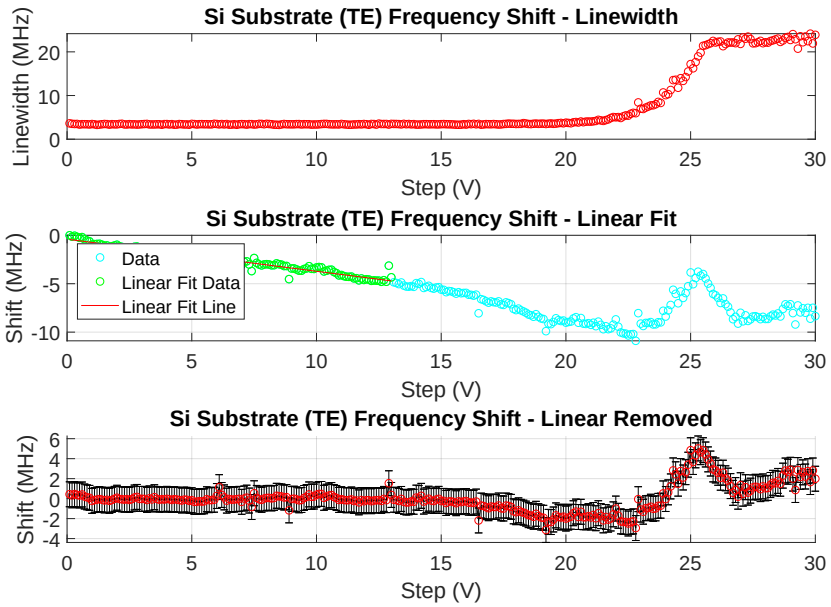

FIGURE 6.8: Analysed output of the MATLAB script for the silicon substrate. The second subfigure features a linear fit line set at a step number before the substrate enters the evanescent field of the resonator. The third figures shows a more accurate frequency shift when the linear fit is removed from the shift data.

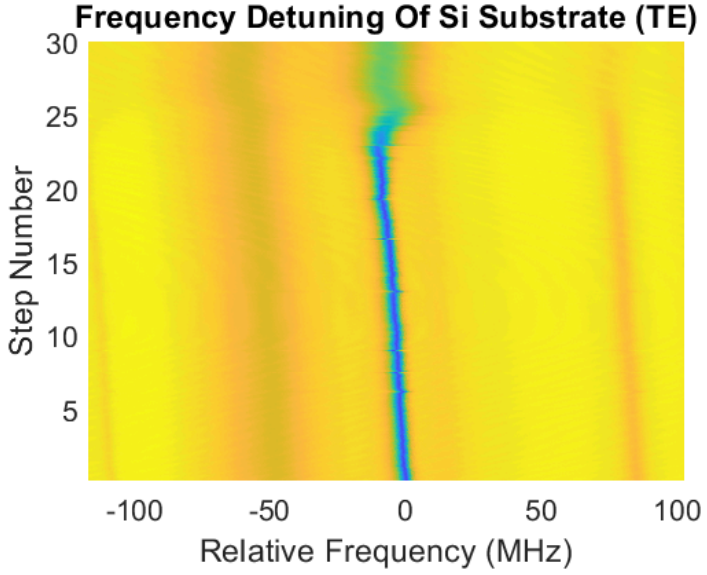

FIGURE 6.9: A pseudo-colour plot of the tested mode. The colour represents the intensity of the light at the detector. The dark line indicates the relative frequency of the mode and shows how it changed over the duration of the sweep.

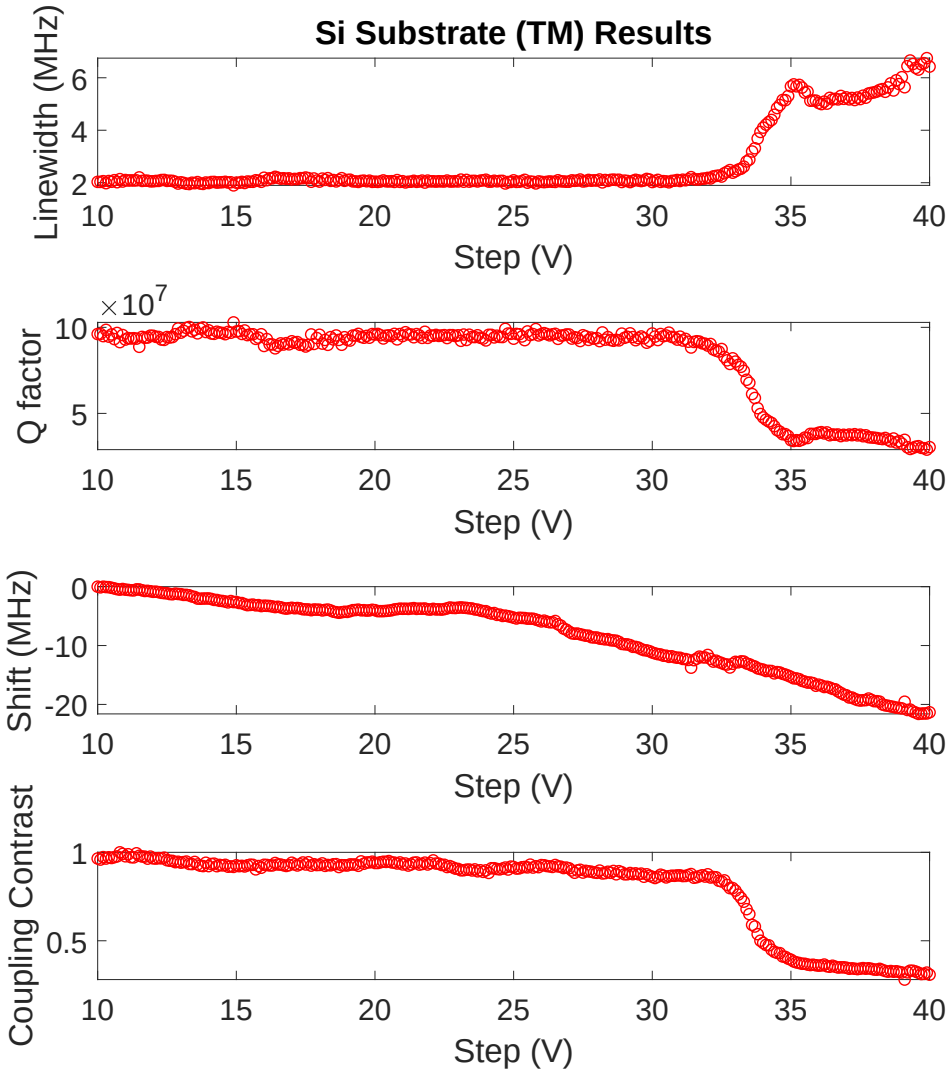

FIGURE 6.10: Raw output of the MATLAB script for the silicon substrate.

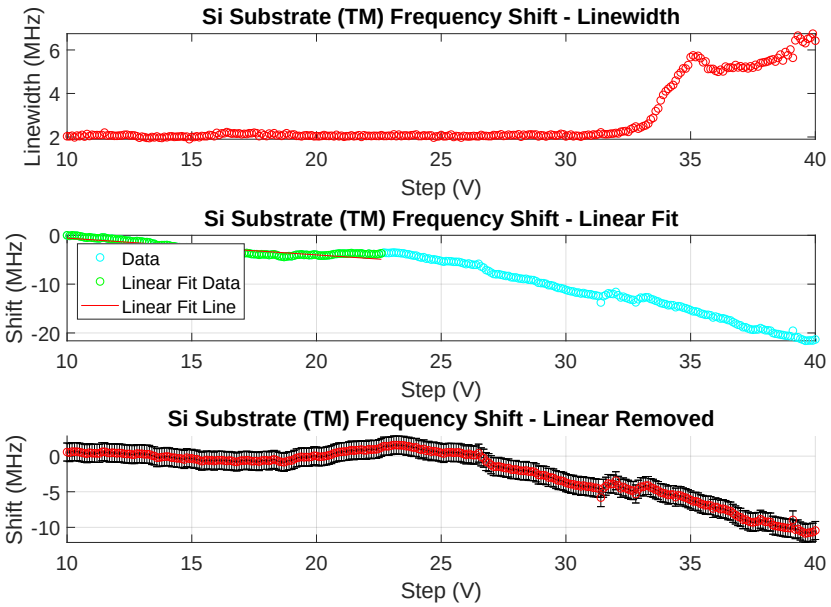

FIGURE 6.11: Analysed output of the MATLAB script for the silicon substrate. The second subfigure features a linear fit line set at a step number before the substrate enters the evanescent field of the resonator. The third figures shows a more accurate frequency shift when the linear fit is removed from the shift data.

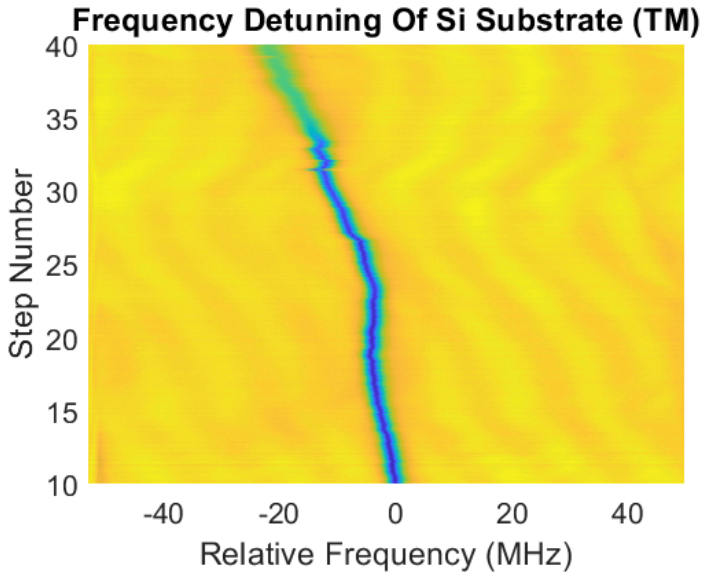

FIGURE 6.12: A pseudo-colour plot of the tested mode. The colour represents the intensity of the light at the detector. The dark line indicates the relative frequency of the mode and shows how it changed over the duration of the sweep.

6.3 Zinc Selenide

6.3.1 TE Mode Sweep

The results of the sweep using the zinc selenide substrate are plotted. Figure 6.13 shows that linewidth, Q-factor and coupling contrast remained constant through from the beginning of the sweep until step 17 where they begin to change. A small oscillation can be seen in the coupling contrast and Q-factor from step 0 to step 5 however the oscillation does not appear to change the value by a significant amount. The zinc selenide substrate results show a resemblance to the previous TE results for the changes in linewidth and Q-factor however the shape of the frequency shift sub-plot is noticeably different. There is no inflection point present in the frequency shift but an increase in gradient of the frequency shift line can be seen after step 21. The range of step values for this sweep is similar to the range of step values present in the silicon substrate results. At step 22 it can be noted that there is a large change in the coupling contrast and linewidth of the mode. The presence of discontinuous jumps after this step suggests that we can note that the step 22.6 must be the point that we can consider the substrate and resonator to be in contact.

The ambient shift in the frequency shift of the mode remains in the zinc selenide substrate sweep results. We repeat the application of fitting a linear line to the first part of this figure to make the effect of the substrate more apparent. The results of this linear fit can be seen in figure 6.14. Here we arbitrarily determine the bounds of 0 and 14 between which a linear fit is calculated. 14 was chosen due to its distance from the designated contact position of the resonator and substrate. We can subtract this linear fit to produce a clearer plot of the effect that the substrate has had on the frequency of the mode. This can be seen in sub-plot 3 where a red-shift can be noted. The error for the frequency shift is calculated from the standard deviation of the linear fit line where $\sigma = 1.87$.

The pseudo-colour plot (figure 6.15 displays a clear boundary where a change in the intensity of the light at the detector can be seen. For the zinc selenide substrate sweep we can see an obvious colour change in the mode at step 20 and the mode becomes indistinguishable from the background after step 23.

6.3.2 TM Mode Sweep

The results of the sweep using the zinc selenide substrate are plotted. Figure 6.16 shows that linewidth, Q-factor and coupling contrast remained constant through from the beginning of the sweep until step 31 where they begin to change. At step 33 it can be noted that there is a large change in the coupling contrast and linewidth of the mode. The presence of discontinuous jumps after this step suggests that we can note that the step 33.3 must be the point that we can consider the substrate and resonator to be in contact.

The ambient shift in the frequency shift of the mode remains in the zinc selenide substrate sweep results. We repeat the application of fitting a linear line to the first part of this figure to make the effect of the substrate more apparent. The results of this linear fit can be seen in figure 6.17. Here we arbitrarily determine the bounds of 0 and 18 between which a linear fit is calculated. 18 was chosen due to its distance from the designated contact position of the resonator and substrate. We can subtract this linear fit to produce a clearer plot of the effect that the substrate has had on the frequency of the mode. This can be seen in sub-plot 3 where a red-shift can be

noted. The error for the frequency shift is calculated from the standard deviation of the linear fit line where $\sigma = 3.03$.

The pseudo-colour plot (figure 6.18 displays a clear boundary where a change in the intensity of the light at the detector can be seen. For the zinc selenide substrate sweep we can see an obvious colour change in the mode at step 34.

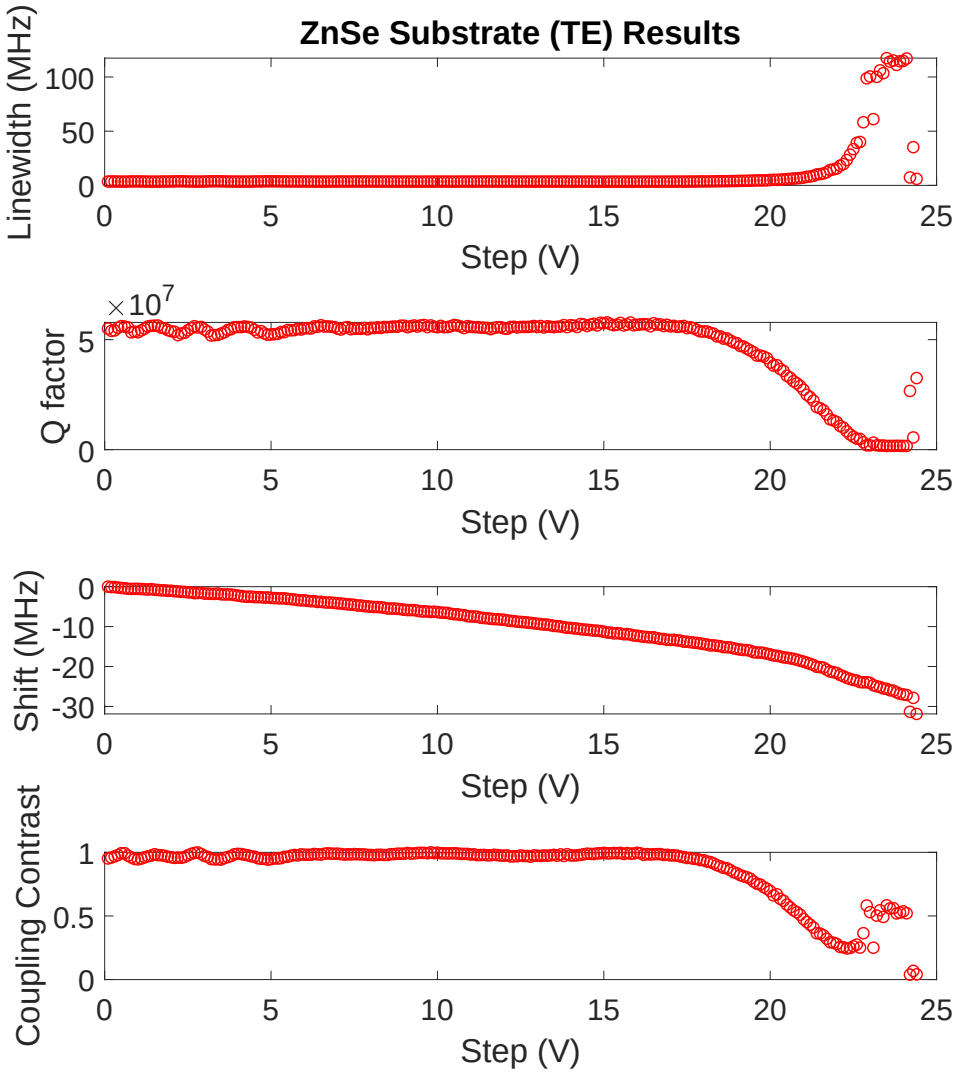

FIGURE 6.13: Raw output of the MATLAB script for the zinc selenide substrate.

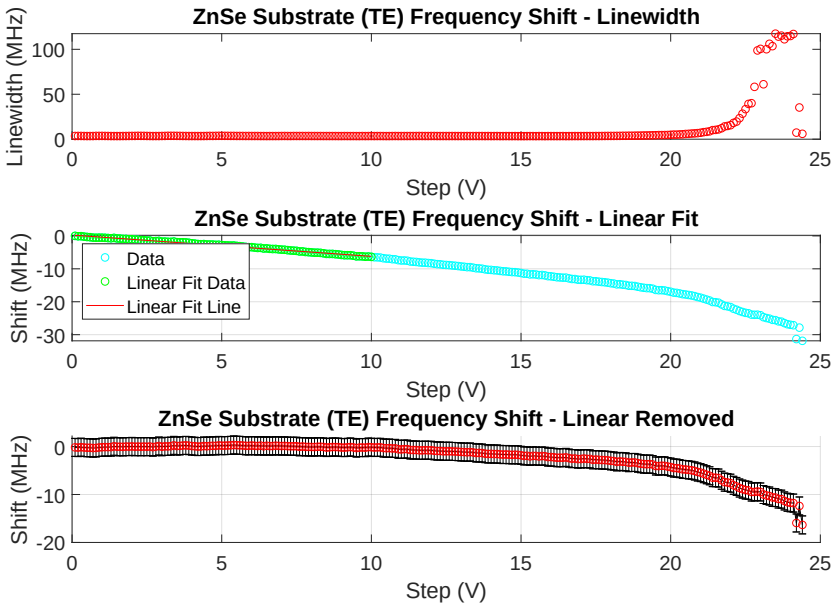

FIGURE 6.14: Analysed output of the MATLAB script for the zinc selenide substrate. The second subfigure features a linear fit line set at a step number before the substrate enters the evanescent field of the resonator. The third figures shows a more accurate frequency shift when the linear fit is removed from the shift data.

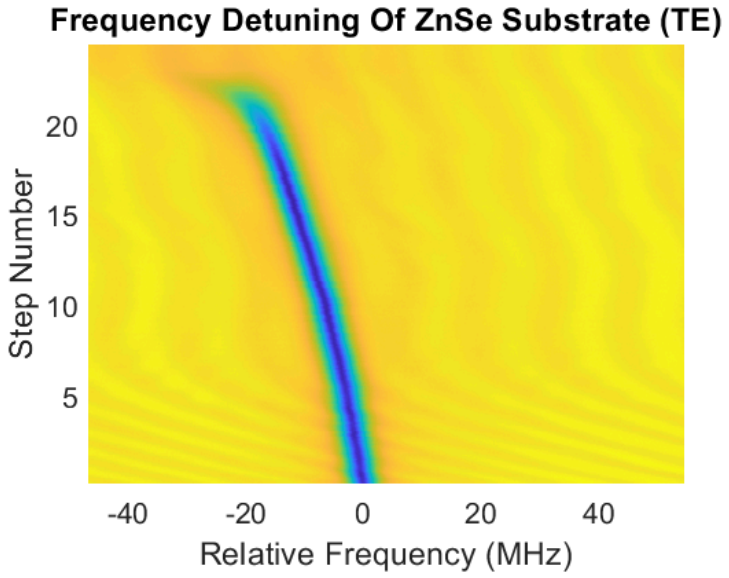

FIGURE 6.15: A pseudo-colour plot of the tested mode. The colour represents the intensity of the light at the detector. The dark line indicates the relative frequency of the mode and shows how it changed over the duration of the sweep.

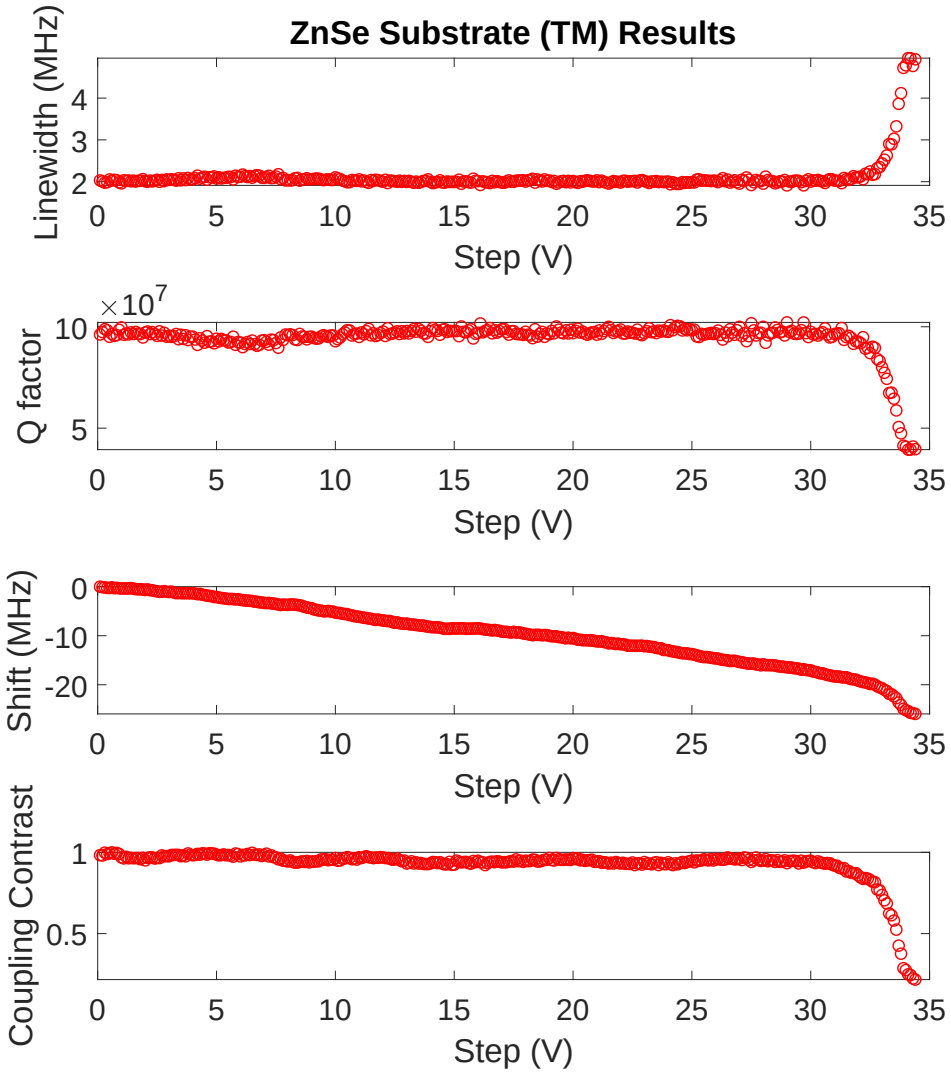

FIGURE 6.16: Raw output of the MATLAB script for the zinc selenide substrate.

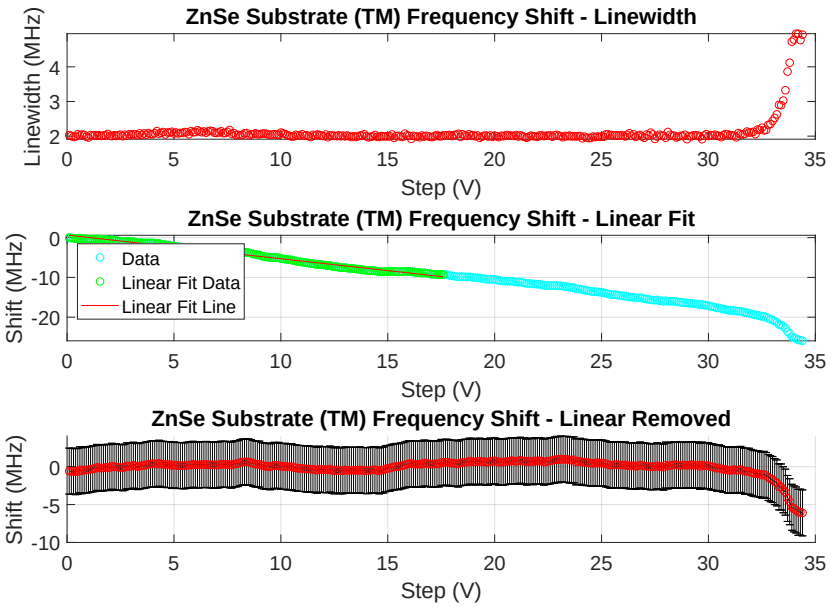

FIGURE 6.17: Analysed output of the MATLAB script for the zinc selenide substrate. The second subfigure features a linear fit line set at a step number before the substrate enters the evanescent field of the resonator. The third figures shows a more accurate frequency shift when the linear fit is removed from the shift data.

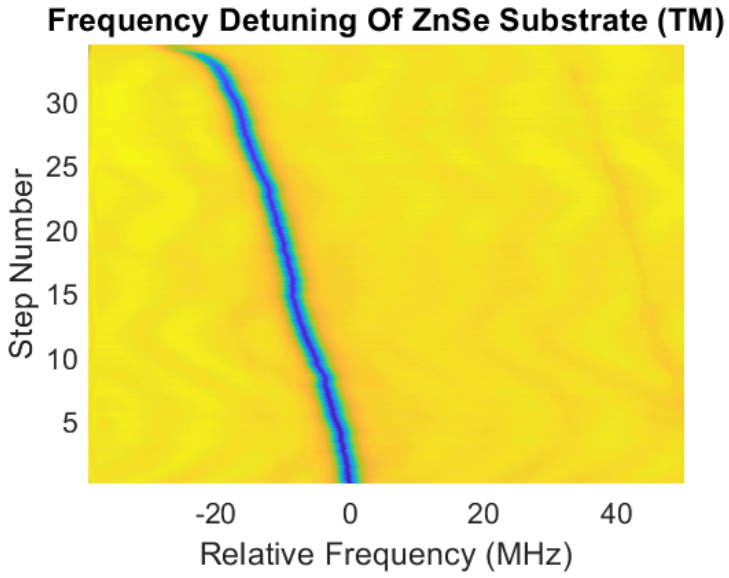

FIGURE 6.18: A pseudo-colour plot of the tested mode. The colour represents the intensity of the light at the detector. The dark line indicates the relative frequency of the mode and shows how it changed over the duration of the sweep.

6.4 Zinc Sulfide

6.4.1 TE Mode Sweep

The results of the sweep using the zinc sulfide substrate are plotted. Figure 6.19 shows that linewidth, Q-factor and coupling contrast remained constant through from the beginning of the sweep until step 13 where they begin to change. A small oscillation can be seen in the linewidth and Q-factor from step 19 to step 22 however the oscillation appears to occur after the values have already changed significantly from their constant values from earlier in the sweep. The zinc sulfide substrate results show a resemblance to the previous results for the changes in linewidth, Q-factor and coupling contrast. The shape of the frequency shift sub-plot bears a similar shape to that seen in the zinc selenide substrate results. We can notice a slight change in the shape of the frequency shift curve that occurs after step 18. A combination of the position of this shape change and the position of the changes to linewidth and Q-factor suggest that we can note that the step 18.5 must be the point that we can consider the substrate and resonator to be in contact.

The ambient shift in the frequency shift of the mode remains in the zinc sulfide substrate sweep results. We repeat the application of fitting a linear line to the first part of this figure to make the effect of the substrate more apparent. The results of this linear fit can be seen in figure 6.20. Here we arbitrarily determine the bounds of 0 and 8 between which a linear fit is calculated. 8 was chosen due to its distance from the designated contact position of the resonator and substrate. We can subtract this linear fit to produce a clearer plot of the effect that the substrate has had on the frequency of the mode. This can be seen in sub-plot 3 where a red-shift can be noted. The error for the frequency shift is calculated from the standard deviation of the linear fit line where $\sigma = 3.12$.

The pseudo-colour plot (figure 6.21 displays a clear boundary where a change in the intensity of the light at the detector can be seen. For the zinc sulfide substrate sweep we can see an obvious colour change in the mode at step 17 and the mode becomes indistinguishable from the background after step 19.

6.4.2 TM Mode Sweep

The results of the sweep using the zinc sulfide substrate are plotted. Figure 6.22 shows that linewidth, Q-factor and coupling contrast remained constant through from the beginning of the sweep until step 17 where they begin to change. We can notice a slight kink in the shape of the frequency shift curve that occurs at step 13 however there is more evidence from the =other measurements to suggest that the step 19.9 must be the point that we can consider the substrate and resonator to be in contact.

The ambient shift in the frequency shift of the mode remains in the zinc sulfide substrate sweep results. We repeat the application of fitting a linear line to the first part of this figure to make the effect of the substrate more apparent. The results of this linear fit can be seen in figure 6.23. Here we arbitrarily determine the bounds of 0 and 10 between which a linear fit is calculated. 10 was chosen due to its distance from the designated contact position of the resonator and substrate. We can subtract this linear fit to produce a clearer plot of the effect that the substrate has had on the frequency of the mode. This can be seen in sub-plot 3 where a red-shift can be noted. The error for the frequency shift is calculated from the standard deviation of the linear fit line where $\sigma = 1.49$.

The pseudo-colour plot (figure 6.24 displays a clear boundary where a change in the intensity of the light at the detector can be seen. For the zinc sulfide substrate sweep we can see an obvious colour change in the mode at step 20.

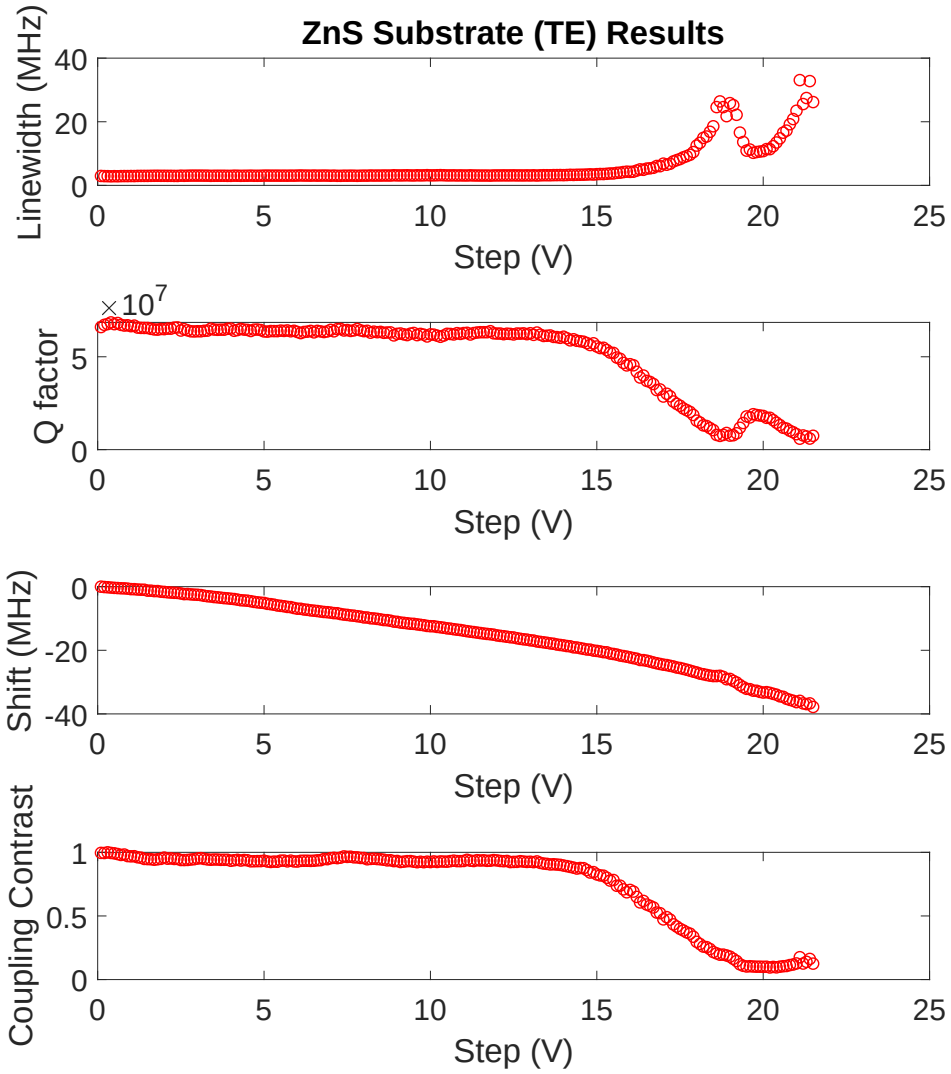

FIGURE 6.19: Raw output of the MATLAB script for the zinc sulfide substrate.

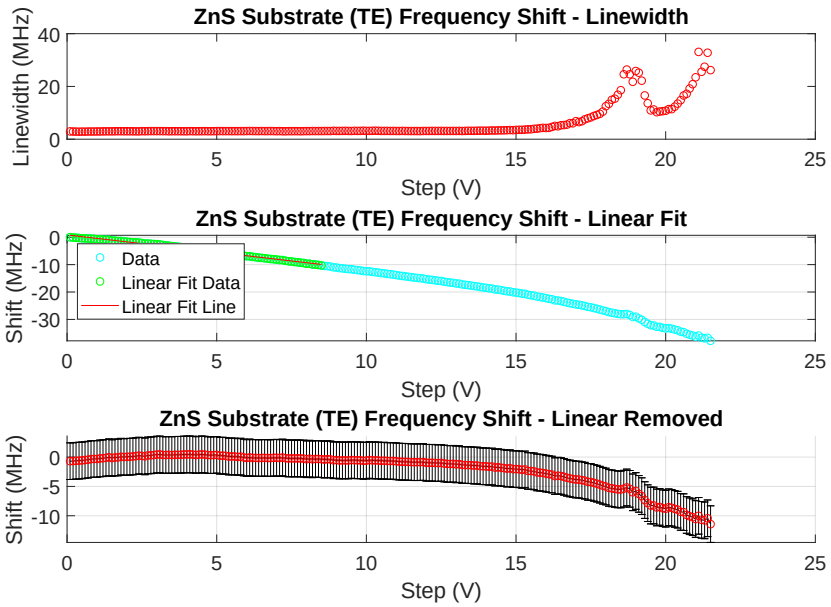

FIGURE 6.20: Analysed output of the MATLAB script for the zinc sulfide substrate. The second subfigure features a linear fit line set at a step number before the substrate enters the evanescent field of the resonator. The third figures shows a more accurate frequency shift when the linear fit is removed from the shift data.

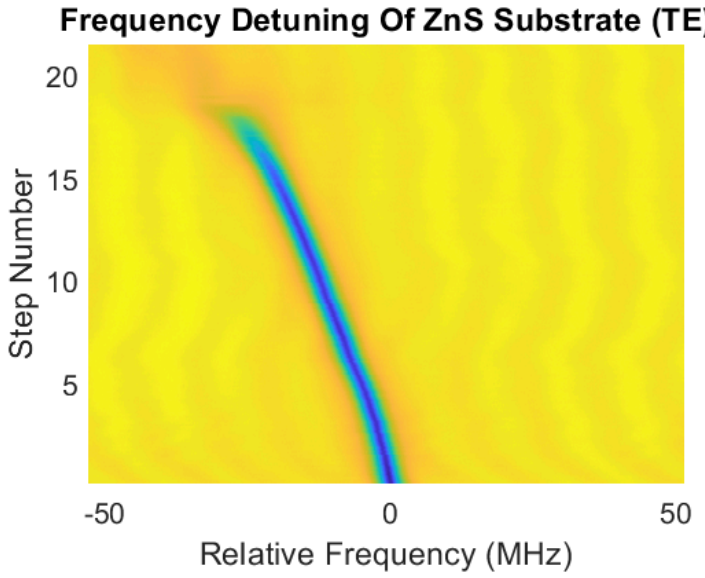

FIGURE 6.21: A pseudo-colour plot of the tested mode. The colour represents the intensity of the light at the detector. The dark line indicates the relative frequency of the mode and shows how it changed over the duration of the sweep.

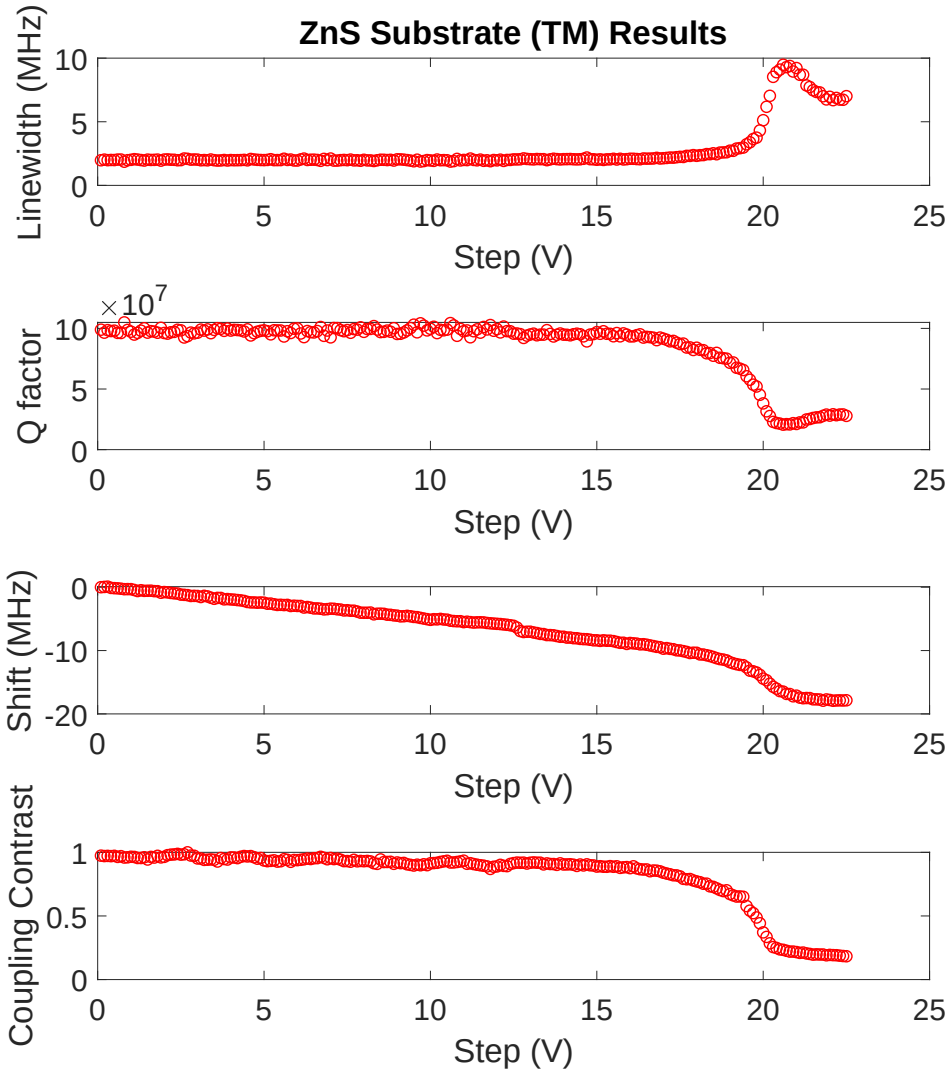

FIGURE 6.22: Raw output of the MATLAB script for the zinc sulfide substrate.

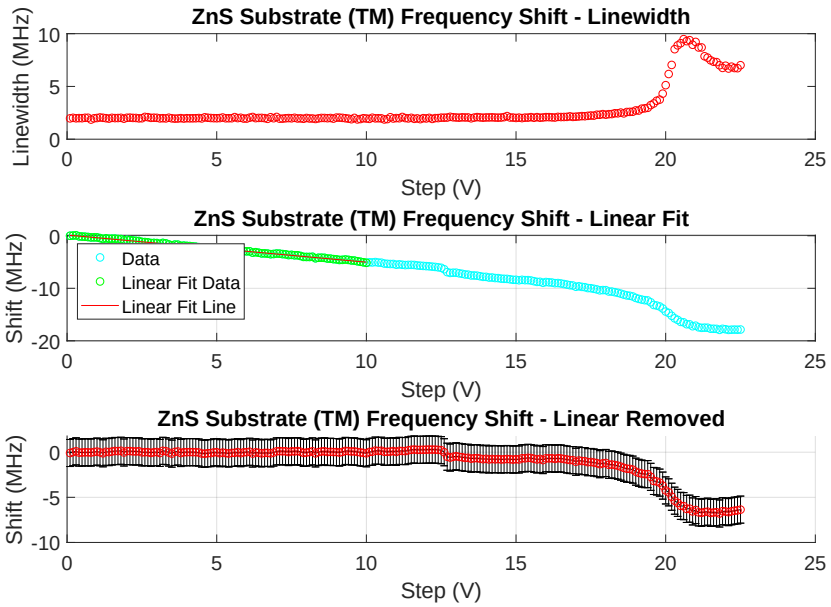

FIGURE 6.23: Analysed output of the MATLAB script for the zinc sulfide substrate. The second subfigure features a linear fit line set at a step number before the substrate enters the evanescent field of the resonator. The third figures shows a more accurate frequency shift when the linear fit is removed from the shift data.

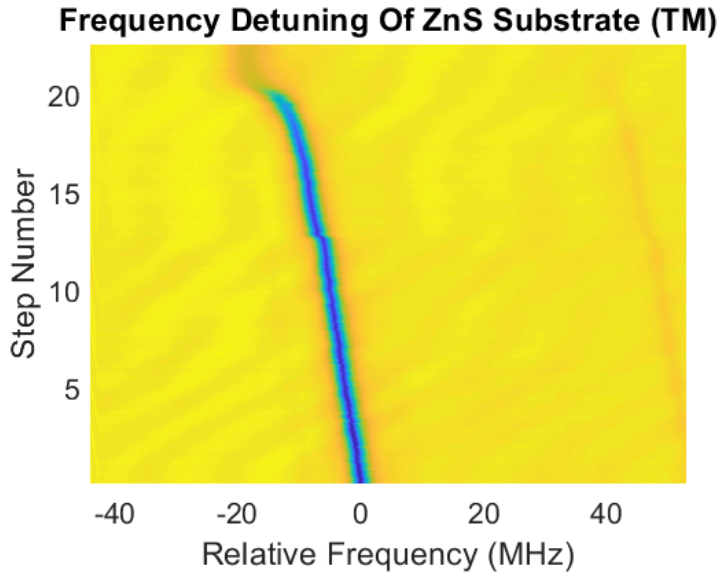

FIGURE 6.24: A pseudo-colour plot of the tested mode. The colour represents the intensity of the light at the detector. The dark line indicates the relative frequency of the mode and shows how it changed over the duration of the sweep.

6.5 Sapphire

6.5.1 TE Mode Sweep

The results of the sweep using the sapphire substrate are plotted. Figure 6.25 shows that linewidth, Q-factor and coupling contrast fluctuate seemingly randomly through the majority of the sweep. The oscillation in linewidth appears to fluctuate about a value of 5 MHz, the oscillation in Q-factor appears to fluctuate about a value of $4e7$ and the coupling contrast appears to oscillate about a value of 0.9. We can notice a slight change in the shape of the frequency shift curve that occurs after step 7. Closer examination of the linewidth, Q-factor and coupling contrast from step 7 to step 10 show that the sub-plots become more discontinuous compared to data between step 0 and step 7. We can use the presence of this discontinuity to note that step 7 must be the point that we can consider the substrate and resonator to be in contact.

The ambient shift in the frequency shift of the mode remains in the sapphire substrate sweep results. We repeat the application of fitting a linear line to the first part of this figure to make the effect of the substrate more apparent. The results of this linear fit can be seen in figure 6.26. Here we arbitrarily determine the bounds of 0 and 4 between which a linear fit is calculated. 4 was chosen due to its distance from the designated contact position of the resonator and substrate. We can subtract this linear fit to produce a clearer plot of the effect that the substrate has had on the frequency of the mode. This can be seen in sub-plot 3 where a red-shift can be noted. The error for the frequency shift is calculated from the standard deviation of the linear fit line where $\sigma = 2.27$.

The pseudo-colour plot (figure 6.27 does not show where a change in the intensity of the light at the detector can be seen. For the sapphire substrate sweep there is no colour change but discontinuous jumps can be seen around step 9.

6.5.2 TM Mode Sweep

The results of the sweep using the sapphire substrate are plotted. Figure 6.28 shows that linewidth is mostly constant throughout the sweep but increases after step 30. We can notice a slight change in the shape of the frequency shift curve that occurs after step 26. We note that step 30.4 must be the point that we can consider the substrate and resonator to be in contact. due to the change in shape of the traces at this step.

The ambient shift in the frequency shift of the mode remains in the sapphire substrate sweep results. We repeat the application of fitting a linear line to the first part of this figure to make the effect of the substrate more apparent. The results of this linear fit can be seen in figure 6.29. Here we arbitrarily determine the bounds of 0 and 26 between which a linear fit is calculated. 26 was chosen due to its distance from the designated contact position of the resonator and substrate. We can subtract this linear fit to produce a clearer plot of the effect that the substrate has had on the frequency of the mode. This can be seen in sub-plot 3 where a red-shift can be noted. The error for the frequency shift is calculated from the standard deviation of the linear fit line where $\sigma = 1.21$.

The pseudo-colour plot (figure 6.30 shoes a second mode forming at step 35 This suggests the substrate has already made contact with the resonator by this point.

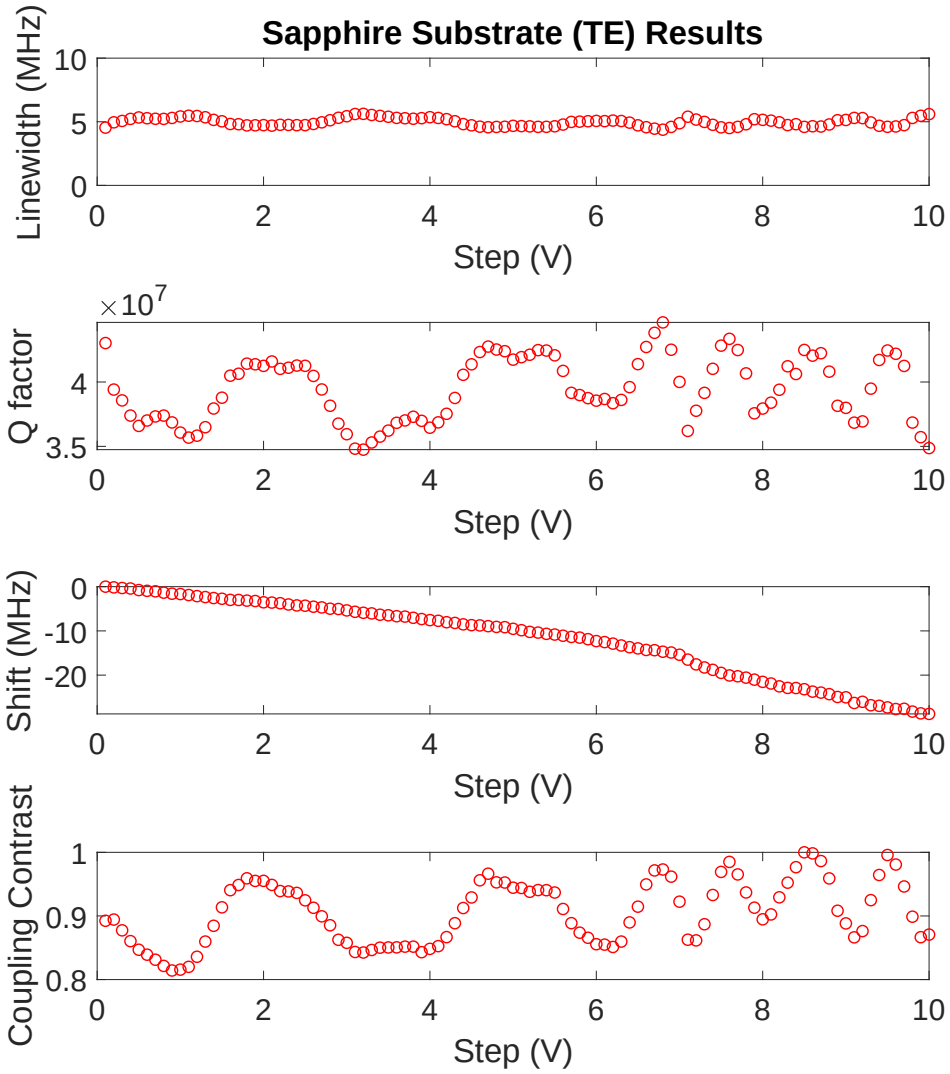

FIGURE 6.25: Raw output of the MATLAB script for the sapphire substrate.

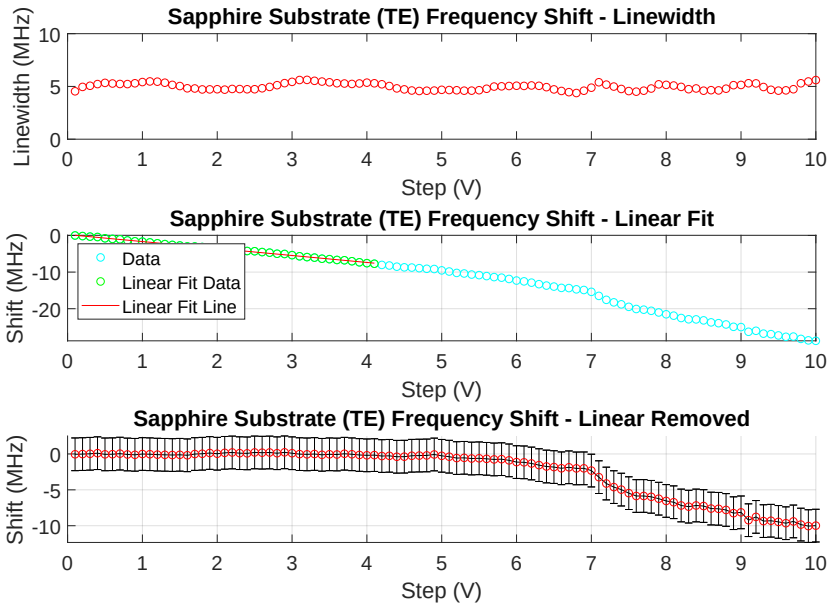

FIGURE 6.26: Analysed output of the MATLAB script for the sapphire substrate. The second subfigure features a linear fit line set at a step number before the substrate enters the evanescent field of the resonator. The third figures shows a more accurate frequency shift when the linear fit is removed from the shift data.

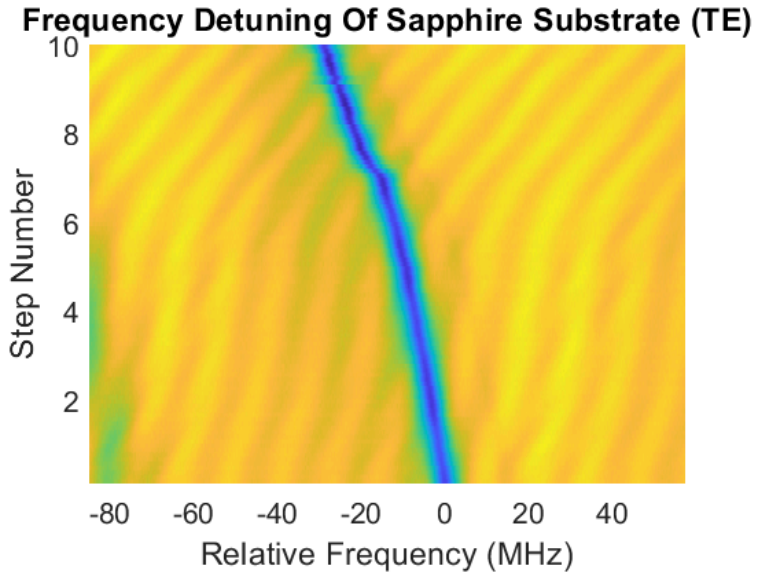

FIGURE 6.27: A pseudo-colour plot of the tested mode. The colour represents the intensity of the light at the detector. The dark line indicates the relative frequency of the mode and shows how it changed over the duration of the sweep.

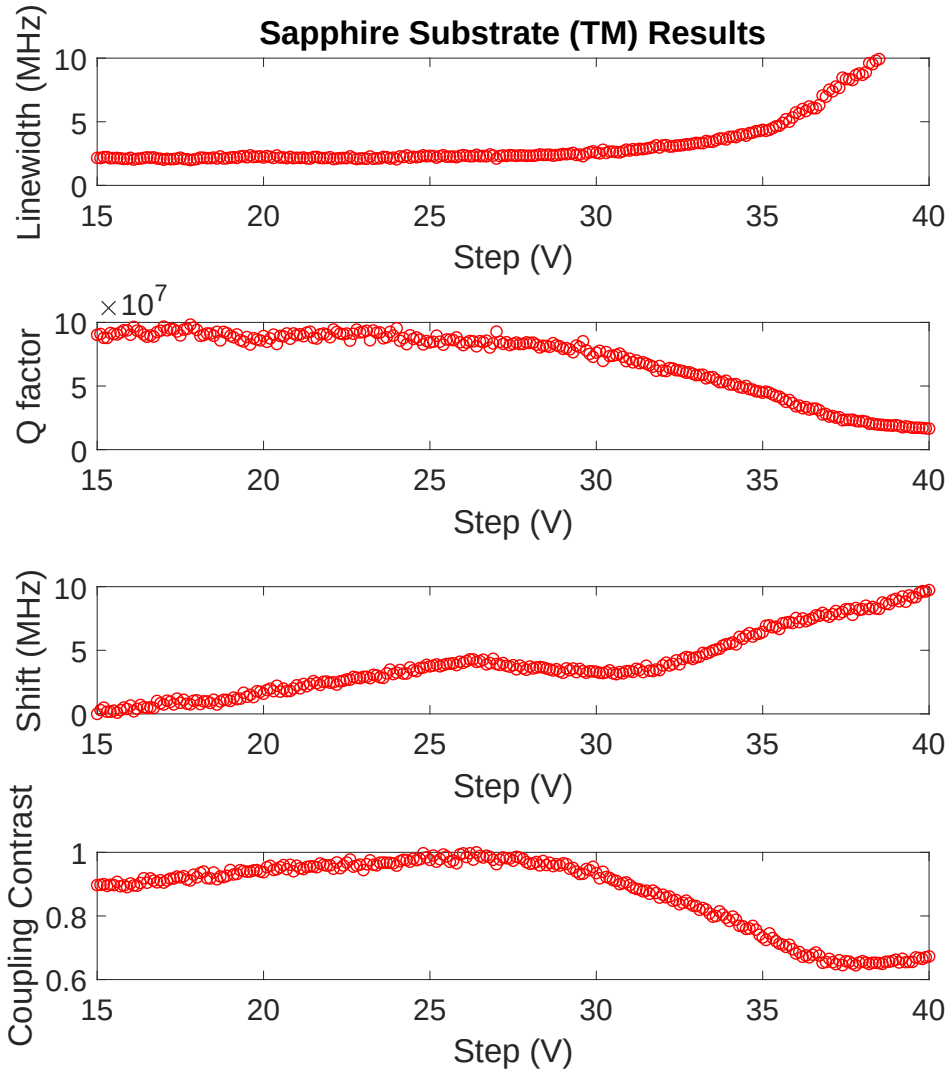

FIGURE 6.28: Raw output of the MATLAB script for the sapphire substrate.

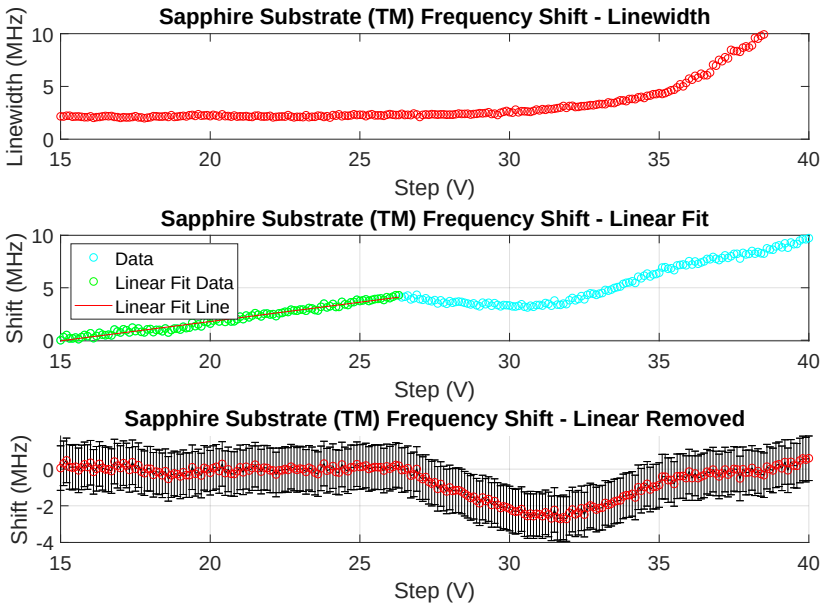

FIGURE 6.29: Analysed output of the MATLAB script for the sapphire substrate. The second subfigure features a linear fit line set at a step number before the substrate enters the evanescent field of the resonator. The third figures shows a more accurate frequency shift when the linear fit is removed from the shift data.

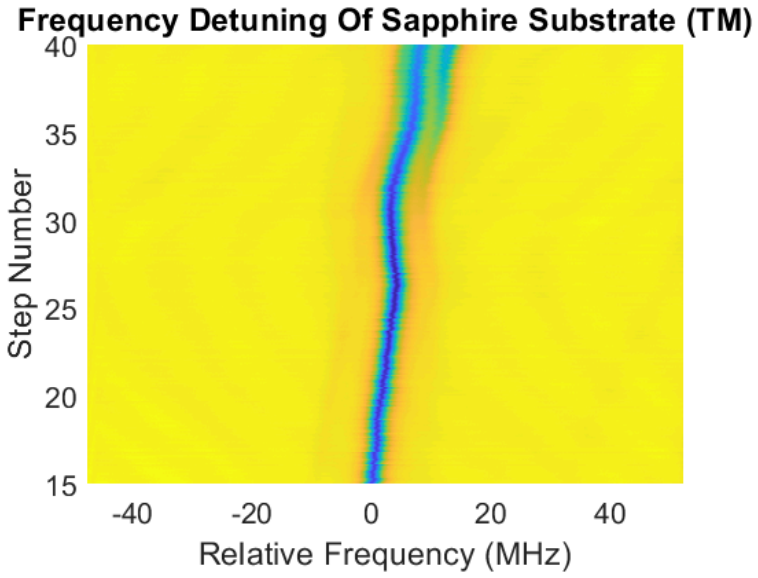

FIGURE 6.30: A pseudo-colour plot of the tested mode. The colour represents the intensity of the light at the detector. The dark line indicates the relative frequency of the mode and shows how it changed over the duration of the sweep.

6.6 Optical Glass

6.6.1 TE Mode Sweep

The results of the sweep using the optical glass substrate are plotted. Figure 6.31 shows that no values remained constant throughout the sweep. Oscillations can be seen in the linewidth, Q-factor and coupling contrast up to step 35. Beyond step 40 it is hard to distinguish the true value of the linewidth or the Q-factor for the optical glass substrate sweep. The linewidth appears to fluctuate about 5.8 MHz up to step 35 and Q-factor appears to fluctuate about 3.3e7 up to step 35. The shape of the frequency shift sub-plot bears a similar shape to that seen in the previous substrate results however there appears to be more instability. It would seem that the appearance of the change in linewidth, Q-factor and coupling contrast occurring near the same step suggests that we can note that the step 39.6 as the point that we can consider the substrate and resonator to be in contact.

The ambient shift in the frequency shift of the mode remains in the optical glass substrate sweep results. We repeat the application of fitting a linear line to the first part of this figure to make the effect of the substrate more apparent. The results of this linear fit can be seen in figure 6.32. Here we arbitrarily determine the bounds of 0 and 17 between which a linear fit is calculated. 17 was chosen due to its distance from the designated contact position of the resonator and substrate. We can subtract this linear fit to produce a clearer plot of the effect that the substrate has had on the frequency of the mode. This can be seen in sub-plot 3. There isn't an obvious red or blue shift to the frequency and the error of the frequency at that position suggests that either direction of shift is likely. The error for the frequency shift is calculated from the standard deviation of the linear fit line where $\sigma = 1.61$.

The pseudo-colour plot (figure 6.33 highlights the discontinuities in the position of the mode after step 38. There are otherwise no obvious places where the mode changes colour or shape.

6.6.2 TM Mode Sweep

The results of the sweep using the optical glass substrate are plotted. Figure 6.34 shows that no values remained constant throughout the sweep. It would seem that the appearance of the change in linewidth near the same step suggests that we can note that the step 40 as the point that we can consider the substrate and resonator to be in contact. This is further confirmed by the presence of mode broadening on the pseudo-colour plot.

The ambient shift in the frequency shift of the mode remains in the optical glass substrate sweep results. We repeat the application of fitting a linear line to the first part of this figure to make the effect of the substrate more apparent. The results of this linear fit can be seen in figure 6.35. Here we arbitrarily determine the bounds of 0 and 32 between which a linear fit is calculated. 32 was chosen due to its distance from the designated contact position of the resonator and substrate. We can subtract this linear fit to produce a clearer plot of the effect that the substrate has had on the frequency of the mode. This can be seen in sub-plot 3. There isn't an obvious red or blue shift to the frequency and the error of the frequency at that position suggests that either direction of shift is likely. The error for the frequency shift is calculated from the standard deviation of the linear fit line where $\sigma = 3.1$.

The pseudo-colour plot (figure 6.36 highlights the discontinuities in the position of the mode after step 38. There are otherwise no obvious places where the mode changes colour or shape.

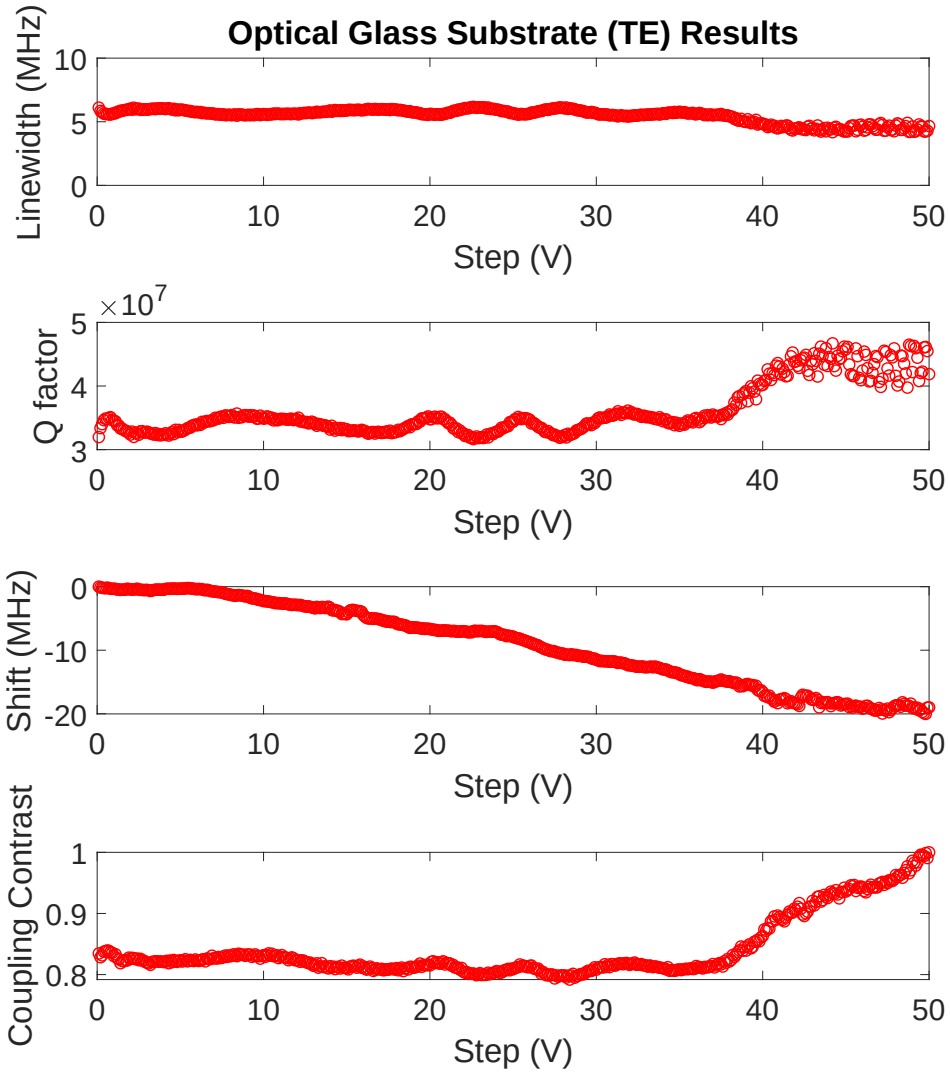

FIGURE 6.31: Raw output of the MATLAB script for the optical glass substrate.

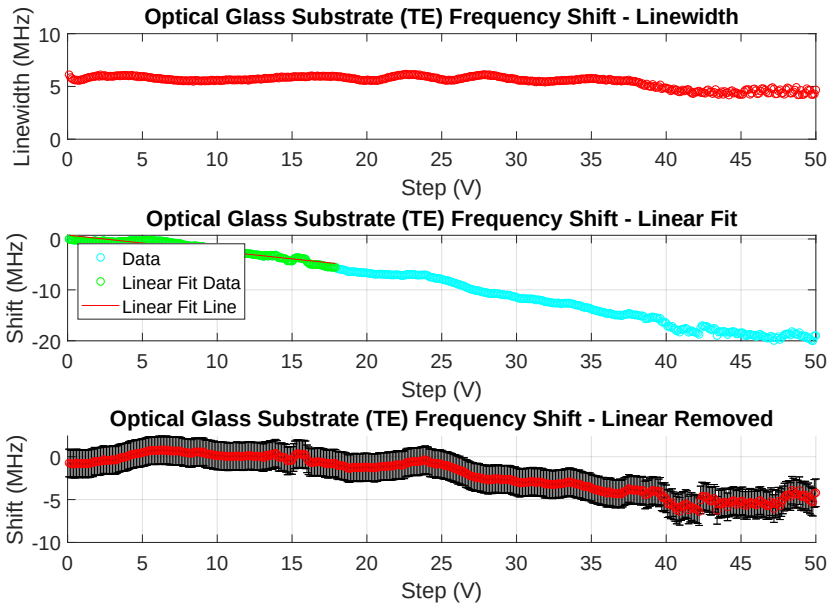

FIGURE 6.32: Analysed output of the MATLAB script for the optical glass substrate. The second subfigure features a linear fit line set at a step number before the substrate enters the evanescent field of the resonator. The third figures shows a more accurate frequency shift when the linear fit is removed from the shift data.

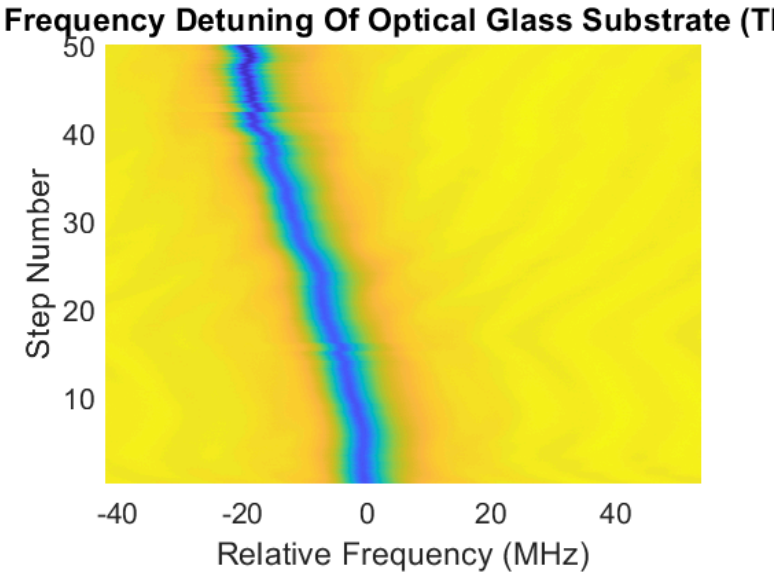

FIGURE 6.33: A pseudo-colour plot of the tested mode. The colour represents the intensity of the light at the detector. The dark line indicates the relative frequency of the mode and shows how it changed over the duration of the sweep.

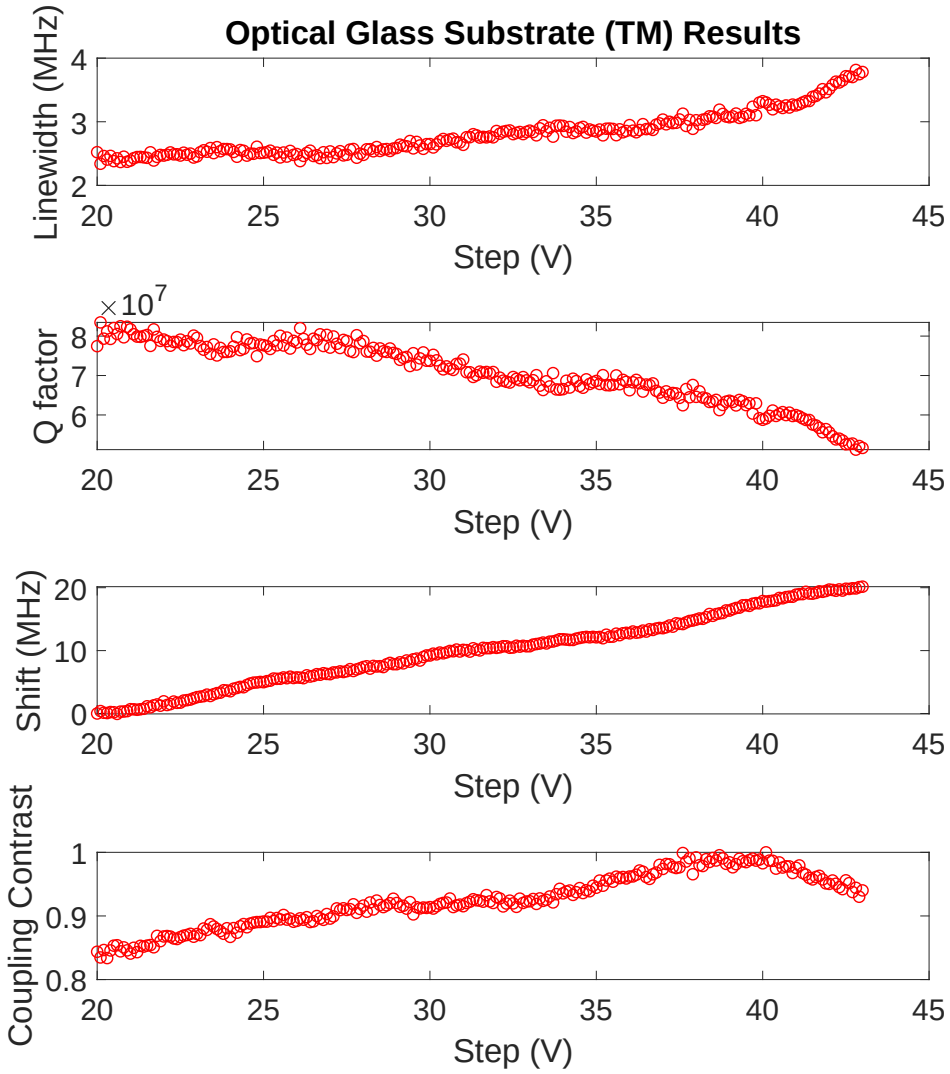

FIGURE 6.34: Raw output of the MATLAB script for the optical glass substrate.

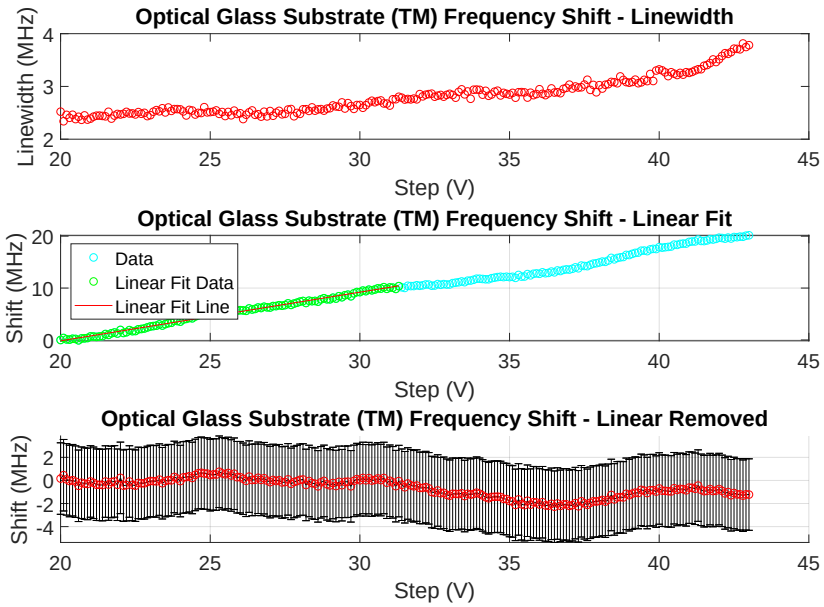

FIGURE 6.35: Analysed output of the MATLAB script for the optical glass substrate. The second subfigure features a linear fit line set at a step number before the substrate enters the evanescent field of the resonator. The third figures shows a more accurate frequency shift when the linear fit is removed from the shift data.

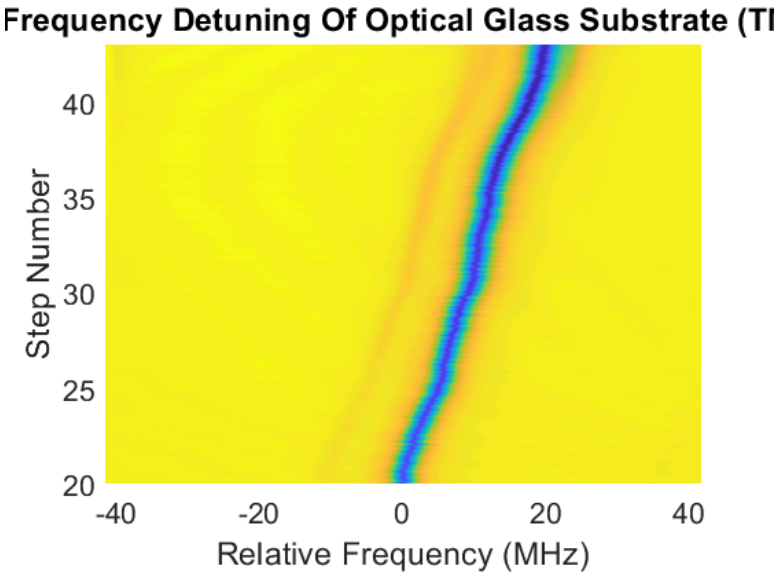

FIGURE 6.36: A pseudo-colour plot of the tested mode. The colour represents the intensity of the light at the detector. The dark line indicates the relative frequency of the mode and shows how it changed over the duration of the sweep.

6.7 Calcium Fluoride

6.7.1 TE Mode Sweep

The results of the sweep using the calcium fluoride substrate are plotted. Figure 6.37 shows that no values remained constant throughout the sweep. Oscillations can be seen in the linewidth, Q-factor and coupling contrast for the entirety of the substrate sweep. The linewidth appears to fluctuate about 3.3 MHz and Q-factor appears to fluctuate about $6.2e7$. The shape of the frequency shift sub-plot bears a similar shape to that seen in the previous substrate results. There is a slight kink in the frequency shift curve at step 50. Also at step 50 the shape of the linewidth and Q-factor curves change slightly with more discontinuities occurring. As the position of the discontinuities in linewidth and Q-factor coincide with the change in gradient of the frequency shift curve, we can note step 49.5 as the point that we can consider the substrate and resonator to be in contact.

The ambient shift in the frequency shift of the mode remains in the calcium fluoride substrate sweep results. We repeat the application of fitting a linear line to the first part of this figure to make the effect of the substrate more apparent. The results of this linear fit can be seen in figure 6.38. Here we arbitrarily determine the bounds of 30 and 42 between which a linear fit is calculated. 42 was chosen due to its distance from the designated contact position of the resonator and substrate. We can subtract this linear fit to produce a clearer plot of the effect that the substrate has had on the frequency of the mode. This can be seen in sub-plot 3 where a slight red shift can be noticed. The error for the frequency shift is calculated from the standard deviation of the linear fit line where $\sigma = 4.41$.

The pseudo-colour plot (figure 6.39 highlights the change in gradient of the frequency shift curve. There are otherwise no obvious places where the mode changes colour or shape.

6.7.2 TM Mode Sweep

The results of the sweep using the calcium fluoride substrate are plotted. Figure 6.40 shows that linewidth remained constant throughout the sweep. There is a kink in the frequency shift curve at step 16. we can note step 16.5 as the point that we can consider the substrate and resonator to be in contact, as this is the step where both the dielectric shift and the coupling contrast are altered.

The ambient shift in the frequency shift of the mode remains in the calcium fluoride substrate sweep results. We repeat the application of fitting a linear line to the first part of this figure to make the effect of the substrate more apparent. The results of this linear fit can be seen in figure 6.41. Here we arbitrarily determine the bounds of 0 and 10 between which a linear fit is calculated. 46 was chosen due to its distance from the designated contact position of the resonator and substrate. We can subtract this linear fit to produce a clearer plot of the effect that the substrate has had on the frequency of the mode. This can be seen in sub-plot 3 where a slight red shift can be noticed. The error for the frequency shift is calculated from the standard deviation of the linear fit line where $\sigma = 0.63$.

The pseudo-colour plot (figure 6.42 highlights the change in gradient of the frequency shift curve. There are otherwise no obvious places where the mode changes colour or shape.

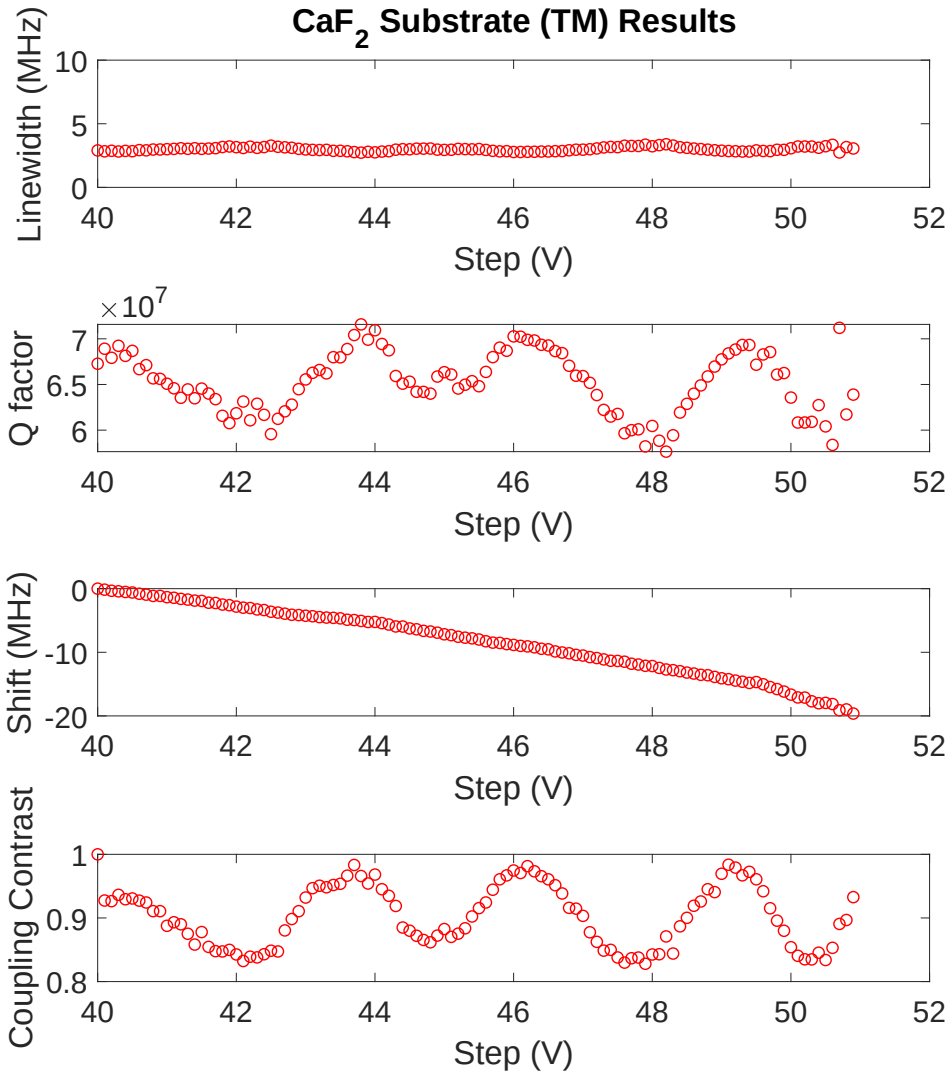

FIGURE 6.37: Raw output of the MATLAB script for the calcium fluoride substrate.

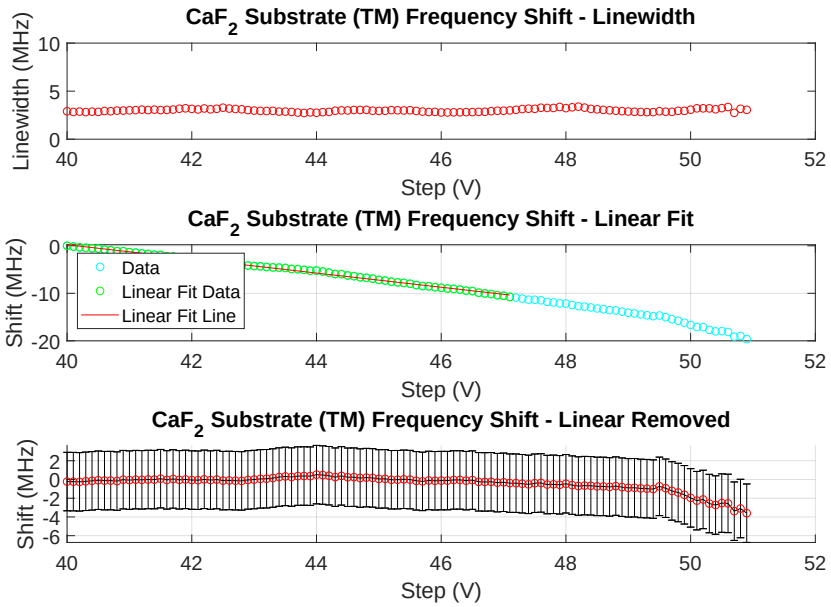

FIGURE 6.38: Analysed output of the MATLAB script for the calcium fluoride substrate. The second subfigure features a linear fit line set at a step number before the substrate enters the evanescent field of the resonator. The third figures shows a more accurate frequency shift when the linear fit is removed from the shift data.

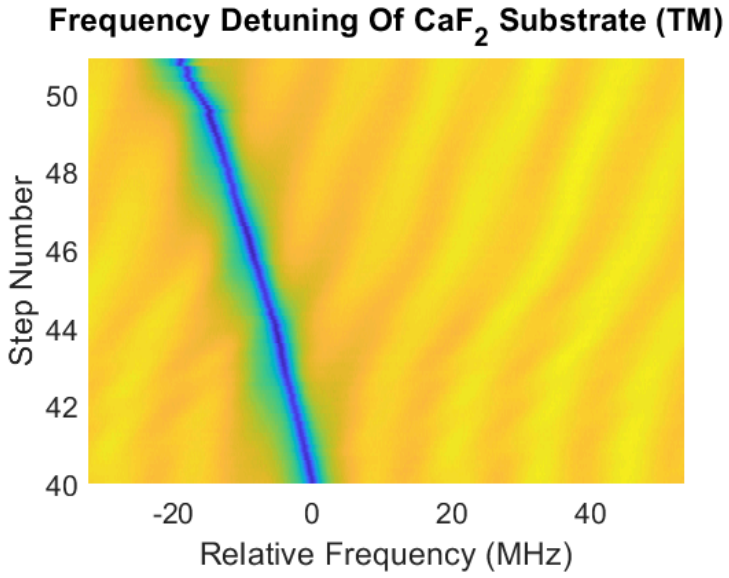

FIGURE 6.39: A pseudo-colour plot of the tested mode. The colour represents the intensity of the light at the detector. The dark line indicates the relative frequency of the mode and shows how it changed over the duration of the sweep.

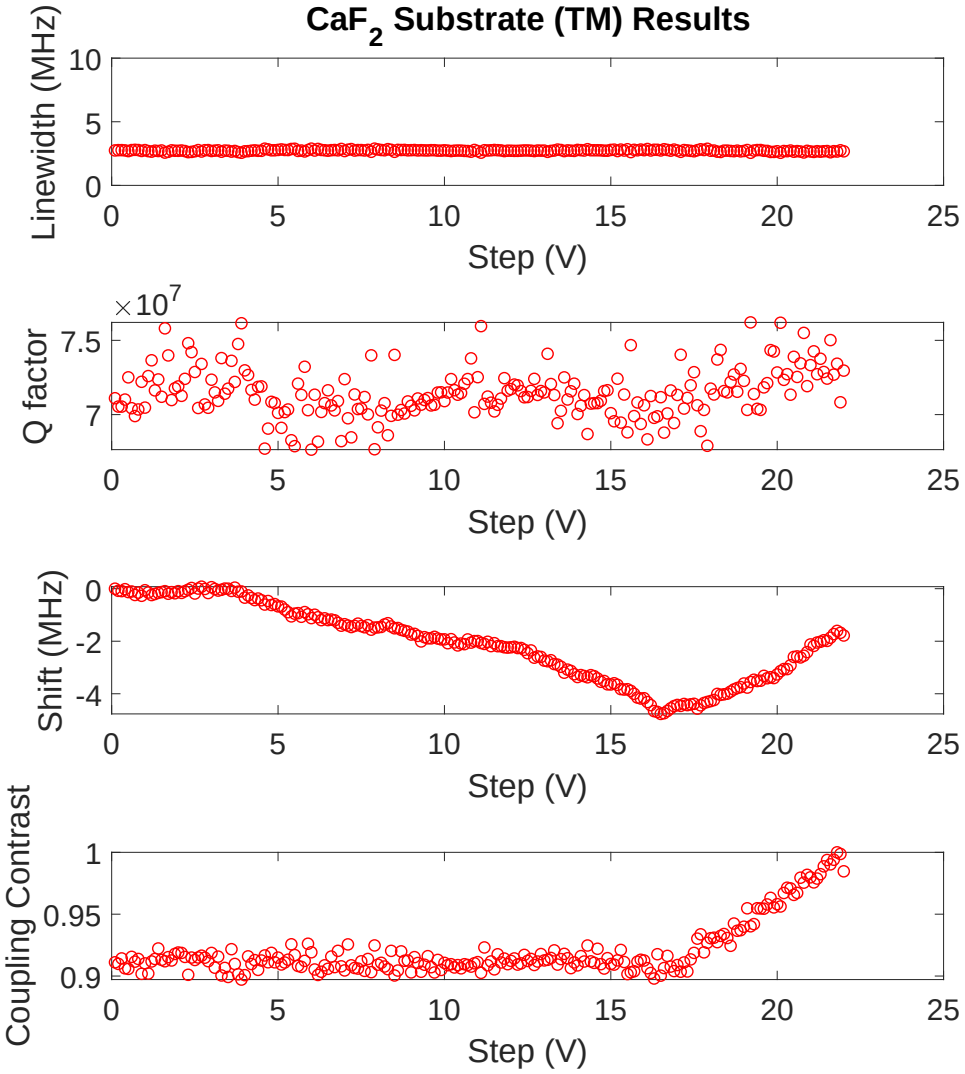

FIGURE 6.40: Raw output of the MATLAB script for the calcium fluoride substrate.

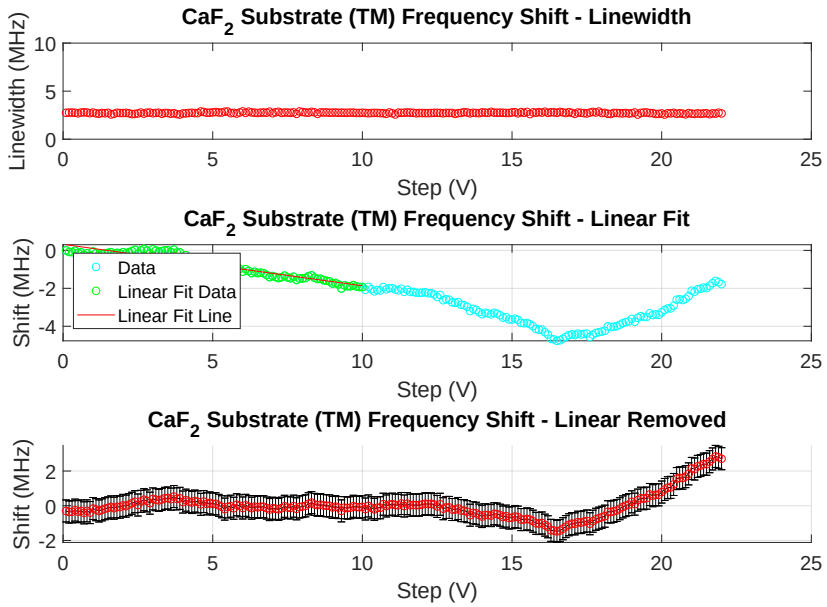

FIGURE 6.41: Analysed output of the MATLAB script for the calcium fluoride substrate. The second subfigure features a linear fit line set at a step number before the substrate enters the evanescent field of the resonator. The third figures shows a more accurate frequency shift when the linear fit is removed from the shift data.

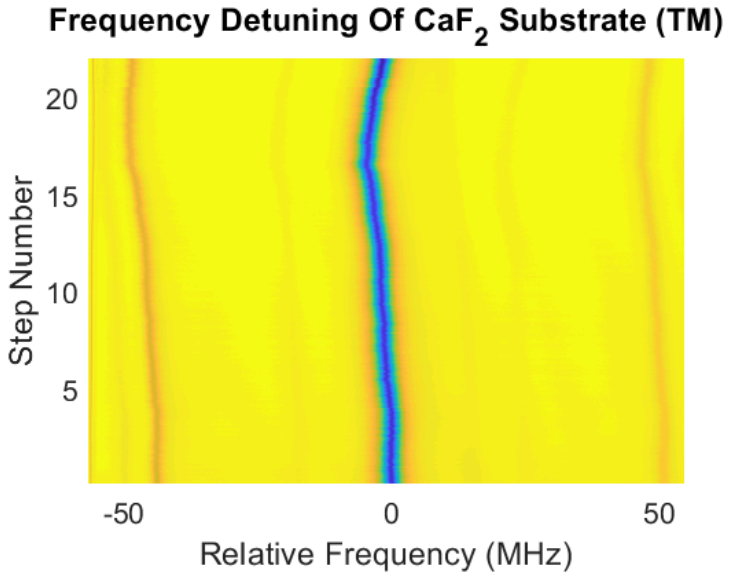

FIGURE 6.42: A pseudo-colour plot of the tested mode. The colour represents the intensity of the light at the detector. The dark line indicates the relative frequency of the mode and shows how it changed over the duration of the sweep.

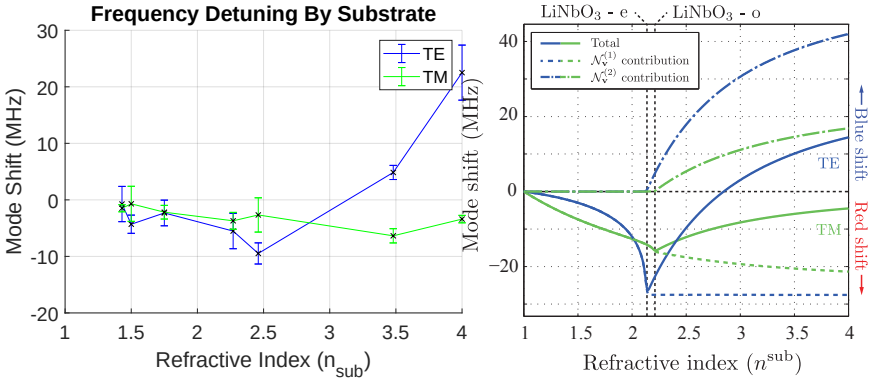

(A) Here we take the results of the frequency shift of the mode from each substrate at their respective contact points to show the effect that the change in refractive index has on the frequency of a mode.

(B) Foreman figure 3a is reinserted here for reference.

FIGURE 6.43: In this figure we see the results of the refractive index of the substrate on mode broadening. Sub figure 6.43a contains the experimental results generated from this research. Sub figure 6.43b contains the theory taken from Foreman et al. (2016) [5]. These are placed side-by-side such that a comparison between theory and experiment can be made.

6.8 Substrate Refractive Index Effects on WGMR Modes

As we aim to investigate the relationship proposed in Foreman et al., we need to measure the frequency detuning and mode broadening figures. To do this we note the position where the substrate can be considered in contact with the resonator. This point provides a comparable measure across the substrates. The refractive indices for the substrates are recalled from table 4.1.

We evaluate the frequency shift of each of the substrates on their respective modes and plot this relationship. This can be seen in figure 6.43. We also retain the error bars from each of the individual sweeps as the error will be equivalent from when it was calculated for each mode, seen in figure 6.43a. When compared with figure 6.43b, we can see that a similar shape emerges in our recreation of the figure. The main point of difference is that the zinc selenide substrate is not expected to have the largest red-shift of the substrates tested. Furthermore, the zinc sulfide substrate was expected to have red-shifted the mode by a greater amount than it did. Finally the amount of error on the germanium (TE) and calcium fluoride (TE) substrates is large when compared with the other substrates tested.

There is similar agreement among the shape of the TM frequency tuning plot. It has a similar shape yet the inflection point is expected to be at the refractive index of zinc selenide and not at silicon as is shown in the figure.

We also evaluate the mode broadening noted in figure 4.2 from Foreman et al. We measure this relationship by determining the linewidth of the mode at the point of contact between the substrate and resonator and subtract from it the linewidth of the mode at a distance considered far away from the resonator, the linear fit line boundary. This is simple to do for the substrates of higher refractive index than lithium niobate as they provide an out-coupling channel that introduces losses into the system and causes the mode to broaden. It is much more difficult to accurately

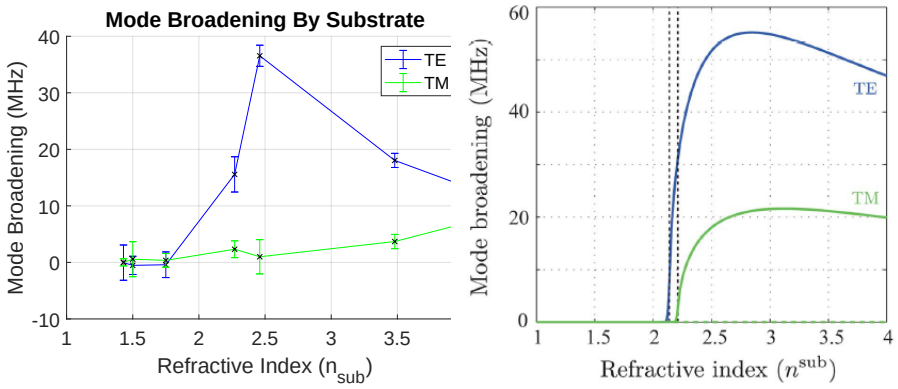

(A) Here we take the results of the broadening of the mode from each substrate at their respective contact points to show the effect that the change in refractive index has on the broadening of a mode.

(B) Foreman figure 3b is reinserted here for reference.

FIGURE 6.44: In this figure we see the results of the refractive index of the substrate on mode broadening. Sub figure 6.44a contains the experimental results generated from this research. Sub figure 6.44b contains the theory taken from Foreman et al. (2016) [5]. These are placed side-by-side such that a comparison between theory and experiment can be made.

measure the mode-broadening of the substrates that have refractive indexes below that of lithium niobate, because there is no obvious point at which the substrate has entered the evanescent field.

Once the mode-broadening has been determined, this is plotted against the refractive index of the respective substrate. The results of this can be seen in figure 6.44. In figure 6.44a, the results of this experiment can be seen. These values are built from the results of each substrate as seen earlier in this chapter. We can compare this to figure 6.44b, we can see that the shape is very similar for TE. The first difference is in the magnitude of the mode-broadening expected. From the theory we would expect zinc selenide to have a larger amount of mode broadening compared to the results. There is good agreement between the substrates with refractive index below lithium niobate (calcium fluoride, optical glass and sapphire) and the theory, as none of these substrates underwent any significant mode broadening and they all have values close to zero. The reason for them not having zero mode broadening is likely due to the way the mode broadening was measured. The magnitudes of the mode-broadening experienced by germanium and silicon was also expected to be greater than the results.

The mode-broadening of the TM modes only show a slight resemblance in the shape between the theory and experiment. The magnitudes of the broadening are off by an order of magnitude and it appears that we get mode broadening for the zinc sulfide substrate and the optical glass substrate, both of which have refractive indices that should be too low for this to occur.

Chapter 7

Discussion

The purpose of this chapter is to discuss in greater depth the results and analysis seen in Chapter 6. We will discuss the results in more detail before looking at the conclusions that can be drawn from this experiment. We will end this chapter with an outlook on the future of this research going forward.

7.1 Analysis

The results resemble the shapes of the figures from the theory but there appears to be disagreement between the magnitudes of the expected shifts and mode broadenings and the results collected in this thesis. One of the first possible sources is noticing that there appeared to be random fluctuations in the linewidth and the Q-factor for the substrates that had a refractive index lower than lithium niobate. Conversely, the linewidths and Q-factors for the substrates that had higher refractive indices than lithium niobate appeared to be very stable. The follow-up issue to these fluctuations is that it makes determining where the resonator and substrate are in contact much harder. It is easy to discern where the resonator and substrate are in contact when the substrate has a refractive index larger than the resonator, as the process of mode-broadening out couples light and gives an indication that the substrate is at least in close proximity to the evanescent field of the resonator, if not directly within it.

There are very few factors that could influence this, the windows are all approximately the same dimensions so it is unlikely to be caused by the relative sizes of the substrates. Furthermore it is not a consequence of the frequency scale as we can remove the mode-broadening of germanium and still see a more uniform distribution of points that the fluctuating substrates cannot replicate.

The temperature control of the setup is also unlikely to be a factor as the substrate sweeps were conducted with the thermistor reading similar temperatures each time. Temperature control will be discussed in more detail in section 7.3 below.

It is also unlikely to be related to the experimental methodology as the same processes were followed for each substrate. The range of movement of the substrate was not kept constant however the range of movement for the optical glass substrate was similar to the range of movement of the silicon substrate so it is unlikely related to the size or distances moved by the substrates during testing.

Finally, the fluctuations are unlikely to be the result of the choice of mode we studied when collecting data. It was very difficult to stabilise the setup for long enough to observe the same mode over the course of collecting data on all seven substrates. As a result we often had to use different modes. While we understand that the theory was based on the idea of retaining the same mode, this was simply not practical in the scope of this experiment. Using different modes between the substrates with higher refractive indices appears to have had little impact on the stability of the linewidth and Q-factor of the observed mode. We do expect that

changing the observed mode would change the results expected. If we observed the same mode, this mode would likely have had a similar Q-factor and linewidth for the duration of the data collection. As the mode would be constant it would also have constant mode numbers. This has implications for comparing the frequency shift between substrates as light coupling into a mode with different mode numbers will experience a slightly different index of refraction inside the resonator. This in turn can change the size of the evanescent field and therefore changing how the substrate interacts with the mode. We do not have reason to believe that this would alter our results by a great deal as we saw that there was a similar change in frequency across many modes tested with the same substrate. This observation removed the requirement to check if a mode was fundamental before the data collection was performed, significantly reducing the preliminary work that needed to be done before every data collection instance.

7.2 Determining Criteria For Results

We collected a large quantity of data during this experiment but only a small number of sweeps could be considered useful or good data. Here we will discuss why most sweeps were rejected from the results seen in chapter 6. Often it was the case that there would be too great an instability in the system. For the majority of this thesis that was likely due to limited thermal stability. We introduced the temperature stabiliser and temperature controller very late into this research and even only having a thermistor in the setup has been very useful in determining why there has been such large instabilities.

The instabilities gave reason to discount results for numerous reasons. At times it would be difficult to obtain results for more than 15 V step ranges as the mode we were observing would simply drift off of the side of the oscilloscope. This cannot be fixed mid sweep in data collection without seriously jeopardising the results. This was a problem faced a lot over this experiment. We had numerous theories about what the cause might be but the inconsistency of the drift made it hard to test it.

Sometimes the instabilities would be of such large magnitudes that it would cover up any trace of a shift. This was a problem for the substrates that displayed little frequency detuning as the magnitude of the instability would be too great to discern the interaction on the frequency from the substrate. This was also a problem for the high refractive index substrates. There were no signs of blue-shift from germanium or silicon for the majority of this experiment. We have reason to believe that the primarily red-shift from the environment is thermal based, but more specifically from heat caused by people moving about the lab. Anecdotally it was noticed that a single person in the lab collecting data could increase the temperature of the resonator environment by as much as 4°. This change in temperature had two effects on the resonances. The first effect we described earlier with reference to modes red-shifting out of the oscilloscope sampling range. The second effect is that it made mode retention extremely difficult between substrates. If we had a mode that showed some stability and a high Q-factor, the process of removing the box and swapping to the next substrate introduced enough heat into the system that modes would sometimes just disappear, or become so hard to discern from the background noise that new modes were sought out instead. This was confirmed when calibrating the temperature controller and purposefully introducing large amounts of heat into the resonators environment, a substantial increase in temperature could cause even

a stable mode to 'disappear'. Some of these thermal instabilities manifested as fluctuations that were noticed as periodic movements in the results. These fluctuations often increased the calculated error associated with the frequency shift. Steps were taken to try and reduce the magnitude of these errors, such as refining the analysed area to be more local to the evanescent field of the WGMR, however we felt that the process we had for fitting errors was sufficiently rigorous that we were obliged to keep this method the same throughout the sweeps. This did lead to error bars with greater magnitudes than perhaps is desired, however it would also prove difficult to justify manipulating single substrate data or errors for the purpose of making the bars smaller.

Sometimes even if the mode was stable, there would be little sign of an interaction with the substrate. This results in plots that show no change beyond random noise for linewidth, Q-factor or coupling contrast. The solution to this is to adjust the distance between the resonator and substrate but there were times when adjusting the offset of the substrate position by as much as 2 µm would not yield anything different. We tried working around this by using different techniques such as sweeping the substrate backwards immediately after hearing that it had made contact with the resonator when moved into place. This did not prove useful as some indications suggested that we had deformed the resonator by such an amount that the substrate looked to have remained in the evanescent field for the entirety of the sweep. This is not useful data as the results of constantly deforming a resonator make determining the point of contact between the substrate and resonator very difficult.

There was also an issue of mode deterioration, whereby a mode that might appear stable would sweep with a steadily worsening coupling contrast until it was indistinguishable from the baseline noise. Adjusting the setup to change the coupling into the resonator often became insufficient to recover the mode, meaning that mode deterioration often required that the resonator be removed from the setup and cleaned (using the process detailed in section 2.6) and re-coupled into. The cause was theorised to be a possible combination of the repeated impacts between the resonator and substrate causing an introduction of dust or other particles onto the resonator (increasing losses) and the impacts moving the resonator slightly in relation to the substrate and coupling prism causing the coupling setup to change slightly.

As can be seen throughout chapter 6, we used a linear fit line to try and reverse some of the effects of the passive drift occurring before the substrate enters the evanescent field. There were many times when this drift was not linear and therefore would be hard to justify removing with a linear fit line. Once the temperature controller was installed, it was not able to reach thermal equilibrium due to various factors explained in 7.3. Because it was not able to reach thermal equilibrium it would exist in a near constant state of heating and cooling. If we collected data during an inflection point between heating and cooling, a non linear shift would be noted throughout the results of that sweep. This is because the introduction of heat would red-shift the mode, and removal of heat would blue-shift the mode. We were experiencing both directions of shift in some sweeps that could not be justified as data.

Finally there were instabilities that made it hard to separate the results into the controlled component and the interaction component. If a substrate is sufficiently far away from the evanescent field, we expect that the mode has a near constant linewidth and coupling contrast. This was not always the case as there were many sweeps conducted that showed a wildly fluctuating linewidth or coupling contrast that made us think there were grounds to discount the sweep. This was not done

to cherry-pick clean data sets but used more as a first measure of data quality. Fluctuations in linewidths could still be used in data sets depending on the magnitude and frequency of the fluctuations. This was another problem of collecting the results with some substrates that did not experience a large dielectric shift because it clouds the difference between a sweep that works and shows no shift and a sweep that doesn't show a shift because it's too far away. We had to use pseudo colour plots along with the raw result outputs to make a decision regarding whether or not a substrate had interacted with the resonator.

Let us change tact for a moment and discuss how we selected the good data rather than discounted the bad. Most data sweeps were taken and analysed to produce the raw result plots seen in 6, what we looked for was mostly a difference between the start and end of a sweep. This was a good rule of thumb to suggest an interaction had taken place. The data was looked upon more favourably if there was a smooth transition between the start and end of a sweep. Discontinuities were not grounds for discounting the data set unless the discontinuities were too dispersed from a line of best fit.

Data was mostly evaluated in this way, smooth, stable data was more likely to be analysed because it would throw less exceptions when analysed in MATLAB. At no point did we choose the data sets based on the observed dielectric shift alone, there were many sweeps that demonstrated shifts that would likely fall in line with the theory, but were discounted for any of the other reasons given above.

7.2.1 Frequency Shift Measurement

From the discussion of the method in section 5.2, one might wonder how a single mode was kept in focus despite all of the problems discussed above, for the duration of collecting data across 6 different substrates. Unfortunately there was no single mode that gave usable data across all 6 substrates as there was almost always a reason to discount data collected from one or more modes from the discussion above. This lead to an important question that rose from the method. When one mode is presenting data that does not need to be discounted, should repeatability or extend-ability be the priority? The argument for repeatability is that we have a mode that can be swept over multiple times for one substrate and good data for one substrate be collected, but risk the mode deteriorating before data can be collected for all 6 substrates. Conversely, if the data is "good enough" for one mode, it could be used to collect data across the remaining substrates but risk the lower sample size skewing the results for a given substrate. Our answer to this question was to exercise judgment in each case depending on the factors at play. Often this would mean taking data from 6 sweeps (3 in each direction). Usually there would be a reason to discount at least one if not several of the sweeps for reasons discussed above. If data was collected for a sweep in each direction, and the results of these sweeps were within the bounds of error of each other, we usually tried to preserve this mode for testing on other substrates, thus striking a balance between repeatability and extend-ability. Building a running average for each sweep across different modes would have been preferable but was not possible within the scale of this experiment. This was due to the short interval between data collection and the writing of this thesis. Instead a single sweep was selected to be representative of the sweeps collected by testing that sweep against the criteria discussed above.

7.3 Temperature Control

We discovered that temperature played a very important role in the stability of the setup. We used the cardboard box and temperature controller to help control the temperature during the data collection. The temperature in the laboratory and the local resonator environment could have a large impact on the frequency of the mode observed if it was not controlled carefully. Often by simply existing in the lab while taking data would be enough to heat the environment around the resonator and cause a red-shift to occur in the data. This is why most of the substrate results feature a red-shift in the frequency shift that we attempted to minimise by using a linear fit. To demonstrate the effect that temperature can have on the frequency, we found some relevant literature on the thermo-optic properties of lithium niobate. Each of the two papers found are discussed in detail below.

One paper by Savchenkov et al. (2006) [20] features a WGMR left for 4 hours with a sweeping laser. This shifted the frequency by approximately 3 GHz as can be seen in figure 7.1. As this was left over a period of 4.5 h, we can determine that their resonator had a frequency drift of

$$f_{\text{drift}} = \frac{\Delta \cdot f}{\text{time}}, \tag{7.1}$$

$$f_{\text{drift}} = 11.\overline{11}\ \text{MHz min}^{-1}. \tag{7.2}$$

The duration of a sweep in our experiment is approximately 30 s. Savchenkov et al. uses figure 7.1 to show how their spectrum evolves in time. The passive frequency shift experienced by the substrates in our experiment is unlikely to be explained by this effect, due to the difference in direction of drifts experienced. The frequency drift presented in this paper would need to be negative to explain the passive red-shift experienced by the substrates in our experiment. Even if the direction was reversed, the red-shift was often at a magnitude greater than $11.\overline{11}$ MHz min^{-1}.

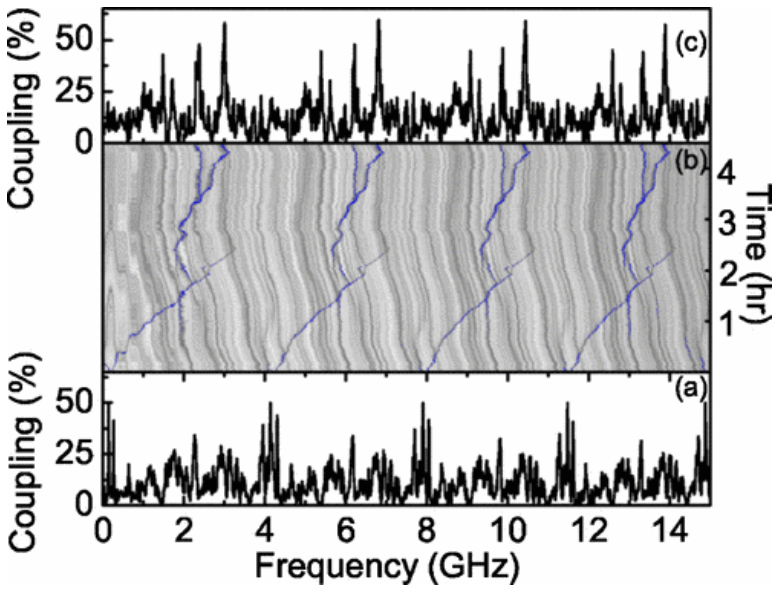

FIGURE 7.1: Figure taken from Savchenkov et al. showing the effect of temperature on the frequency of a WGMR..

The second paper we will discuss is a paper by Moretti et al. (2005) [21] which discusses the thermal expansion of a lithium niobate WGMR. We assumed that the cardboard box would thermalize the resonator and substrate to the same temperature within 120 s of placing the cardboard box over our setup. [21] derives the coefficients for thermal expansion in a z-cut lithium niobate resonator. This is identical to the one used in our setup.

To determine how temperature changes the frequency then, we have the frequency of a WGMR mode

$$\nu = \frac{m \cdot c}{2\pi \cdot R \cdot n_{\text{eff}}}. \tag{7.3}$$

Taking the time derivative yields

$$\frac{d\nu}{dT} = -\frac{\mathrm{m} \cdot \mathrm{c}}{\mathrm{R} \cdot \mathrm{n_{eff}}} \left(\frac{1}{\mathrm{R}} \frac{\partial R}{\partial T} + \frac{1}{\mathrm{n_{eff}}} \frac{\partial \mathrm{n_{eff}}}{\partial T} \right). \tag{7.4}$$

We make the assumption that $n_{eff} \approx n_e$ because the resonator is mounted with the optical axis in the z-direction. This also assumes that only the fundamental modes are coupled into. Because of this assumption, we can therefore also assume that they will have approximately equal temperature derivatives

$$\frac{\partial \mathrm{n_{eff}}}{\partial T} \approx \frac{\partial \mathrm{n_e}}{\partial T}. \tag{7.5}$$

Therefore we have

$$\frac{1}{\nu}\frac{d\nu}{dT} = -\frac{1}{\mathrm{R}}\frac{\partial \mathrm{R}}{\partial \mathrm{T}} - \frac{1}{\mathrm{n_e}}\frac{\partial \mathrm{n_e}}{\partial \mathrm{T}}. \tag{7.6}$$

We define

$$\alpha_{perp} = \frac{1}{\mathrm{R}}\frac{\partial \mathrm{R}}{\partial \mathrm{T}}, \tag{7.7}$$

and

$$\alpha_{ne} = \frac{1}{\mathrm{n_e}}\frac{\partial \mathrm{n_e}}{\partial \mathrm{T}}. \tag{7.8}$$

We can now rewrite equation 7.6 as

$$\frac{1}{\nu}\frac{d\nu}{dT} = -\alpha_{perp} - \alpha_{ne}. \tag{7.9}$$

We have collected terms parallel to the optical axis α_{ne} and the terms perpendicular to the optical axis α_{perp}. In Pignatiello et al. (2007) [22] they measure the thermal expansion coefficients of lithium niobate. We quote the result for z-cut lithium niobate

$$\alpha_{perp} = 13.6 \times 10^{-6} K^{-1}. \tag{7.10}$$

Moretti et al. doesn't solve for the coefficients with 1550nm light but we assume that the results for 1523nm are approximately the same. We also assume room temperature (22°). Starting with equation 4 of [21]

$$\frac{dn_e}{dT} = -2.6 + 19.8 \times 10^{-3} T (10^{-5} K^{-1}), \tag{7.11}$$

and substitute 22°C = 295.15 K we get

$$\frac{dn_e}{dT} = -2.6 \cdot 10^{-5} + 19.8 \cdot 10^{-3} \cdot 295.15 \cdot 10^{-5}. \tag{7.12}$$

$$\frac{dn_e}{dT} = 3.244 \times 10^{-5} \tag{7.13}$$

We can use this result with $n_e = 2.21$ to solve equation 7.8

$$\alpha_{ne} = 1.468 \times 10^{-5}. \tag{7.14}$$

Putting these values together to reform equation 7.6 gives us

$$\frac{1}{\nu}\frac{d\nu}{dT} = -13.6 \times 10^{-6} - 1.468 \times 10^{-5} = -2.828 \times 10^{-5}. \tag{7.15}$$

To get the derivative we multiply both sides by ν which we find by solving the wave equation 4.3 for $\lambda = 1550$

$$\nu_{1550} = 1.935 \times 10^{14}. \tag{7.16}$$

Therefore

$$\frac{d\nu}{dT} = -5.472 \times 10^{9}. \tag{7.17}$$

We rearrange this expression to find that a 10 MHz change in frequency can be caused by a change in temperature of $-1.83°$mK.

In this experiment we used a temperature controller that could thermalize a setup with a stability of $\pm 0.02°$C but there were problems with the implementation. The heat-sink we used did not seem to be effective at dispersing the heat. If the thermistor was at a higher temperature than was set on the temperature controller, the Peltier would dump heat into the heat-sink. This would cause the heat-sink to act like a proxy heater and warm up the resonator even if the brass rod was cooling down. We attempted to use a small current through the Peltier to generate a fixed red-shift that could be accounted for in the results, yet the ability to generate a small red-shift was masked by the passive heating of the resonator environment that occurred when people remained in the lab for any period of time. Further to this point, the lack of thermal insulation between the brass rod, the aluminium block it resides in and the copper temperature control block meant that the aluminium block would also function as a large heat-sink secondary to the one mounted on the Peltier. As this was connected directly to the optical table it makes it hard to gauge and calibrate the temperature controller as the system is made more complicated than passing a thermal load through a copper block. Even when the temperature would be close to stable, and oscillate over a range of 0.1°C, the temperature fluctuations would cause the modes to oscillate back and forth on the oscilloscope. To have the modes moving forwards and backwards is less desirable than movement in a single direction. In a single direction we can be aware of the shift when we are taking data, knowing that the shift we are seeing while collecting the data. If the modes were to oscillate while data was being collected, it would be much harder to discern whether or not the shift we were seeing was resulting from the substrate of the temperature.

As we were not able to use the temperature controller to its full extent, the way we used it was more to supplement the passive temperature changes that were occurring in the local environment to the resonator. We used the temperature controller to raise the temperature of the resonator environment if the red-shift resulting

from passive heating looked to increase the frequency of the observed mode past the bounds of the oscilloscope screen.

7.4 Conclusion

Our aim was to determine if the relationship between refractive index and frequency shift exists as is proposed in Foreman et al. We have shown that the relationship is verifiable from the results produced in chapter 6, and through creating our own versions of the figures in presented in Foreman et al. that were discussed in section 6.8.

We were also able to show that the relationship between mode broadening and substrate refractive index can also be verified. These conclusions are strongest for the TE modes tested, however the TM modes tested appear to bear a similar shape when compared with the theory from Foreman et al.

While these results are conclusive, the conclusions would be further strengthened if a single mode were observed for the duration of the data collection. We showed that the temperature control is crucial for mode retention as thermal fluctuations are responsible for the dismissal of a large amount of the data collected.

7.5 Outlook

There are now systems in place that would make further study of this possible, we have demonstrated the ability to collect large quantities of data using autonomous computer scripts and communication between laboratory apparatus. We were able to demonstrate that temperature fluctuations are the main source of instability in this setup. Further refining of the temperature controller design would reduce thermal fluctuations and potentially make observing one mode across all seven substrates possible. While we have shown evidence of the relationship for frequency tuned TE modes, the relationship for frequency tuning TM modes can be investigated further due to the reduced agreement between the experimental results and the theory.

Bibliography

[1] Brian Dearsley. *Exploring London's St Paul's Cathedral: A Visitor's Guide | PlanetWare*. URL: https://www.planetware.com/london/st-pauls-cathedral-eng-l-spal.htm (visited on 02/11/2019).

[2] John William Strutt Rayleigh. *The theory of sound*. eng. London, Macmillan and co., 1877. URL: http://archive.org/details/theorysound06raylgoog (visited on 05/28/2017).

[3] Gustav Mie. "Beiträge zur Optik trüber Medien, speziell kolloidaler Metallösungen". en. In: *Annalen der Physik* 330.3 (1908), pp. 377–445. ISSN: 1521-3889. DOI: 10.1002/andp.19083300302. URL: https://onlinelibrary.wiley.com/doi/abs/10.1002/andp.19083300302 (visited on 01/23/2019).

[4] P. Debye. "Der Lichtdruck auf Kugeln von beliebigem Material". en. In: *Annalen der Physik* 335.11 (Jan. 1909), pp. 57–136. ISSN: 1521-3889. DOI: 10.1002/andp.19093351103. URL: https://onlinelibrary.wiley.com/doi/abs/10.1002/andp.19093351103 (visited on 01/23/2019).

[5] Matthew R. Foreman et al. "Dielectric tuning and coupling of whispering gallery modes using an anisotropic prism". EN. In: *JOSA B* 33.11 (Nov. 2016), pp. 2177–2195. ISSN: 1520-8540. DOI: 10.1364/JOSAB.33.002177. URL: https://www.osapublishing.org/abstract.cfm?uri=josab-33-11-2177 (visited on 05/24/2017).

[6] Dominik W. Vogt et al. "Anomalous blue-shift of terahertz whispering-gallery modes via dielectric and metallic tuning". In: (Jan. 2019). DOI: arXiv:1901.03424. URL: https://arxiv.org/abs/1901.03424.

[7] Luke S. Trainor et al. "Selective Coupling Enhances Harmonic Generation of Whispering-Gallery Modes". In: *Physical Review Applied* 9.2 (Feb. 2018), p. 024007. DOI: 10.1103/PhysRevApplied.9.024007. URL: https://link.aps.org/doi/10.1103/PhysRevApplied.9.024007 (visited on 02/12/2019).

[8] Florian Sedlmeir et al. "Experimental characterization of an uniaxial angle cut whispering gallery mode resonator". In: *Opt. Express* 21.20 (Oct. 2013), pp. 23942–23949. DOI: 10.1364/OE.21.023942. URL: http://www.opticsexpress.org/abstract.cfm?URI=oe-21-20-23942.

[9] M. L. Gorodetsky and V. S. Ilchenko. "Optical microsphere resonators: optimal coupling to high-Q whispering-gallery modes". EN. In: *JOSA B* 16.1 (Jan. 1999), pp. 147–154. ISSN: 1520-8540. DOI: 10.1364/JOSAB.16.000147. URL: https://www.osapublishing.org/abstract.cfm?uri=josab-16-1-147 (visited on 05/25/2017).

[10] J. C. Knight et al. "Phase-matched excitation of whispering-gallery-mode resonances by a fiber taper". In: *Opt. Lett.* 22.15 (Aug. 1997), pp. 1129–1131. DOI: 10.1364/OL.22.001129. URL: http://ol.osa.org/abstract.cfm?URI=ol-22-15-1129.

[11] I. Breunig et al. "Whispering gallery modes at the rim of an axisymmetric optical resonator: Analytical versus numerical description and comparison with experiment". EN. In: *Optics Express* 21.25 (Dec. 2013), pp. 30683–30692. ISSN: 1094-4087. DOI: 10.1364/OE.21.030683. URL: https://www.osapublishing.org/oe/abstract.cfm?uri=oe-21-25-30683 (visited on 01/23/2019).

[12] Christoph S. Werner et al. "Control of mode anticrossings in whispering gallery microresonators". In: *Opt. Express* 26.2 (Jan. 2018), pp. 762–771. DOI: 10.1364/OE.26.000762. URL: http://www.opticsexpress.org/abstract.cfm?URI=oe-26-2-762.

[13] H. H. Li. "Refractive index of silicon and germanium and its wavelength and temperature derivatives". In: *Journal of Physical and Chemical Reference Data* 9.3 (1980), pp. 561–658. DOI: 10.1063/1.555624. URL: https://doi.org/10.1063/1.555624.

[14] Martin A. Green. "Self-consistent optical parameters of intrinsic silicon at 300K including temperature coefficients". In: *Solar Energy Materials and Solar Cells* 92.11 (Nov. 2008), pp. 1305–1310. ISSN: 0927-0248. DOI: 10.1016/j.solmat.2008.06.009. URL: http://www.sciencedirect.com/science/article/pii/S0927024808002158.

[15] D. T. F. Marple. "Refractive Index of ZnSe, ZnTe, and CdTe". In: *Journal of Applied Physics* 35.3 (Mar. 1964), pp. 539–542. ISSN: 0021-8979. DOI: 10.1063/1.1713411. URL: https://doi.org/10.1063/1.1713411 (visited on 01/25/2019).

[16] Mary Debenham. "Refractive indices of zinc sulfide in the 0.405–13-μm wavelength range". In: *Appl. Opt.* 23.14 (July 1984), pp. 2238–2239. DOI: 10.1364/AO.23.002238. URL: http://ao.osa.org/abstract.cfm?URI=ao-23-14-2238.

[17] Irving H. Malitson. "Refraction and Dispersion of Synthetic Sapphire". In: *J. Opt. Soc. Am.* 52.12 (Dec. 1962), pp. 1377–1379. DOI: 10.1364/JOSA.52.001377. URL: http://www.osapublishing.org/abstract.cfm?URI=josa-52-12-1377.

[18] Irving H. Malitson. "A Redetermination of Some Optical Properties of Calcium Fluoride". In: *Appl. Opt.* 2.11 (Nov. 1963), pp. 1103–1107. DOI: 10.1364/AO.2.001103. URL: http://ao.osa.org/abstract.cfm?URI=ao-2-11-1103.

[19] Jiang Li et al. "Sideband spectroscopy and dispersion measurement in microcavities". In: *Opt. Express* 20.24 (Nov. 2012), pp. 26337–26344. DOI: 10.1364/OE.20.026337. URL: http://www.opticsexpress.org/abstract.cfm?URI=oe-20-24-26337.

[20] Anatoliy A. Savchenkov et al. "Enhancement of photorefraction in whispering gallery mode resonators". In: *Physical Review B* 74.24 (Dec. 2006), p. 245119. DOI: 10.1103/PhysRevB.74.245119. URL: https://link.aps.org/doi/10.1103/PhysRevB.74.245119.

[21] Luigi Moretti et al. "Temperature dependence of the thermo-optic coefficient of lithium niobate, from 300 to 515 K in the visible and infrared regions". In: *Journal of Applied Physics* 98.3 (Aug. 2005), p. 036101. ISSN: 0021-8979. DOI: 10.1063/1.1988987. URL: http://aip.scitation.org/doi/10.1063/1.1988987.

[22] Felice Pignatiello et al. "Measurement of the thermal expansion coefficients of ferroelectric crystals by a moiré interferometer". In: *Optics Communications* 277 (Sept. 2007), p. 14. DOI: 10.1016/j.optcom.2007.04.045.